Modelling Compositional Convection for Applications to Exoplanet Atmospheres



Namrah Habib

Under the Supervision Of:

Prof. Raymond Pierrehumbert

A thesis submitted in partial fulfillment for the degree of Doctor of Philosophy

Christ Church · University of Oxford · December 2023

A Pandu Production.

Declaration

I hereby declare that except where specific reference is made to the work of others, the contents of this dissertation are original and have not been submitted in whole or in part for consideration for any other degree or qualification in this, or any other university. This dissertation is my own work and contains nothing which is the outcome of work done in collaboration with others, except as specified in the text and Acknowledgments. Chapter 3 has been accepted for publication in The Astrophysical Journal as:

> Habib, N. and Pierrehumbert, R.T, "Modeling Non-Condensing Compositional Convection for Applications to Super-Earth and Sub-Neptune Atmospheres". *The Astrophysical Journal*, (2023).

Namrah Habib
February 2024

Acknowledgements

I have received a mountain of support throughout my DPhil, and I am extremely grateful to everyone who has contributed. First, I would like to thank my supervisor, Ray Pierrehumbert, for his unwavering support and guidance throughout my DPhil and for being an exceptional scientific advisor. I have learned so much from being a part of your research group. Thank you for taking a chance on me and believing in my potential. Your enthusiasm and curiosity about both our world and all the planets we study are infectious. I would also like to thank all the postdocs and students in Ray's group for their support, especially Maxence Lefèvre and Xianyu Tan. Thank you both for taking the time to teach me, answer all of my questions, and for all your persistent support throughout my DPhil. I could not have completed this project without you guys.

I would also like to thank Bowen Fan, Francisco Spaulding-Astudillo, and Xuan Ji. I've had invaluable discussions with you guys. Thank you for challenging me, testing my understanding, and stimulating ideas. I was going through a tough time with my PhD project, and being able to attend RossbyPalooza was a phenomenal experience. I am grateful for all the people I had the opportunity to meet and chat with at RossbyPalooza.

Huge thanks to Sally Blumenthal, Ed Derby, Emily Van de Koot, Hamish Innes, Marylou Fournier Tondreau, and Richard Chatterjee. I was fortunate to meet you all during my PhD. Without you, the DPhil would not have been nearly as manageable or as fun. I am grateful for your support and friendship. I'd also like to thank Emily, Hamish, Maxence, Mark and Xianyu for all their help and support during the last term of my DPhil.

I would also like to express my gratitude to Neil Bowles for always sharing your space mission stories with me whenever I would see you in AOPP, for all of your advice, and for your guidance during the pandemic. Thank you, Dani DellaGiustina, and Kiya Riverman, for mentoring and supporting me, and giving me the opportunity to work with the SIIOS team.

Dani, you are an amazing role model and mentor, and I cannot thank you enough for all of your help, guidance, and support. I hope to be as brilliant as you one day. Additionally, I would like to thank Cece, Christian, Kristina, and Georgia. I feel lucky to have met you guys. You guys are absolutely amazing, and I will always be grateful for the time I spent with you in Greenland.

I would like to extend thanks to my community of friends. Nathan, Keara, Angela, Steph, Georgiana, Cathrin, and Ryan – thank you all for believing in me, pushing me when I needed it, calling me out when I needed it, and generally being there for me. My DPhil would not have been the same without you all, and I am grateful and fortunate to have you guys in my life.

I want to thank my family for being by my side - I hope I can make you proud. I'd especially like to thank my siblings, Sana and Mohammad, for making me experience every emotion known to humankind throughout my DPhil. I know I often go out of my way to annoy you guys, but I love you, and my success is largely due to your encouragement, support, and love.

Finally, thank you, Daniel, for everything. You are beyond intelligent, funny, kind, and super silly. You make my heart happy and you make me a better person every day. *Together - to infinity and beyond.*

Abstract

Characterizing the climates of exoplanets— planets orbiting other stars —advances our knowledge of atmospheric science, planetary formation, internal structures and will eventually lead to the holy grail of exoplanet science, detecting biosignatures of alien life. This study focuses on atmospheric convection in super-Earth and sub-Neptune exoplanets, a relatively unexplored topic. We aim to understand how compositional gradients of atmospheric tracers affect stable atmospheric states, the distribution of atmospheric tracers, and cloud formation. We use 3D convection resolving simulations with Cloud Model 1 (CM1) to build a fundamental understanding of how compositional variations influence convection and the atmospheric state in both hydrogen-dominated and higher mean molecular weight exoplanet atmospheres.

We perform modular, idealized simulations with CM1 to study compositional convection. Initially, we examine compositional convection in non-condensing atmospheres without the effects of radiation or other planetary processes. Next, we run simulations where atmospheric tracers can condense, thus incorporating the effect of latent heat release on compositional convection. Lastly, we use CM1 to model a radiative-convective system. Our simulations aim to identify stable atmospheric structures, determine how convection distributes atmospheric tracers, and explore the impact on convective clouds. The CM1 simulation results pave the way for future developments of convection parameterizations for global climate modeling of sub-Neptune and super-Earth exoplanet atmospheres.

Table of Contents

List of Figures xiii

List of Tables xv

1 Introduction 1
- 1.1 Exoplanet Detection Methods . . . 5
- 1.2 Exoplanet Characterization Methods . . . 9
  - 1.2.1 Transmission Spectroscopy . . . 11
  - 1.2.2 Emission Spectroscopy . . . 12
  - 1.2.3 Phase Curve Observations . . . 14
  - 1.2.4 Current Observations of sub-Neptunes & super-Earths . . . 16
- 1.3 3D Modeling of Exoplanet Atmospheres . . . 18
- 1.4 Convection Modeling for Super-Earth & Sub-Neptune Atmospheres . . . 20
- 1.5 An Overview of this Thesis . . . 24

2 Atmospheric Convection 27
- 2.1 Compositional Convection in Planetary Atmospheres . . . 29
  - 2.1.1 High Mean Molecular Weight Atmospheres . . . 29
  - 2.1.2 Hydrogen-Dominated Atmospheres . . . 30
- 2.2 Stability to Atmospheric Convection . . . 33
  - 2.2.1 Convection in Well-Mixed Atmospheres & The Schwarzschild Stability Criterion . . . 34
  - 2.2.2 Non-Condensing Compositional Convection & The Ledoux Local Stability Criterion . . . 37
  - 2.2.3 Condensing Compositional Convection & The Guillot Local Stability Criterion . . . 45
  - 2.2.4 CAPE Analysis . . . 49

3 Modeling Non-Condensing Compositional Convection **51**
3.1 Summary . . . 51
3.2 Compositional Convection Modeling with CM1 . . . 54
3.2.1 High Resolution CM1 Simulations . . . 60
3.2.2 CM1 Parameter Study . . . 62
3.3 CM1 Simulation Results & Discussion . . . 64
3.3.1 High Resolution CM1 Simulation Results Overview . . . 65
3.3.2 Discussion of CM1 Results . . . 72
3.4 Non-Condensing Convection Adjustment Scheme . . . 83
3.5 Conclusions . . . 88

4 Modeling Condensing Compositional Convection **93**
4.1 Summary . . . 93
4.2 Compositional Convection Modeling with CM1 . . . 95
4.2.1 Isothermal Condensing Compositional Convection Simulations . . . 98
4.2.2 Adiabatic Condensing Compositional Convection Simulations . . . 100
4.3 CM1 Simulation Results & Discussion . . . 100
4.3.1 CM1 Results from the Initially Isothermal Simulations . . . 101
4.3.2 CM1 Results from the Initially Adiabatic Simulations . . . 108
4.3.3 Evaluating CM1 Radiative Timescales & Convergence . . . 114
4.4 Conclusions . . . 119

5 Summary and Future Work **121**

Appendix An Overview of Cloud Model 1 **125**

References **135**

List of Figures

1.1 Scatter plot of the detected exoplanet population showing the planetary bulk radius versus effective temperature . . . 2
1.2 Distribution of radii for low mass planets . . . 3
1.3 Schematic of the transit method for exoplanet detection . . . 7
1.4 Schematic of exoplanet atmospheric characterization methods . . . 10
1.5 Comparison of GCM output showing the impact of the representations of convection on the simulated climate of exoplanets . . . 22

2.1 Atmospheric thermal profile with and without considering condensation-driven convective inhibition . . . 31
2.2 Sketch illustrating atmospheric stability to convection . . . 35
2.3 Buoyancy due to finite amplitude displacements of a Ledoux stable atmospheric profile . . . 42

3.1 2D vertical cross-sections of the mass mixing ratio from the Earth air atmosphere non-condensing CM1 simulations. . . . 64
3.2 2D vertical cross-sections of the mass mixing ratio from the H_2 atmosphere non-condensing CM1 simulations. . . . 65
3.3 2D vertical cross-sections of the mass mixing ratio from the CO_2 atmosphere non-condensing CM1 simulations. . . . 66
3.4 Case 1: Final atmospheric state from CM1 non-condensing simulations of an initial isothermal Earth air atmosphere with a water vapor tracer. . . . 69
3.5 Case 2: Final atmospheric state from CM1 non-condensing simulations of an initial isothermal H_2 atmosphere with a water vapor tracer. . . . 70
3.6 Case 3: Final atmospheric state from CM1 non-condensing simulations of an initial isothermal CO_2 atmosphere with a water vapor tracer. . . . 71

3.7 Case 4: Final atmospheric state from CM1 non-condensing simulations of an initial non-isothermal Earth air atmosphere with a water vapor tracer. 72
3.8 Case 5: Final atmospheric state from CM1 non-condensing simulations of an initial non-isothermal H_2 atmosphere with a water vapor tracer. 73
3.9 Case 6: Final atmospheric state from CM1 non-condensing simulations of an initial non-isothermal CO_2 atmosphere with a water vapor tracer. 74
3.10 Parameter study showing how variation in the strength of the compositional gradient at constant temperature affects non-condensing compositional convection. 75
3.11 Parameter study showing how variation in the strength of the temperature gradient with a constant background compositional gradient affects non-condensing compositional convection. 76
3.12 Comparing a non-condensing convective adjustment scheme to CM1 simulations of non-condensing compositional convection. 84

4.1 Atmospheric state for the CM1 simulation without radiation of an initially isothermal atmosphere with $T = 273$ K and an initial state $q_{v,s} \approx q_{\text{crit}}$. 102
4.2 Atmospheric state for the CM1 simulation of an initially isothermal atmosphere with $T = 273$ K and an initial state $q_{v,s} \approx q_{\text{crit}}$. 103
4.3 Atmospheric state for the CM1 simulation of an initially isothermal atmosphere with $T = 300$ K and $q_{v,s} > q_{\text{crit}}$. 106
4.4 Atmospheric state for the CM1 simulation of an initially isothermal atmosphere with $T = 225$ K and $q_{v,s} < q_{\text{crit}}$. 107
4.5 Vertical velocity cross-sections of the four isothermal condensing compositional convection CM1 simulations. 109
4.6 Vertical velocity and condensate mixing ratio cross-sections from the adiabatic CM1 simulation initialized on a moist adiabat. 110
4.7 Vertical velocity and condensate mixing ratio cross-sections of the adiabatic simulation initialized on the dry then moist adiabat. 111
4.8 Atmospheric state for the CM1 simulation of an initially moist adiabatic atmosphere with $T_s = 460$ K and $p_s = 300$ bar. 112
4.9 Atmospheric state for the CM1 simulation of an initially dry then moist adiabatic atmosphere with $T_s = 850$ K and $p_s = 300$ bar. 113
4.10 CM1 Radiative fluxes for the initially isothermal compositional convection simulations. 115
4.11 CM1 Radiative fluxes and estimated radiative timescale for the two initially adiabatic condensing compositional convection simulations. 116

List of Tables

3.1 Atmospheric constants used within the CM1 non-condensing simulations. All simulations use a gravity value of 9.8 m s^{-2}. 55
3.2 Initial atmospheric sounding parameters and domain size used for the CM1 initial value problem simulations. 59

4.1 Atmospheric constants used within the CM1 condensing compositional convection simulations 95
4.2 Initial atmospheric sounding parameters and domain size used for the CM1 condensing compositional convection simulations. 98

1

Introduction

The detection and characterization of a diverse range of exoplanets – planets orbiting other stars – has led to a revolution in planetary science. About 5,557 exoplanets have been detected (as of December 2023; NASA Exoplanet Archive) since the first exoplanet orbiting a sun-like star was discovered in 1995 (Mayor and Queloz, 1995). Exoplanets are typically studied through two main approaches, population or characterization studies. Characterization studies focus on uncovering physical processes of individual exoplanets through atmospheric observations (see Section 1.2). Conversely, population studies look at understanding the distribution and statistical properties of the range of detected exoplanets. In particular, population studies constrain exoplanet occurrence rates and look for trends between various planetary properties such as, effective temperature, planet mass and radius,

orbital period, etc. The current population of detected exoplanets is shown in Fig. 1.1. Current exoplanet detection methods are biased towards detecting planets on short orbits and planets with relatively large radii, so the current population of detected exoplanets is observationally biased.

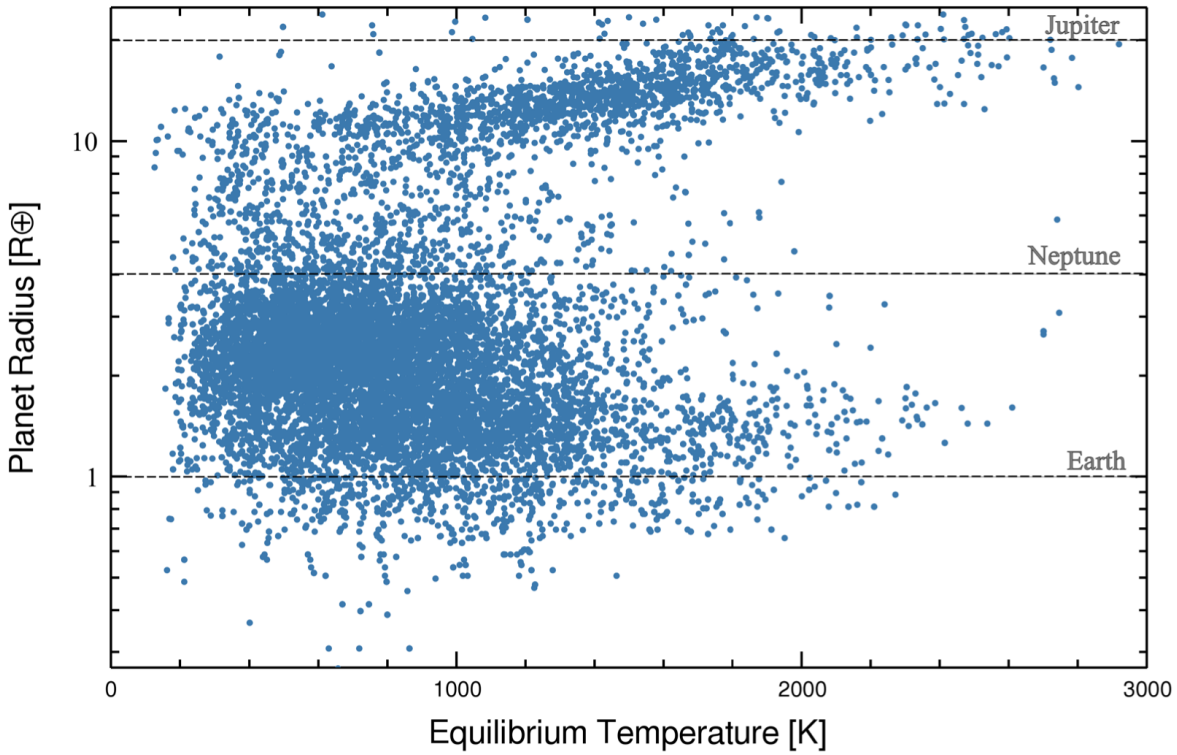

Fig. 1.1 Planet radius versus equilibrium temperature plot of the current sample of detected exoplanets. Lines indicating the radius of Earth, Neptune and Jupiter are shown for comparison. Two distinct exoplanet populations are apparent. First, a population of hot, large planets called hot Jupiters. Second, a more abundant population of exoplanets is observed at radii in between Neptune and Earth. This figure was generated in November 2023 using the NASA Exoplanet Archive[1].

Fig. 1.1 shows two main groups of exoplanets, hot Jupiters and sub-Neptunes. Hot Jupiters are approximately Jupiter-sized exoplanets that are located close to their host stars, close-in, and have atmospheric equilibrium temperatures of ~1000 - 3000 K. Exoplanet population statistics show that close-in exoplanets between the size of Earth and Neptune are the most commonly detected exoplanets. This group of exoplanets is divided into two

[1] https://exoplanetarchive.ipac.caltech.edu/

distinct populations by the “radius valley” (Fulton et al., 2017; Van Eylen et al., 2018; Cloutier and Menou, 2020); the observed gap in the exoplanet size distribution separating a smaller, higher density population from a larger, lower density population as shown in Fig. 1.2. In this work, we will refer to the smaller, higher density planets, $\lesssim$ 1.5 Earth radii ($R_\oplus$), in this population as super-Earths, and the larger, lower density planets, ~1.6 - 3.9 $R_\oplus$ as sub-Neptunes. The radius valley represents the under-abundance of planets between ~1.5 - 2 $R_\oplus$. Approximately 25% of the 4,177 exoplanet detections with known radii are super-Earths, and about 43% are sub-Neptunes (NASA Exoplanet Archive).

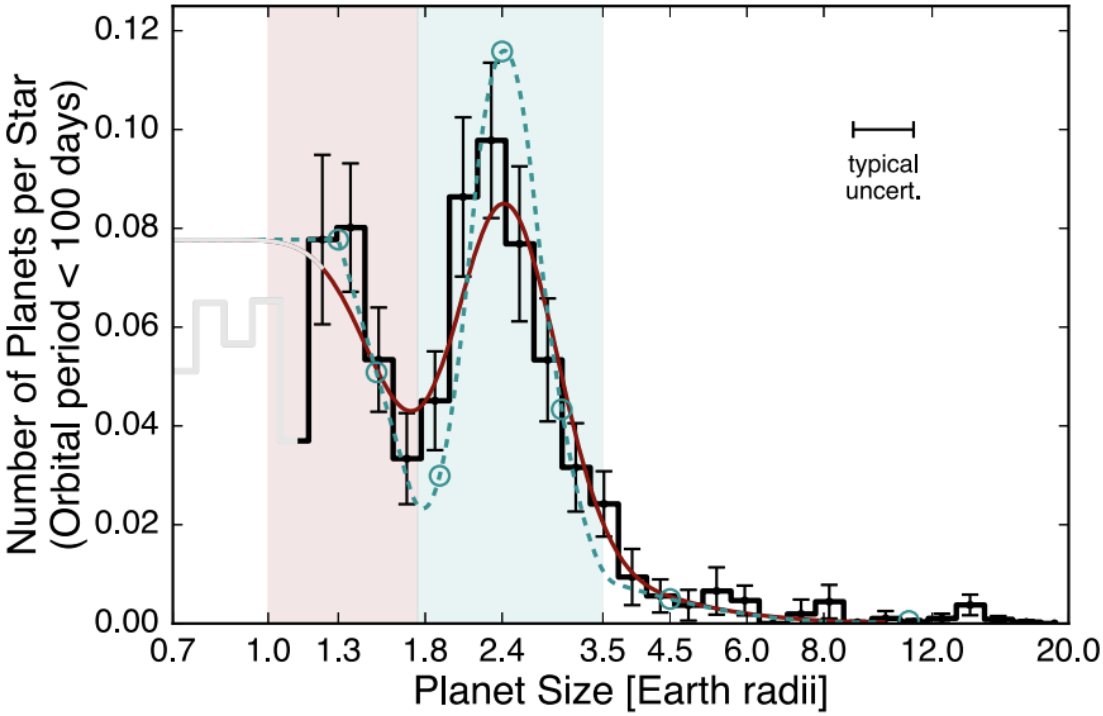

Fig. 1.2 Histogram of planetary radius of close-in planets. The radius distribution of exoplanets shows two clear peaks at ~ 1.3 $R_\oplus$ and 2.4 $R_\oplus$. The “radius valley" at ~ 1.5 - 2 $R_\oplus$ separates the two populations of low mass exoplanets with the higher planet size population corresponding to sub-Neptunes and lower planet size corresponding to super-Earths. This figure is adapted from Fulton et al. (2017)

.

Observations of super-Earth densities suggest a significant rocky core, while super-Earth radii suggest a thin, high mean molecular weight atmosphere, if any atmosphere at all (Seager et al., 2007; Van Eylen et al., 2018). Super-Earth atmospheres are thought to arise from a combination of atmospheric processes, including the accretion of a primary hydrogen atmosphere, atmospheric escape processes leading to the loss of the primary atmosphere, surface outgassing and exchange between the surface and atmosphere (Seager et al., 2007; Elkins-Tanton and Seager, 2008; Owen et al., 2020).

Conversely, given the mass and radii of sub-Neptunes, many interior structures are plausible and have been proposed. A commonly accepted model for sub-Neptune structure, preferred by observational constraints (Rogers and Seager, 2010; Van Eylen et al., 2018), is a planet with a hydrogen-helium-dominated atmosphere over a rocky or ice-rich core. Other proposed sub-Neptune structures include water-rich interiors and atmospheres which match the bulk density of sub-Neptune planets (Luque and Pallé, 2022), and “Hycean Worlds" (Madhusudhan et al., 2021), which are planets with a hydrogen-helium-dominated atmosphere, a water rich interior and large oceans. In this thesis we will use the term sub-Neptune to refer to exoplanets that are $1.6 - 3.9\ R_\oplus$ and have a substantial fraction of hydrogen within the atmosphere. Sub-Neptunes are a prime target for James Webb Space Telescope (JWST) observations, as these observations have the potential to enhance our understanding of these planets and clarify uncertainties in their composition.

In this thesis, I focus on developing a fundamental understanding of atmospheric convection for sub-Neptune and super-Earth exoplanet atmospheres using 3D convection-resolving models. The work presented here is developed in a generalized framework, but I focus on applications to sub-Neptune and super-Earth exoplanets because this group of exoplanets represents the most commonly detected type of exoplanet. Developing models to explain the atmospheric processes of sub-Neptunes and super-Earths can help constrain and inform observations of these worlds. Prior to delving into atmospheric convection, I will

begin by briefly introducing exoplanet detection methods, atmospheric characterization methods, and 3D atmospheric modeling. Understanding the characterizable properties of exoplanets is essential for developing physical models to study exoplanet atmospheres.

1.1 Exoplanet Detection Methods

There are a range of different exoplanet detection methods. Different detection methods vary in their sensitivity to planet sizes and orbits, with each method suited to identifying a specific range of exoplanets. Two of the most commonly used detection methods are planetary transits and radial velocity. We focus on these methods since planets detected through these methods are the ones most suited to atmospheric characterization.

Planetary transits are by far the most common method of detecting exoplanet candidates and presently ~75% of the known 5,557 discovered exoplanets (NASA Exoplanet Archive) are detected using the transit method. Planetary transits look for apparent periodic dimming of the stellar flux caused by a planet passing between its host star and the observer (i.e. the telescope) and blocking a portion of the observed stellar flux (Charbonneau et al., 2002; Madhusudhan, 2018; Fischer et al., 2014). The transit method is shown in Fig. 1.3. The transit depth describes the amount by which the observed stellar flux decreases when a planet transits its host star, and is proportional to the relative size of the planet to its host star. The transit depth, δ, is defined as,

$$\delta \approx \left(\frac{R_p}{R_\star}\right)^2. \tag{1.1}$$

where $R_\star$ and R_p are the radius of the star and transiting planet respectively. If the stellar radius is known for a given planet-star system, the transit method allows to constrain the planetary radius. Additionally, the period of the transit provides the orbital period of the planet.

The transit method is biased towards detecting larger planets such as hot Jupiters. Larger planets block more of the observed stellar flux during a transit, leading to a larger transit depth, thus making these planets easier to detect. To detect smaller exoplanets such as sub-Neptunes and super-Earths, smaller host stars are advantageous. When a planet transits a smaller M-dwarf star, the transit depth is larger because the planet covers a greater fraction of the star compared to if the same planet were orbiting a larger sun-like star. M-dwarf stars are the most common type of star in our galaxy. Many small, nearby M-dwarfs stars have been found to host planetary systems, commonly referred to as the *M-dwarf opportunity*, as many of these planets are suitable candidates for atmospheric characterization. Lastly, the transit method is biased to detect planets with shorter orbital periods because these planets are more likely to transit and will also transit more frequently.

The **radial velocity (RV) method** has found ~19% of the known 5,557 exoplanets (NASA Exoplanet Archive). The RV method looks for planet-induced motion of a host star through periodic Doppler shifts in the stellar spectrum from high-resolution spectroscopy measurements (Wright and Gaudi, 2013; Fischer et al., 2014; Wright, 2017). The host star is not stationary in a planet-star system, but rather, the star will move in a small orbit or “wobble" around the center of mass of the planet-star system. This “wobble" of the host star is detectable through Doppler shifts of the star’s spectrum. The RV method measures the host star’s velocity along the line of sight of the observer, i.e. radial velocity $v_{r,\star}$. The measured radial velocity provides a lower bound on the true stellar orbital velocity, $v_\star$, because the planet-star system inclination, i, affects the Doppler shift but is unknown. The stellar orbital velocity is related to the measured radial velocity by,

$$v_{r,\star} = v_\star \cdot \sin(i). \tag{1.2}$$

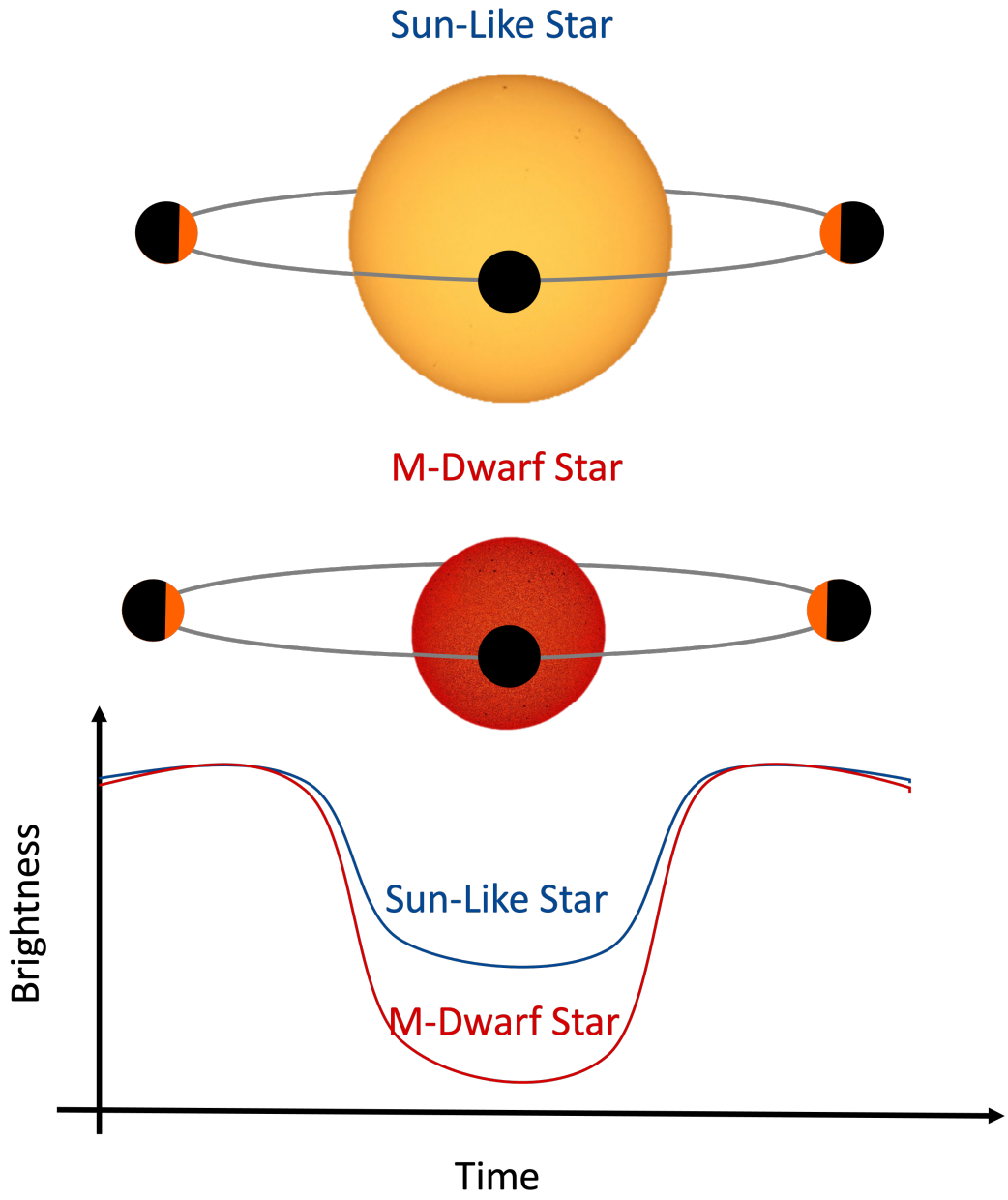

Fig. 1.3 Schematic illustrating the transit method for exoplanet detection. As a transiting exoplanet passes in front of its host star, it will block a fraction of the light of the planet, leading to a dip in the observed brightness. In this figure, we highlight the importance of the stellar size on the transit spectra. The planet size is approximately the same in the top and bottom transit sketches, but as the planet pass in front of the smaller (M dwarf) star, it blocks a larger fraction of the observed stellar light and creates a larger transit depth.

The RV method provides a way to constrain the planet mass. By conservation of momentum,

$$M_\star v_\star = M_p v_p, \tag{1.3}$$

where v_p is the planet velocity, M_p and $M_\star$ are the bulk mass of the planet and star, respectively. The planet velocity is given by,

$$v_p = \frac{2\pi a}{P}, \tag{1.4}$$

where a is the semi-major axis of the planet's orbit and P is the orbital period of the planet. The semi-major axis of the planet's orbit is known through Kepler's third law which states,

$$a \approx \left(\frac{GM_\star P^2}{4\pi^2}\right)^{1/3} \tag{1.5}$$

where G is the universal gravitational constant and assuming $M_\star >> M_p$. Combining Kepler's third law with Eqns. 1.2-1.4 allows to determine a lower bound on the planet mass as,

$$M_p^3 \sin^3(i) \approx \frac{P}{2\pi G \cdot M_\star^2} \cdot v_{r,\star}^3. \tag{1.6}$$

Note the planet's orbital period is measured using the RV method.

The RV method is biased towards detecting planets with larger masses and short orbital periods, as this produces larger Doppler shifts in the stellar spectrum. The first detected exoplanet, 51 Pegasi b, is a hot Jupiter type planet that was found using the RV method (Mayor and Queloz, 1995).

Most exoplanets are detected using the transit method and then followed up with RV measurements. There is a chance of false-positive detections when using the transit method. Therefore, planet candidates identified through the transit method are typically followed up with alternative exoplanet detection methods, primarily the RV method. If an exoplanetary

system is transiting, it is possible to constrain the both the planet's radius and mass with the transit and RV methods. The combined measurements of a planet's mass and radius provide constraints on its surface gravity and density. The planet's density constraints can be used to provide insights into the bulk composition and interior structure of the exoplanet.

1.2 Exoplanet Characterization Methods

In the past decade, exoplanet science has moved from an era of detecting exoplanets to an era of exoplanet atmospheric characterization. In this section, I summarize three common methods used for exoplanet atmospheric characterization: transmission spectroscopy, emission spectroscopy, and phase curve observations (see reviews by Seager and Deming, 2010; Kreidberg, 2017; Madhusudhan, 2019). I will end this section with a brief discussion of current observations of sub-Neptune and super-Earth exoplanets. Again, there are other methods of exoplanet atmospheric characterization but I limit the discussion here to focus on the characterization methods that are presently used and able to characterize sub-Neptune and super-Earth exoplanets.

Phase curve observations, transmission and emission spectroscopy all require the exoplanet being observed to be transiting. Often, transiting exoplanets are *tidally locked* meaning the planet always shows the same face to its host star since the planet's rotation period is the same as its orbital period. Tidally locked exoplanets have a permanent day and night-side. These three characterization methods, transmission, emission, and phase curves, probe different parts of an exoplanet's atmosphere at various stages in the planet's orbit. A summary of the three characterization methods discussed here is shown in Fig. 1.4.

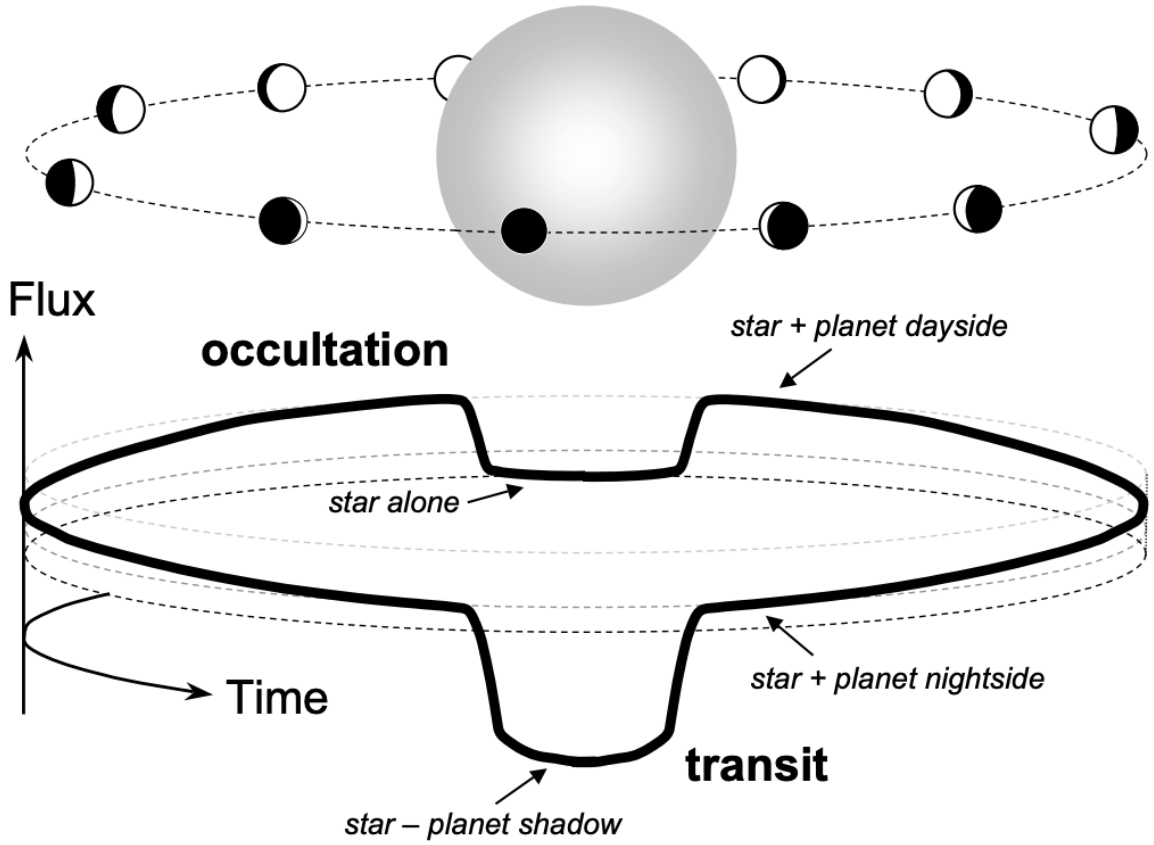

Fig. 1.4 Schematic of Exoplanet Characterization Methods showing the transiting planet passing in front of its star (primary transit), behind the star in secondary eclipse or occultation and the phase of the tidally locked planet as it orbits its host star. Transmission spectroscopy measures the transit depth at multiple wavelengths and probes the size of the planet at different wavelengths, molecular features and clouds and hazes present in the day-to-night terminator region of the atmosphere. Emission spectroscopy measures the ratio of planetary to stellar flux and probes the thermal emission, atmospheric composition and albedo of the planet's day-side. Lastly, phase curves observe the ratio of planetary to stellar flux of the transiting exoplanet through the full duration of its orbit and constrain atmospheric transport processes and the longitudinal temperature structure. This figure is adapted from Winn (2010).

1.2.1 Transmission Spectroscopy

Transmission spectroscopy involves observing an exoplanet as it transits its host star and measuring the transit depth at multiple wavelengths. As a planet transits, light from the host star is blocked by the bulk of the planet, but some star light is able to pass through the planet's atmosphere at the day-night terminator. The day-night terminator is the atmospheric region that separates the day-side and the night-side of an exoplanet. The atmosphere of the planet creates a small, wavelength dependent variation in the flux observed from the star-planet system due to atmospheric species preferentially absorbing light at various wavelengths. For instance, at one wavelength, the planet's atmosphere might absorb more of the star's light, making the planet appear larger and resulting in a greater transit depth compared to another wavelength. The transmission spectrum is the variation in the transit depth, Eqn. 1.1, as a function of wavelength. The transmission spectrum provides an indication of the molecular species present within the planetary atmosphere and thus provides information about the composition of the atmosphere.

The transit depth is sensitive to the atmospheric scale height. At a wavelength where the atmosphere is fully opaque, the effective radius of the planet measured by the transit depth is $R_{p,\,\mathrm{eff}} = R_p + H_A$, where R_p is the radius of the optically thick portion of the planet, such as the surface of a rocky planet, and H_A is the atmospheric height where $R_p >> H_A$. The difference in the transit depth when the atmosphere is fully transparent ($R_{p,\,\mathrm{eff}} = R_p$) and when the atmosphere is fully opaque ($R_{p,\,\mathrm{eff}} = R_p + H_A$) is,

$$\Delta = \left(\frac{R_p + H_A}{R_\star}\right)^2 - \left(\frac{R_p}{R_\star}\right)^2 \approx \frac{2R_p H_A}{R_\star^2}. \tag{1.7}$$

The atmospheric height is proportional to the atmospheric scale height,

$$H = \frac{k_B T}{\mu g}, \tag{1.8}$$

where k_B is the Boltzmann constant, T is the temperature, μ is the mean molecular weight of the atmosphere and g is gravitational acceleration. An important consequence of Eqns. 1.7 - 1.8 is that the transit depth increases with increasing atmospheric scale height. Therefore, hotter and or lower mean molecular weight atmospheres are more observable with transmission spectroscopy, since these exoplanets will have larger features in transmission spectra. Sub-Neptunes are more favorable to be characterized with transmission spectroscopy than super-Earths due to their hydrogen-dominated atmospheres. Super-Earth exoplanets with high mean molecular weight atmospheres will be hard to characterize with transmission spectroscopy due to smaller features in the spectra unless the super-Earth is very close-in to its host star and the effective temperature of the planet is high, i.e. 55 Cnc e with $T_{\rm eff} \approx 2700$ K.

A flat transmission spectrum implies either that the exoplanet does not have an atmosphere or the exoplanet's atmosphere has strong cloud and or haze cover. Clouds and hazes, depending on their size distributions, will make the atmosphere opaque over a wide range of wavelengths and prevent the detection of any spectral features due to atmospheric species. Observations of various exoplanets suggests clouds are ubiquitous in planetary atmospheres. Famously, the sub-Neptune exoplanet GJ-1214b was observed with the *Hubble Space Telescope* (HST), and found to have a completely flat transmission spectra (Kreidberg et al., 2014a). Follow-up observations of this exoplanet with JWST again showed a flat transmission spectra, but an atmosphere on this planet has been confirmed through emission spectroscopy and phase curve observations (Kempton et al., 2023).

1.2.2 Emission Spectroscopy

Emission spectroscopy observes the planet's day-side thermal flux relative to the stellar flux as the planet goes behind its host star during secondary eclipse. Emission spectroscopy measures the flux for the planet-star system, $f_\star + f_p$, right before the secondary eclipse and

also the flux solely from the star, $f_\star$, when the planet is behind the star. Taking the ratio of the flux outside and during the eclipse as a function of wavelength gives the emission spectrum of the planet. The measured quantity of the emission spectrum is the ratio of the thermal flux of the planet relative to the star $f_p/f_\star$ as a function of wavelength.

Planetary emission spectra display a range of spectral features due to the absorption and emission by atmospheric molecular species (Kreidberg, 2017). Emission spectroscopy, like transmission spectroscopy, offers insights into the atmospheric composition of the observed exoplanet. However, emission spectroscopy can probe deeper layers of planetary atmospheres compared to transmission spectroscopy. By combining emission and transmission spectral data, it is possible to more precisely constrain the abundances of different molecules in the atmosphere (Kreidberg et al., 2014b). Further, spectral features in the emission spectra are highly sensitive to the atmospheric temperature gradient. Spectral features are observed in absorption when the atmospheric temperature is *decreasing* with height, and conversely in emission with the atmospheric temperature is *increasing* with height. Therefore, emission spectra have the potential to constrain if exoplanet atmospheres have thermal inversions, when the atmospheric temperature increases with height, like in the Earth's stratosphere.

The secondary eclipse signal is largest for hotter, larger planets. To first order, $f_p/f_\star$ can be approximated as,

$$\frac{f_p}{f_\star} = \frac{R_p^2 \cdot B(\lambda, T_p)}{R_\star^2 \cdot B(\lambda, T_\star)}, \tag{1.9}$$

where $B(\lambda, T)$ is the black body Planck function, λ is the wavelength, T_p is the temperature of the planet, and $T_\star$ is the temperature of the star. The Planck function is defined as,

$$B(\lambda, T) = \frac{2hc^2}{\lambda^5} \frac{1}{\exp\left(\frac{hc}{\lambda k_B T}\right) - 1}, \tag{1.10}$$

where h is Planck's constant and c is the speed of light in a vacuum. $B(\lambda, T_p)$ peaks at longer wavelengths than $B(\lambda, T_\star)$. Planetary flux peaks in the infrared, therefore, emission spectra are often observed at infrared wavelengths. Eqn. 1.9 shows the largest eclipse signal is for either larger planets or planets orbiting a smaller host star, such as an M-dwarf.

1.2.3 Phase Curve Observations

Full phase light curves (or phase curves), observe an exoplanet through the entirety of its orbit and can provide longitudinal information about the thermal emission of the exoplanet and the reflected stellar light (Knutson et al., 2007; Parmentier et al., 2016; Parmentier and Crossfield, 2017). The observed flux of the planet-star system, $f_p/f_\star$, as a function of time is the phase curve. Most close-in transiting exoplanets are assumed to be tidally-locked, so as the planet orbits its host star, the phase of the planet facing the observer changes and therefore, the amount of planetary flux observed also changes (see Fig. 1.4).

Phase curve observations are highly sensitive to the wavelength. Different wavelength phase curve observations probe different atmospheric regions and processes. There are two main phase curve observations; (1) thermal flux which is observed at infrared wavelengths and (2) reflected light which is measured at optical wavelengths (Parmentier et al., 2016). The reflected light contribution to the phase curve probes the amount of light reflected from the planet and provides constraints about the albedo and cloud distribution on the day-side of the exoplanet.

The thermal phase curve constrains the thermal emission of the planetary atmosphere. The planet emits more light where it is hotter, therefore the shape of the thermal phase curve indicates the hottest and coldest parts of the planet. Phase curves with a large amplitude, the difference between the maximum and minimum observed flux, suggest that the atmosphere is inefficient at redistributing heat from the day-side to the night-side of the planet. Conversely, phase curves with a small amplitude suggest the atmosphere is more efficient at

distributing heat around the planet (Parmentier and Crossfield, 2017). The day-to-night flux contrast can be used to infer the average day-to-night brightness temperature difference, assuming the planet radiates like a black body. Mechanisms that regulate phase curve amplitudes are linked to atmospheric dynamics (Showman and Guillot, 2002; Cowan and Agol, 2010; Perez-Becker and Showman, 2013; Komacek and Showman, 2016). Additionally, the phase curve offset, the difference in time between the maximum flux and the eclipse, has also been used to infer and constrain atmospheric dynamics. Again, like transmission and emission spectroscopy, phase curves observations have the largest signal for larger and hotter exoplanets.

In summary, transmission spectroscopy can be used to infer the presence of different atmospheric molecular species and constrain the total mean molecular weight of an exoplanet atmosphere. Emission spectroscopy probes the day-side of an exoplanet atmosphere and can provide information about the composition and atmospheric thermal gradient. Phase curves provide longitudinal information about the thermal structure and cloud distribution of exoplanets and can constrain the albedo and day-to-night temperature contrast.

The main focus of this thesis is developing atmospheric convection theory and models. Atmospheric convection plays a fundamental role in (1) cloud formation, (2) the vertical mixing and distribution of atmospheric tracers, and (3) the vertical temperature profile. All three of these aspects influence exoplanet atmospheric observations using the three methods discussed here, either directly or indirectly. The main question this thesis aims to address is what is the compositional distribution of atmospheric tracers and temperature profile in super-Earth and sub-Neptune atmospheres. We do not look to explicitly model individual exoplanets but rather, we aim to improve our understanding of atmospheric convection to determine the atmospheric structure of sub-Neptune and super-Earth exoplanets and how this might affect observations of atmospheres around sub-Neptune and super-Earth exoplanets.

1.2.4 Current Observations of sub-Neptunes & super-Earths

Earlier observations of sub-Neptunes were primarily limited to transmission spectroscopy in infrared and optical wavelengths using Hubble Space Telescope (HST) and the Spitzer Telescope. JWST was launched in December 2021 and covers a wider wavelength range in the infrared and a higher resolution compared to both Hubble and Spitzer. Presently, there are still limited observations of sub-Neptunes and super-Earths but future JWST observations will enable us to learn more about these exoplanets. In this section, I provide an overview of various observations of sub-Neptune and super-Earth exoplanets. This section is not a comprehensive list of all exoplanet atmospheric observations but rather this discussion aims to highlight our current capabilities and understanding of sub-Neptune and super-Earth exoplanets. Mass, radius and temperature estimates for the following planets are taken from the IAC community database for exoplanet atmospheric observations (`https://research.iac.es/proyecto/exoatmospheres/index.php`).

HST transmission spectroscopy observations of the sub-Neptune K2 18 b (2.6 $R_\oplus$, 8.9 $M_\oplus$, $T \approx 284$ K) suggested a hydrogen-helium-dominated atmosphere with the presence of water vapor and clouds within its atmosphere (Benneke et al., 2019b; Tsiaras et al., 2019). The water vapor detection in the atmosphere of K2 18 b was contested and Bézard et al. (2022) suggested the spectral signatures were due to methane rather than water vapor. Follow-up transmission spectroscopy observations of K2 18 b with JWST have suggested strong detection of methane and carbon dioxide in a hydrogen-dominated atmosphere, and found a non-detection of both water vapor and ammonia (Madhusudhan et al., 2023).

Additionally, HST transmission spectroscopy observations of the sub-Neptune GJ 1214 b (2.7 $R_\oplus$, 8.2 $M_\oplus$, $T \approx 596$ K) revealed a flat near-infrared spectrum, suggesting the presence of clouds or hazes within this sub-Neptune's atmosphere (Kreidberg et al., 2014a). GJ 1214 b was also followed up with JWST phase curve observations, which suggest a highly reflective

layer of clouds or haze in the atmosphere and a potential water vapor detection (Kempton et al., 2023).

Other observations of sub-Neptunes include; HST and Spitzer telescope transmission and emission observations of GJ 3470 (4.3 $R_\oplus$, 12.6 $M_\oplus$, $T \approx 593$ K) which suggested a hydrogen-dominated atmosphere with a potential water vapor detection (Benneke et al., 2019a). HST transmission observations of 55 Cnc e (1.8 $R_\oplus$, 8.5 $M_\oplus$, $T \approx 2000$ K) have suggested a hydrogen-rich atmosphere with a HCN detection (Tsiaras et al., 2016). Demory et al. (2016) presented phase curve observations of 55 Cnc e and showed a strong day-to-night temperature contrast and constrained the day and night-side brightness temperature.

JWST is facilitating more observations of sub-Neptune worlds, with many observations already scheduled for the current and upcoming JWST cycles. As highlighted in the introduction, the composition and interior structure of sub-Neptune worlds still remains largely unknown. Current observations suggest sub-Neptunes have hydrogen-rich atmospheres with clouds and or hazes. Observations by JWST will enable us to better learn of sub-Neptune compositions, thereby providing insights into their atmospheres.

Super-Earth observations are more challenging than sub-Neptune exoplanets due to their smaller, higher mean molecular weight atmospheres. HST transmission spectrum observations of GJ 1132 b (1.1 $R_\oplus$, 1.6 $M_\oplus$, $T \approx 580$ K) suggested a detection of HCN and CH_4 in a low mean molecular weight atmosphere (Swain et al., 2021). However, other studies have suggested a water-rich (Southworth et al., 2017) and even non-water dominated high mean molecular weight atmosphere (Diamond-Lowe et al., 2018) for GJ 1132 b.

Recent JWST transmission observations of GJ 486 b (1.3 $R_\oplus$, 2.8 $M_\oplus$, $T \approx 700$ K; Moran et al., 2023) suggested a potential water-rich atmosphere, however, Moran et al. (2023) do not rule out contamination from the stellar spectrum. JWST transmission and emission spectra of TRAPPIST 1b (1.1 $R_\oplus$, 0.86 $M_\oplus$, $T \approx 400$ K) have suggested no planetary atmosphere (Greene et al., 2023). Additionally, JWST emission spectra of TRAPPIST 1c (1.1 $R_\oplus$,1.4 $M_\oplus$,

$T \approx 341$ K) rule out a thick CO_2 atmosphere and suggest the observations are consistent with either a bare rock planet or a thin atmosphere (Zieba et al., 2023). Similarly, transmission observations of LHS 475 b (0.95 $R_\oplus$, 0.91 $M_\oplus$, $T \approx 586$ K) rule out a thick atmosphere and are more consistent with high altitude clouds, a tenuous atmosphere or no atmosphere at all (Lustig-Yaeger et al., 2023).

Even in the JWST era, super-Earth atmospheres are challenging to constrain and detect. At present, current observations suggests that super-Earths may not have atmospheres at all, or if they do, super-Earth atmospheres are cloudy and thin. Nonetheless, future observations of super-Earths are planned in the upcoming JWST cycles and hopefully, will be able to conclusively detect atmospheres around these worlds.

1.3 3D Modeling of Exoplanet Atmospheres

3D atmospheric modeling with General Circulation Models (GCMs) allows to study planetary climate and characterize the environments of individual exoplanets. An advantage of GCMs over 1D or 2D atmospheric models is their ability to self-consistently model multiple complex atmospheric processes and the interactions between them. GCMs provide a way to study 3D-effects and coupling of different atmospheric feedbacks and processes. Key atmospheric processes that can be accounted for in GCMs include large-scale atmospheric circulation, radiative transfer, convection, turbulence, surface processes, volatile condensation, precipitation, cloud processes and microphysics (Shields, 2019). The heart of GCMs is a dynamical core which solves the primitive fluid dynamics equations on a rotating sphere. The dynamical core is coupled to representations of physical forcings which solve for additional atmospheric processes such as convection, radiation and cloud microphysics. GCMs can be run to model a range of complexity, from simple models which focus on capturing the physics of key processes (e.g. Kaspi and Showman, 2015) to more comprehensive and

detailed representations that account for interactions of multiple atmospheric processes (e.g. Drummond et al., 2019).

GCM studies are used to understand the general climate regimes and atmospheric circulation for various classes of exoplanets, aid in interpreting observational data for specific exoplanets, and for terrestrial exoplanets are also used to determine climate conditions required for habitability, defined as whether liquid water can exist on the surface of a planet (e.g. Leconte et al., 2013; Popp et al., 2016; Wolf, 2017; Wolf et al., 2017).

GCM studies of sub-Neptunes have primarily focused on K2 18 b (Charnay et al., 2021; Innes and Pierrehumbert, 2022) and GJ 1214 b (Menou, 2011; Kataria et al., 2014; Charnay et al., 2015a; Zhang and Showman, 2017; Drummond et al., 2018; Mayne et al., 2019). GCM studies of GJ 1214 b have been centered on understanding the impact of atmospheric composition by varying the metallicity (the proportion of elements heavier than hydrogen and helium, often expressed in units of $Z_{\odot} = 0.0134$) on the planetary circulation (Menou, 2011; Kataria et al., 2014; Zhang and Showman, 2017; Drummond et al., 2018). All studies generally agree that increasing metallicity leads to a larger day-to-night temperature contrast. Additionally, Charnay et al. (2015a,b) modeled the predicted vertical mixing and the influence of clouds on the atmospheric dynamics and spectra of GJ 1214 b.

Super-Earth GCM studies typically focus on developing theoretical understandings of the climate of terrestrial exoplanets and how different climate regimes would affect exoplanet observables. For instance, Haqq-Misra et al. (2018); Komacek and Abbot (2019) used GCM simulations to determine how changes in a priori unknown planetary properties would affect the atmospheric circulation and expected phase curves of terrestrial planets orbiting M-dwarfs (Haqq-Misra et al., 2018; Komacek and Abbot, 2019) and Sun-like stars (Komacek and Abbot, 2019). Planetary properties characterized in these GCM studies include incident stellar flux, planetary rotation rate, atmospheric mass, surface gravity, cloud particle size and distribution, etc.

Typically, GCMs used to model super-Earth and sub-Neptune exoplanets are nationally or institutionally developed Earth GCM models which have been adapted for general planetary applications. A benefit of modifying Earth-centric GCMs for planetary applications is that these models leverage existing code frameworks. However, super-Earth and sub-Neptune GCMs do inherit modules for atmospheric processes that are optimized or tuned specifically for modeling Earth and match the abundant observational data we have of Earth. These Earth-centric atmospheric process modules may not necessarily be representative of exoplanet climates and can be difficult to constrain due to the limited information from exoplanet observations. In this thesis, we will focus on the representation of atmospheric convection.

1.4 Convection Modeling for Super-Earth & Sub-Neptune Atmospheres

Atmospheric convection refers to vertical motions in the atmosphere driven by gravity acting upon variations on the density distribution in the atmosphere, also known as buoyancy. Convection is an efficient method of transporting energy and trace gases vertically in the atmosphere. Density variations in the atmosphere are due to either temperature (thermal convection) or compositional (compositional convection) variations. Convection can arise in the atmosphere due to radiation heating the surface or cooling aloft, but could also arise from variations of compositional gradients of atmospheric tracers. The condensation of atmospheric tracers during convection, known as moist convection, plays a significant role in the formation of precipitation and cloud processes. Conversely, dry convection refers to convective mixing where atmospheric tracers are sub-saturated or do not undergo phase changes within the temperature-pressure range of the atmosphere.

Representation of convection within GCMs is a known source of uncertainty (Sergeev et al., 2020; Fauchez et al., 2020, 2022; Sergeev et al., 2022; Turbet et al., 2022) in climate modeling of exoplanet atmospheres, especially for smaller $1 - 10\ R_\oplus$ sized planets. GCMs resolve planetary atmospheric circulations on the order of hundreds of km, whereas convection can occur on the order of meter to kilometer length scales. Therefore, convection is parameterized in GCMs. There are two main types of convection parameterizations, convective adjustment schemes and mass flux parameterizations.

Convective adjustment schemes adjust the vertical atmospheric sounding state to a marginally stable state while conserving enthalpy. In most cases, the marginally stable state in convective adjustment schemes is defined to be a moist or dry adiabat. Alternatively, mass-flux parameterizations simulate the statistical effect of convective plumes without resolving convection (Arakawa, 2004). Mass flux schemes are considered to be more representative of convection, and are more commonly used in climate models. However, mass flux schemes are based on years of Earth convection data and are often “tuned" to model present-day Earth.

Sergeev et al. (2020) compared GCM outputs for two terrestrial exoplanets, Proxima-b and TRAPPIST-1e, using convective adjustment, mass-flux convection schemes, and a high resolution convection permitting model. Their study showed that convective adjustment schemes predicted higher atmospheric temperatures and enhanced zonal flows compared to mass flux schemes. However, mass-flux convection schemes cannot be taken as ground-truth for modeling exoplanet atmospheres since they contain free parameters that are difficult to tune without access to detailed observations such as those available for Earth. Fig. 1.5 shows a sample plot from Sergeev et al. (2020) study highlighting the difference in surface temperature and winds when using different convection schemes. Additionally, Sergeev et al. (2020) performed simulations which used a convection permitting model in a nested grid configuration with their GCM. Their study suggests that convection parame-

terization schemes overestimate the average day-to-night temperature contrast relative to convection permitting simulations. Sub-Neptune GCMs typically use convective adjustment schemes (e.g. Menou, 2011; Mayne et al., 2019) whereas super-Earth GCM studies use both convective adjustment and mass-flux parameterizations (e.g. Wolf et al., 2017; Sergeev et al., 2020).

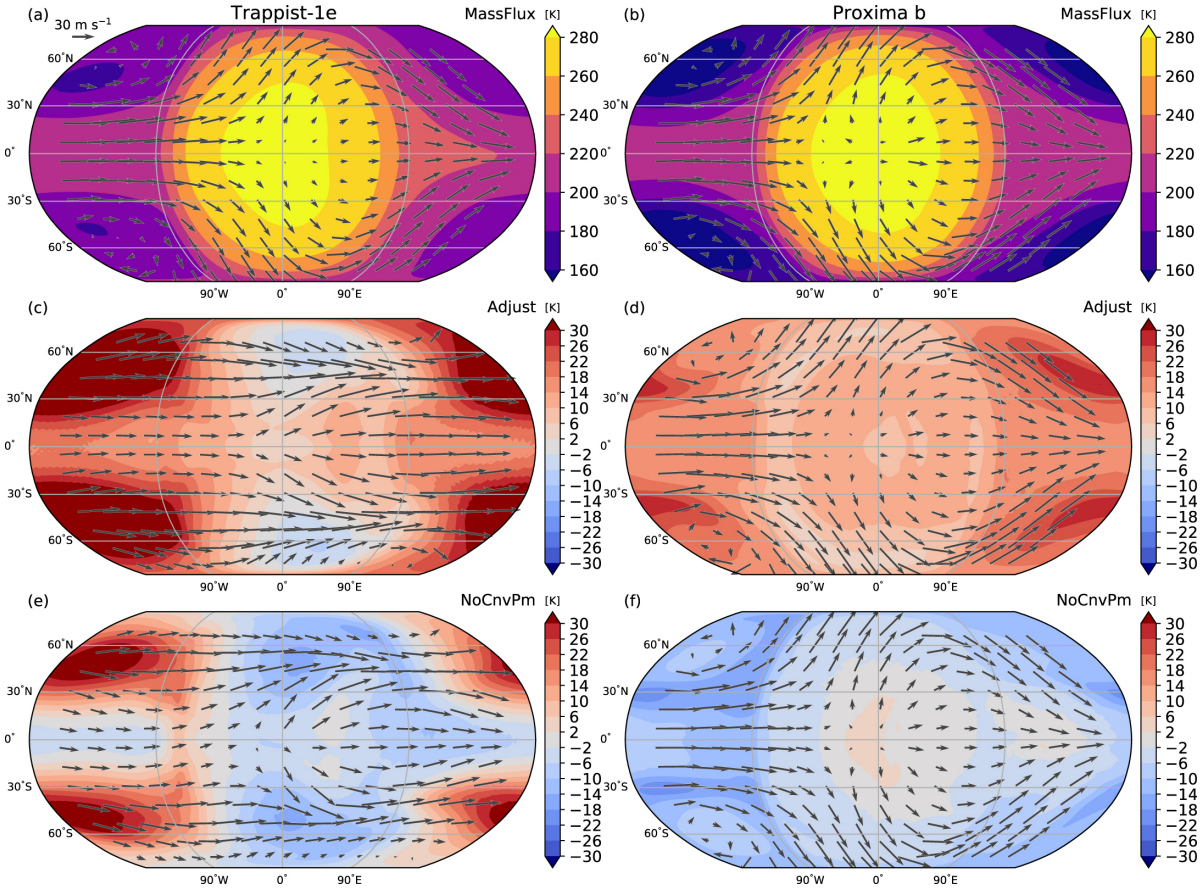

Fig. 1.5 A comparison of output GCM surface temperature [K] (shading) and horizontal wind vectors at 250 hPa (arrows) using three different representations of convection for two super-Earth exoplanets, TRAPPIST-1e (left column) and Proxima-b (right column). The top row shows simulated GCM output when using a mass flux scheme, the middle row shows simulated GCM output when using the convective adjustment scheme, and the bottom row shows the GCM output when using no convection scheme at all. All cases use the Met Office Unified Model (UM). The middle and bottom row show the difference in the surface temperature relative to the top row. This figure is adapted from Sergeev et al. (2020).

Further, the TRAPPIST-1 Habitable Atmosphere Intercomparison (THAI) Protocol (Fauchez et al., 2020, 2022; Turbet et al., 2022; Sergeev et al., 2022) compared 3D climate modeling out-

put from four GCMs (ExoCAM, LMD-Generic, ROCKE-3D, and UM) that are commonly used to model rocky exoplanets. The THAI study showed that all four GCMs predicted similar climate but differ in the details of the climate regime (Turbet et al., 2022; Sergeev et al., 2022). In particular, Sergeev et al. (2022) showed that cloud and convection parameterizations are one of the major sources of the differences within the 3D simulated climate output from the four GCMs. The THAI study revealed a significant sensitivity in the predicted climate when using various convection schemes in GCMs, emphasizing the need for a deeper theoretical understanding of convection in exotic exoplanet conditions. The THAI study focused on terrestrial like exoplanets, but further GCM intercomparison projects are underway for sub-Neptunes (Christie et al., 2022). The THAI study illustrates the need to improve our understanding and modeling of atmospheric convection so we can better represent and study the climate of exoplanet atmospheres.

Convection parameterizations for exoplanet atmospheres are challenged by the greater diversity of exoplanet atmospheric compositions compared to Earth. For many sub-Neptune and super-Earth atmospheres, the effects of vertically inhomogeneous atmospheric trace gases on convection are important (Guillot, 1995; Leconte et al., 2017; Li and Ingersoll, 2015; Markham et al., 2023). Compositional convection is a convective process in which buoyancy is significantly influenced by the compositional gradient of atmospheric tracers. In Earth's present atmosphere, H_2O has a lower molecular weight compared to N_2 and contributes slightly to the positive buoyancy of an air parcel. The compositional convection effect in Earth's atmosphere is small, but has been shown to significantly affect Earth's climate in the tropics (see Seidel and Yang, 2020; Yang and Seidel, 2020). In higher mean molecular weight atmospheres, such as CO_2-dominated atmospheres, water vapor further enhances the positive buoyancy of an atmospheric air parcel leading to a larger compositional buoyancy effect.

Conversely, in sub-Neptune exoplanets with primarily H_2-dominated atmospheres, convection can be inhibited by the greater density of atmospheric tracers compared to the background air (Guillot, 1995; Leconte et al., 2017). When accounting for compositional gradients of water vapor and other atmospheric tracers in the H_2-dominated atmospheres of the Solar System giant planets, Leconte et al. (2017) showed that the planetary deep atmospheric temperature can be hundreds of kelvin hotter than predicted by a moist or dry adiabat. Hotter deep atmospheric temperatures impact our understanding of planetary interior chemistry, evolution, and habitability for terrestrial exoplanets. Previous studies of convective inhibition due to compositional gradients have focused on modeling the Solar System giant planets (Guillot, 1995; Leconte et al., 2017; Li and Ingersoll, 2015). However, compositional convection within H_2-dominated atmospheres is relevant for sub-Neptune atmospheres, terrestrial planets with a persistent H_2 supported greenhouse warming such as those discussed in Pierrehumbert and Gaidos (2011), and transient primordial H_2 atmospheres that have accreted on rocky planets while the protoplanetary disk is still present (Young et al., 2023).

1.5 An Overview of this Thesis

The main objective of this work is to study how compositional convection impacts the expected atmospheric temperature structure and compositional profile of tracers in sub-Neptune and super-Earth atmospheres. We use an open source, convection resolving model, Cloud Model 1 (CM1; Bryan, 2009), to perform idealized 3D compositional convection simulations. The simulations we performed within this work are simplified and not fully representative of planetary atmospheres we aim to study, but they are important to build a foundation for understanding compositional effects on convection and the atmospheric state of sub-Neptune and super-Earth exoplanets.

In Chapter 2 we review atmospheric thermodynamics theory and background relevant for this work. Chapters 3 and 4 show results from our 3D compositional convection simulations. We start by studying compositional convection in its simplest form without condensation and radiation in Chapter 3. In our non-condensing simulations we explore how compositional gradients in planetary atmospheres affect the stable atmospheric state after convective mixing in both high mean molecular weight atmospheres and hydrogen-dominated atmospheres. Additionally, in Chapter 3, we also present a simplified 1D convective adjustment scheme that can be used in GCMs to represent compositional convection in super-Earth and sub-Neptune atmospheres.

Building upon this work, in Chapter 4 we characterize the effect of condensation and radiation on compositional convection in hydrogen-dominated atmospheres using 3D convection resolving simulations. We focus on H_2-rich atmospheres in Chapter 4 to explore how convective inhibition due to compositional gradients affects the atmospheric structure of exoplanets with H_2-rich atmospheres. Lastly we provide a summary of the work presented in this thesis and discussion of future work in Chapter 5.

2

Atmospheric Convection

Atmospheric convection is fluid flow driven by gravity acting upon variations in the vertical distribution of density within the fluid, i.e. buoyancy. Buoyancy is defined as,

$$B = -g\left(\frac{\rho'}{\rho_0}\right), \tag{2.1}$$

where g is the gravitational acceleration of the planet, ρ' is the perturbation in density relative to a base state, ρ_0 (See Emanuel, 1994, Chap. 1). Density variations in the atmosphere are due to either temperature or compositional variations.

Differences between the molecular weight of an atmospheric tracer relative to the bulk background air influences the buoyancy and convective mixing within the atmosphere. At the same temperature and pressure, an air parcel of pure background air will have a

different density than a parcel of some mixture of background air with an atmospheric tracer. The effects of atmospheric tracers on convection (also called virtual effects) are typically represented using virtual temperature,

$$T_v = T\left(\frac{1+q_v/\epsilon}{1+q_v}\right), \tag{2.2}$$

where T is the atmospheric temperature (K), q_v is the mass mixing ratio of the atmospheric tracer (kg/kg), and $\epsilon = M_v/M_b$ is the ratio of the mean molecular weight of the atmospheric tracer to the background atmosphere. Virtual temperature represents the temperature a parcel of pure background air would need to have in order to have the same density as a parcel of some mixture of background air with an atmospheric tracer. Effectively, T_v represents density in units of temperature and allows us to write the ideal gas law as $P = \rho R_b T_v$ where R_b is the gas constant for the background atmosphere and ρ is the total atmospheric density. The mass mixing ratio quantifies how much atmospheric tracer is present relative to the background air and is defined as the ratio of the density of the atmospheric tracer (ρ_v) relative to the background atmosphere density (ρ_b),

$$q_v = \rho_v/\rho_b. \tag{2.3}$$

If the atmospheric tracer has a lower mean molecular weight than the bulk atmosphere $\epsilon < 1$, then $T_v > T$ and the atmospheric tracer can *enhance* buoyancy relative to a parcel of pure background atmosphere at the same temperature. Conversely, when $\epsilon > 1$ and the atmospheric tracer is heavier than the background atmosphere and it can *suppress* convection from occurring. Compositional convection is often overlooked because the compositional convection effect is relatively small in Earth's N_2-dominated atmosphere. However, compositional convection effects are significant for H_2-dominated atmospheres,

such as those of sub-Neptunes, and can be important for high mean molecular weight atmospheres of super-Earths due to the greater diversity of compositions relative to Earth.

In this chapter, we first review literature about compositional convection for high mean molecular weight atmospheres where $\epsilon < 1$, such as Earth's atmosphere, and then for H_2-dominated atmospheres where $\epsilon > 1$. We conclude this chapter with a discussion of atmospheric stability to convection when considering compositional gradients.

2.1 Compositional Convection in Planetary Atmospheres

2.1.1 High Mean Molecular Weight Atmospheres

Water vapor gradients can enhance buoyancy in Earth's atmosphere. However, the relative difference between the mean molecular weight of water vapor and Earth's background atmosphere is small. Further, water vapor makes up a small fraction of Earth's atmosphere. This means that the compositional convection effect in Earth's atmosphere is relatively small and often neglected. Nonetheless, compositional convection has been shown to have a significant impact on Earth's climate in the tropics (Yang and Seidel, 2020; Seidel and Yang, 2020). Yang and Seidel (2020) proposed that compositional convection effects can stabilize the climate in Earth's tropics and lead to an increase in the amount of energy emitted to space. Seidel and Yang (2020) verified the proposed model of Yang and Seidel (2020) using 3D convection resolving simulations and showed that the magnitude due to compositional convection feedback compares to other climate feedbacks in Earth's atmosphere.

There are limited studies of compositional convection in high mean molecular weight exoplanet atmospheres. Daley-Yates et al. (2021) used idealized 3D hydrodynamics simulations to study compositional convection for hot, rocky exoplanets. Within their simulations, they imposed a constant compositional gradient in the atmosphere by incorporating the chemical reaction $CO + O \leftrightharpoons CO_2$ where CO_2 is preferentially produced in the upper atmo-

sphere and removed in the lower atmosphere. Daley-Yates et al. (2021) aimed to determine the equilibrium temperature profile while accounting for a compositional gradient and radiative forcing for an idealized super-Earth atmosphere. Their simulations suggest that compositional convection leads to a reduction of the temperature gradient, causing the lower atmosphere temperature to decrease while the upper atmosphere temperature increased. We perform a similar simulation in Chapter 3 of this thesis, but generalize our study to focus on compositional convection without forcing the system using a chemical reaction term or additional heating terms.

2.1.2 Hydrogen-Dominated Atmospheres

In a hydrogen-dominated atmosphere, any atmospheric tracer is heavier than the background atmosphere. Therefore, in H_2-dominated atmospheres, vertical gradients of atmospheric tracers can strongly stabilize and potentially inhibit convection (Guillot, 1995; Leconte et al., 2017; Friedson and Gonzales, 2017). Compositional convection in H_2-dominated atmospheres has primarily been studied using 1D models for applications to the Solar System giant planets (Guillot, 1995; Li and Ingersoll, 2015; Leconte et al., 2017; Friedson and Gonzales, 2017) with some recent studies extending this idea to determine the structure of exoplanets with a H_2-dominated atmosphere and a surface magma ocean using 1D models (Markham et al., 2022; Misener and Schlichting, 2022).

For the case when the atmospheric tracer can condense in the temperature-pressure range of the atmosphere and the atmosphere is saturated with the tracer, Guillot (1995) showed that condensation of atmospheric tracers in hydrogen-helium-dominated atmospheres can completely suppress convection when the abundance of the atmospheric tracer reaches a critical value. Leconte et al. (2017) further extended this theory and suggested that in the absence of convection the primary mechanism to transport heat through atmospheric layers where convection is inhibited is radiation. Convectively stable radiative layers lead to

an increase in the deep atmosphere temperature (Leconte et al., 2017). Fig. 2.1 shows the atmospheric thermal profile in the case with and without condensation-driven convective inhibition from Leconte et al. (2017).

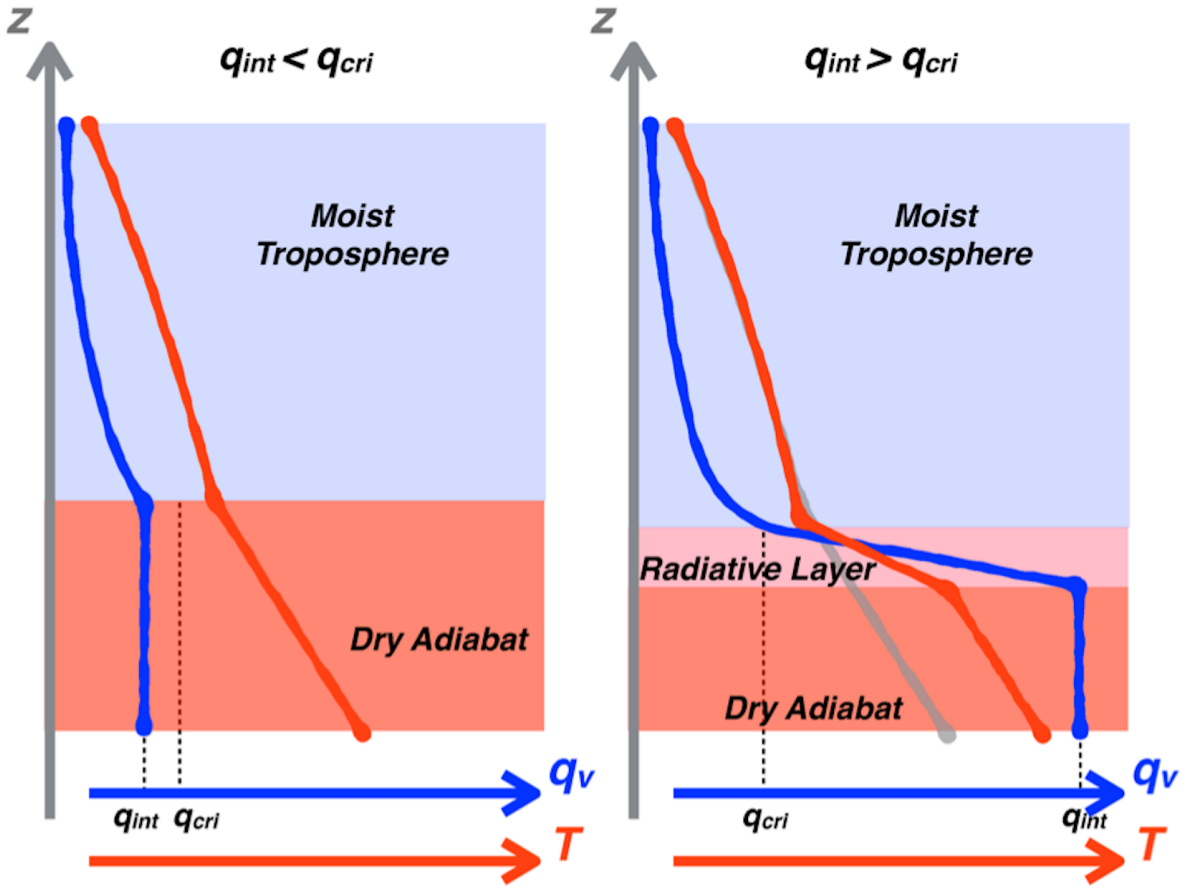

Fig. 2.1 Atmospheric temperature (red) and mass mixing ratio (blue) profile with (right panel) and without (left panel) condensation-driven convective inhibition. The left panel shows two layers within the atmosphere where in the lower layer (red shaded region) condensation does not occur (dry regime) and $q_{\rm int} < q_{\rm crit}$. While the upper atmospheric layer (blue shaded region) shows the atmospheric state described by a moist adiabat. The right panel shows a predicted three layer atmosphere where the condensing (moist troposphere) and dry regions of the atmosphere are separated by a radiative layer where the temperature decreases faster with height relative to a convective layer. The radiative layer is proposed to form when condensation occurs and $q_{\rm int} > q_{\rm crit}$. Adapted from Leconte et al. (2017)

Guillot (1995) suggested based on the observed temperature gradient, there is evidence of stabilized layers which could be due to methane condensation causing convective inhibition in the atmospheres of Uranus and Neptune. Furthermore, Leconte et al. (2017) suggest

that the observed giant storms on Saturn could be explained by compositional convective inhibition due to the presence of water vapor. Additionally, if Jupiter is sufficiently enriched in water vapor, a non-convecting region due to compositional buoyancy would also be present within Jupiter's atmosphere (Leconte et al., 2017), but this has not been observed.

Li and Ingersoll (2015) used a compositional convection mechanism to explain the periodic giant storms observed in Saturn's Northern Hemisphere (i.e. Great Storm of 2010-2011). Li and Ingersoll (2015) suggest that the concentration of water vapor is greater than the critical value in the lower atmosphere of Saturn, causing the atmosphere to be stable and thus inhibiting convection between the upper and lower part of the atmosphere. A key difference between the mechanism proposed by Li and Ingersoll (2015) compared to Leconte et al. (2017) is that Li and Ingersoll (2015) assume that convective inhibition completely stops heat transport between the upper and lower part of the atmosphere and no radiative layer forms. Heat exchange between the two atmospheric layers occurs during the periodic giant storms in the Li and Ingersoll (2015) mechanism. For the giant storms to occur in the Li and Ingersoll (2015) mechanism, the upper atmosphere needs to radiatively cool to the same virtual temperature as the top of the lower atmosphere, at which point a giant storm occurs. There are limitations and uncertainty in the Li and Ingersoll (2015) model, such as the radiative timescale of the storms or why the giant storms seem to be observed only at certain latitudes.

Convective inhibition due to condensing compositional convection is relevant for any planetary atmosphere with a condensable atmospheric tracer that has a higher mean molecular weight than the background atmosphere. In Chapter 4 we use 3D convection resolving simulations to explore the compositional and temperature profiles due to condensing compositional convection. The aim of the simulations performed in Chapter 4 is to determine the atmospheric state when convective inhibition is possible and to determine whether or not stable radiative layers can form. Condensation does not need to occur to create

compositional buoyancy effects. In Chapter 3, we explore non-condensing compositional convection in H_2-dominated and high mean molecular weight atmospheres.

2.2 Stability to Atmospheric Convection

Assessment of the stability of an initial atmospheric state to convection can proceed from a linearized stability analysis or a buoyancy analysis in which the density of a displaced parcel is compared to the density of the surrounding atmosphere. The former kind of analysis yields how initial instability growth rates depend on the horizontal wavelength of a perturbation. Alternatively, buoyancy analysis, which is more common in the context of atmospheric convection studies, has the advantage that it considers the energy available for mixing when air parcels are displaced by a finite amount, and this is the approach used in this thesis.

Neutral stability is achieved when an initial displacement does not grow in amplitude in the absence of dissipation. A displaced parcel in a neutrally stable situation will experience buoyancy that acts to move it back towards its original position, but without dissipation the parcel will oscillate about its original position without decay. It is expected that friction will eventually damp out the oscillations. Marginally stable states are neutrally stable states where a displaced parcel has zero buoyancy, and therefore remains in place rather than oscillating about its original position. Marginally stable states are neither convective nor stably stratified. We can further distinguish local versus global neutral stability. Local stability only demands neutral stability for infinitesimal displacements, whereas global stability demands neutral stability against displacements with a finite (though possibly bounded) amplitude.

Stability can be determined by adiabatically displacing an atmospheric parcel vertically, without allowing any mixing of the parcel with its surroundings, and comparing its density with the ambient atmosphere at its new level. A sketch illustrating atmospheric stability is shown in Fig. 2.2. An adiabat describes the temperature-pressure profile of an air parcel as

it is displaced adiabatically within the atmosphere. In Fig. 2.2 we use virtual temperature rather than density to determine atmospheric stability, where $\rho = P/(R_b T_v)$. Generally, a displaced air parcel is convectively stable when the virtual temperature of the parcel is less than the atmospheric virtual temperature. Conversely, a displaced air parcel is unstable to convection when its virtual temperature is greater than the atmospheric virtual temperature allowing the parcel to continue to rise and convectively mix. In the case where the atmospheric tracer is saturated in an air parcel and condensation can occur as the air parcel is displaced, condensation and the compositional gradient can potentially stabilize an unstable superadiabatic atmospheric temperature profiles. This is further discussed in Section 2.2.3.

First, we will consider atmospheric thermodynamics background and convective stability criterion for a well mixed atmosphere in Section 2.2.1 and an atmosphere with a non-condensing atmospheric tracer in Section 2.2.2. We then consider the case where the atmospheric tracer can condense in Section 2.2.3. We end this chapter with the definition of convective available potential energy (CAPE) in Section 2.2.4 which allows us to determine atmospheric stability when an air parcel is perturbed a finite amount. CAPE is applicable to convection with an atmospheric tracer that is either condensing or non-condensing.

Note, in the following sections we consider mixtures of a background gas, with corresponding quantities labeled with subscript b, and a second gas (an atmospheric tracer) denoted by subscript v, for *vapor*. In all the examples we consider explicitly in this thesis, the second gas is water vapor.

2.2.1 Convection in Well-Mixed Atmospheres & The Schwarzschild Stability Criterion

If an atmosphere is well-mixed, then the composition of the atmosphere is homogeneous everywhere. To determine the stability of the atmosphere to convection, we compare the

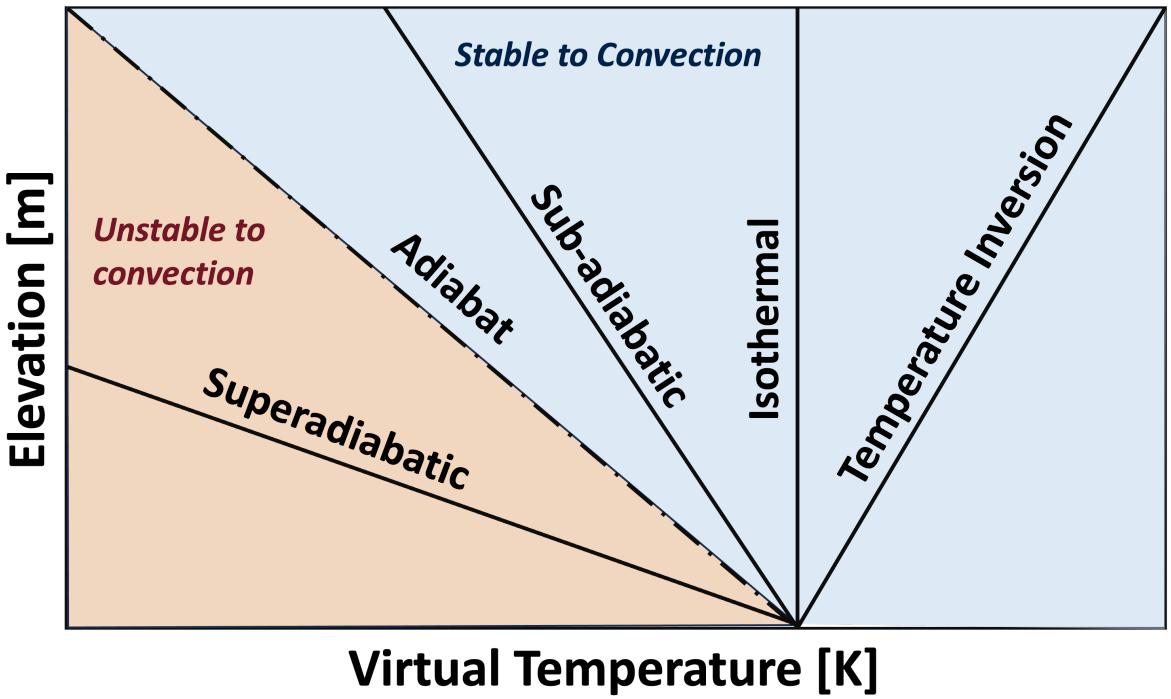

Fig. 2.2 Sketch illustrating atmospheric stability with respect to convection. Consider an air parcel rising from the intersection point of all the virtual temperature profiles. A rising air parcel, when perturbed adiabatically, will follow a temperature profile described by either a dry or moist adiabat, depending on whether the air parcel is sub-saturated or saturated respectively. Stability to convection is determined by comparing the density of a displaced air parcel to the background atmospheric density profile. In this sketch we use virtual temperature to represent density perturbations due to composition and temperature. If the atmospheric virtual temperature profile is in the blue-shaded region, the virtual temperature of the displaced air parcel is less than that of the atmospheric profile, and the parcel will return to its original position, indicating convective stability. If the atmospheric virtual temperature profile is represented by a profile in the orange-shaded region, the virtual temperature of the displaced parcel is greater than the virtual temperature of the background atmosphere, and the parcel is unstable, leading to convection. Note, this sketch illustrates a concept and is not intended to be technically accurate.

density of a displaced parcel to the density of the ambient atmosphere. If the composition is uniform everywhere in the atmosphere, density variations are solely due to temperature variations, and we can determine atmospheric stability by comparing the temperature of a displaced parcel to the temperature of the ambient atmosphere.

From the first law of thermodynamics, the entropy change per unit mass of an air parcel assuming no compositional change is,

$$\delta S = C_p d\ln T - R d\ln p, \tag{2.4}$$

where C_p and R are the heat capacity and gas constant for the atmosphere per unit mass. The specific heats of the individual gases depend on temperature, but the temperature dependence will be neglected throughout the current work. $R \equiv R^*/\mu$ where μ is the total mean molecular weight of the atmosphere and R^* is the universal gas constant. An air parcel when displaced will rise or sink adiabatically, therefore,

$$\frac{d\ln T_{\rm parcel}}{d\ln p} = \beta, \tag{2.5}$$

where $\beta = R/C_p$.

Neutral stability requires that the temperature of a parcel lifted adiabatically is less than the ambient temperature where,

$$T_{\rm parcel}(p_2) = T_1 - \left(\frac{d\ln T_{\rm parcel}}{d\ln p}\right) d\ln p, \tag{2.6}$$

$$T_{\rm amb}(p_2) = T_1 - \left(\frac{d\ln T_{\rm amb}}{d\ln p}\right) d\ln p. \tag{2.7}$$

Using Eqn. 2.5, $T_{\rm parcel} \leq T_{\rm amb}$ is,

$$\frac{d\ln T_{\rm amb}}{d\ln p} \leq \beta. \tag{2.8}$$

This is the Schwarzschild criterion for atmospheric stability in well-mixed atmospheres (Schwarzschild and Härm, 1958).

2.2.2 Non-Condensing Compositional Convection & The Ledoux Local Stability Criterion

Consider an atmosphere with a compositional gradient of an atmospheric tracer (i.e. an atmosphere with inhomogeneous composition) where q_v is the mass mixing ratio of the vapor to the background gas, i.e. ρ_v/ρ_b, where ρ is density. Up to a constant, the entropy per unit mass of the mixture is,

$$S(p) = C_{\text{p,mix}} \ln T - R_b \left(\frac{1}{1+q_v} \right) \ln p_b - R_v \left(\frac{q_v}{1+q_v} \right) \ln p_v, \tag{2.9}$$

where p_b and p_v represent the partial pressure of the background and tracer components respectively (Emanuel, 1994, Chap. 4). $C_{\text{p,mix}}$ is the mass-weighted mean specific heat of the mixture, at constant pressure,

$$C_{p,\text{mix}} = \frac{1}{1+q_v} C_{p,b} + \frac{q_v}{1+q_v} C_{p,v}. \tag{2.10}$$

$R_b \equiv R^*/M_b$ and $R_v \equiv R^*/M_v$ are the gas constants for the two gases, where R^* is the universal gas constant, and M_b and M_v are the molar masses of the respective gases. The total pressure is $p = p_b + p_v$, and serves as a vertical coordinate.

Suppose a parcel with original temperature $T(p_1)$ is displaced adiabatically to a pressure level p_2, without any mixing with the surroundings. Using conservation of entropy, $T(p_2)$ is

determined by

$$0 = C_{\mathrm{p,mix}} \ln \frac{T(p_2)}{T(p_1)} - R_b \left(\frac{1}{1+q_v} \right) \ln \frac{p_{b,2}}{p_{b,1}} - R_v \left(\frac{q_v}{1+q_v} \right) \ln \frac{p_{v,2}}{p_{v,1}}, \tag{2.11}$$

$$= C_{\mathrm{p,mix}} \ln \frac{T(p_2)}{T(p_1)} - R_{\mathrm{mix}} \ln \frac{p_2}{p_1}, \tag{2.12}$$

where

$$R_{\mathrm{mix}} = R_b \left(\frac{1}{1+q_v} \right) + R_v \left(\frac{q_v}{1+q_v} \right). \tag{2.13}$$

Since the parcel is displaced without mixing, q_v is fixed at its original value, hence $C_{p,\mathrm{mix}}$ also remains fixed at its original value. Because q_v (and likewise molar mixing ratio) remains fixed, Dalton's Law implies $p_{b,2}/p_{b,1} = p_2/p_1$ and $p_{v,2}/p_{v,1} = p_2/p_1$, from which the second equality in Eqn. 2.11 is derived. If we define $\beta_{\mathrm{mix}} = R_{\mathrm{mix}}/C_{p,\mathrm{mix}}$ then,

$$T(p_2) = T(p_1) \left(\frac{p_2}{p_1} \right)^{\beta_{\mathrm{mix}}(p_1)}. \tag{2.14}$$

Eqn. 2.14 defines the dry adiabat originating from p_1. Note that the logarithmic slope in Eqn. 2.14 is given by the value of β_{mix} at the original pressure level p_1.

To determine stability, we compare the density of the displaced parcel with the density of the ambient atmosphere at p_2. The density of displaced and ambient parcels is determined from their temperature using the ideal gas equation of state with gas constants appropriate to their respective composition. When composition is inhomogeneous, it is customary to compute density using the virtual temperature, T_v,

$$T_v = T \frac{M_b}{\mu(p)}, \tag{2.15}$$

where μ is the mass-weighted harmonic mean molar mass of the gas mixture and M_b is the molar mass of the background gas. The mean molar mass can be written as,

$$\frac{M_b}{\mu(p)} = \left(\frac{1 + q_v(p)/\epsilon}{1 + q_v(p)}\right), \tag{2.16}$$

where $\epsilon = M_v/M_b$, and M_v is the molar mass of the tracer. When $\epsilon < 1$ the tracer enhances buoyancy, whereas for $\epsilon > 1$ (e.g. for H_2O tracer in an H_2 atmosphere) the tracer suppresses buoyancy.

For a parcel displaced adiabatically without mixing, the original value $q_v(p_1)$ is conserved, so this value is used in computing the virtual temperature of the displaced parcel. Likewise, the original $\beta_{\text{mix}}(p_1)$ is used in computing the temperature of the displaced parcel. The resulting virtual temperature of the adiabatically displaced parcel defines the virtual adiabat which passes through $(p_1, T_v(p_1))$, for which we will use the notation $T_{v,\text{ad}}(p_2|p_1)$. Thus,

$$T_{v,\text{ad}}(p_2|p_1) = T_v(p_1)\left(\frac{p_2}{p_1}\right)^{\beta_{\text{mix}}(p_1)}. \tag{2.17}$$

The actual temperature of the displaced parcel, $T_{\text{ad}}(p_2|p_1)$ can be obtained from Eqn. 2.17 using Eqn. 2.15 and Eqn. 2.16 with mixing ratio $q_v(p_1)$ corresponding to that of the parcel at its origin.

A lifted parcel ($p_2 < p_1$) has negative buoyancy, and hence is neutrally stable, when its virtual temperature $T_{v,\text{ad}}(p_2|p_1)$ is less than the ambient virtual temperature $T_{v,\text{amb}}(p_2)$. The lifted parcel's virtual temperature $T_v(p_2)$ is computed from Eqn. 2.17 using the original mixing ratio $q_v(p_1)$, since q_v is conserved upon lifting, but the ambient virtual temperature is computed using the local value $q_v(p_2)$, which is generally different from $q_v(p_1)$. For a lifted parcel, neutral stability requires $T_{v,\text{ad}}(p_2|p_1) \leq T_{v,\text{amb}}(p_2)$, or equivalently,

$$T_{v,\text{amb}}(p_1)\left(\frac{p_2}{p_1}\right)^{\beta_{\text{mix}}(p_1)} \leq T_{v,\text{amb}}(p_2), \tag{2.18}$$

with the equality defining marginal stability (i.e. neutral buoyancy), in which case the displaced parcel neither rises nor sinks.

The Ledoux Local Stability Criterion

For stability against infinitesimal displacements, consider $p_2/p_1 = 1-\delta$, with $0 < \delta << 1$ for infinitesimal lifting. Substitute $p_2/p_1 = 1-\delta$ in Eqn. 2.18, Taylor expand, and pass to the limit $\delta \to 0$ to obtain,

$$\left.\frac{d\ln T_{v,\mathrm{amb}}}{d\ln p}\right|_{p_1} \leq \beta_{\mathrm{mix}}(p_1). \tag{2.19}$$

The criterion for neutral stability of a slightly depressed parcel ($\delta < 0$) is identical. Eqn. 2.19 is a form of the Ledoux criterion for local stability (Ledoux, 1947) at p_1. The Ledoux criterion has the same form as the Schwarzschild criterion (Schwarzschild and Härm, 1958), which applies to the compositionally homogeneous case, except with virtual temperature substituted for temperature.

Suppose that the ambient virtual temperature profile is marginally stable (Eqn. 2.19 with inequality replaced by equality) for all p_1 within a layer. Then, integrating Eqn. 2.19 over the layer, we find,

$$T_{v,\mathrm{amb}}(p) = T_{v,\mathrm{amb}}(p_0)\, e^{\int_{\ln p_0}^{\ln p} \beta_{\mathrm{mix}}(p)\, d\ln p}, \tag{2.20}$$

where $T_{v,\mathrm{amb}}(p_0)$ is the virtual temperature at some point p_0 within the layer. Eqn. 2.20 defines a unique local, marginally stable virtual temperature profile that passes through $(p_0, T_{v,\mathrm{amb}}(p_0))$. However, there is a continuous family of temperature and composition profiles that correspond to the same marginally stable virtual temperature profile, $T_{v,\mathrm{amb}}(p)$, given by varying the end state $q_v(p)$ in Eqn. 2.15. This differs from the the compositionally homogeneous case where there is a unique marginally stable end state passing through a given temperature-pressure point.

The profile defined by Eqn. 2.20 is not the virtual adiabat that passes through $(p_0, T(p_0))$, since the virtual adiabat would be determined from Eqn. 2.17 with fixed $\beta_{\mathrm{mix}}(p_0)$. If $\beta_{\mathrm{mix}}(p)$

is independent of p, the Ledoux-stable profile reduces to the virtual adiabat. This is the case when the composition is homogeneous in the layer, $q_v(p)$ = constant, or for inhomogeneous compositions it can be approximately true if the two gases in the mixture have nearly the same numbers of excited internal degrees of freedom.

Stability to Finite Amplitude Displacements

For compositionally homogeneous atmospheres, if the ambient temperature profile within a given layer is taken to be the dry adiabat passing through any (p_1, T_1) point, then adiabatic displacements of parcels by any amount within the layer yields zero buoyancy, so that the layer is marginally stable to finite amplitude displacements. This is not generally the case for virtual adiabats in a compositionally inhomogeneous atmosphere. Suppose that within a layer, $T_{v,\mathrm{amb}}(p) = T_{v,\mathrm{ad}}(p|p_1)$ for some p_1. If we adiabatically lift a parcel from some pressure $p_0 \neq p_1$ within the layer, without allowing mixing, the buoyancy of the lifted parcel is then proportional to,

$$T_{v,\mathrm{ad}}(p|p_0) - T_{v,\mathrm{ad}}(p|p_1) = T_{v,\mathrm{ad}}(p_0|p_1)\left(\left(\frac{p}{p_0}\right)^{\beta_{\mathrm{mix}}(p_0)} - \left(\frac{p}{p_0}\right)^{\beta_{\mathrm{mix}}(p_1)}\right). \tag{2.21}$$

Since $\beta_{\mathrm{mix}}(p_0) \neq \beta_{\mathrm{mix}}(p_1)$ when $q_v(p)$ is non-uniform, the buoyancy of the displaced parcel is generally nonzero, and could be either neutrally stable or unstable depending on the profile of β_{mix}. Fig. 2.3(a) illustrates this effect for the case of water vapor mixed with an H_2 background, with concentration profile $q_v(p) = 10(p/p_0)$, where p_0 is the surface pressure. The ambient virtual temperature is taken to be $T_{v,\mathrm{ad}}(p, \frac{1}{2}p_0)$, with $T_{v,\mathrm{ad}} = 300$ K at $p = \frac{1}{2}p_0$. The figure shows the buoyancy for a parcel lifted adiabatically without mixing from p_0 to p. We see that (by construction) a parcel displaced by any amount from $p = \frac{1}{2}p_0$ would have zero buoyancy, but a parcel lifted from p_0 is positively buoyant and unstable to convection. Since the vertical variation of β_{mix} is small, the buoyancy generated is small, equivalent to under a 3.5 K excess in virtual temperature.

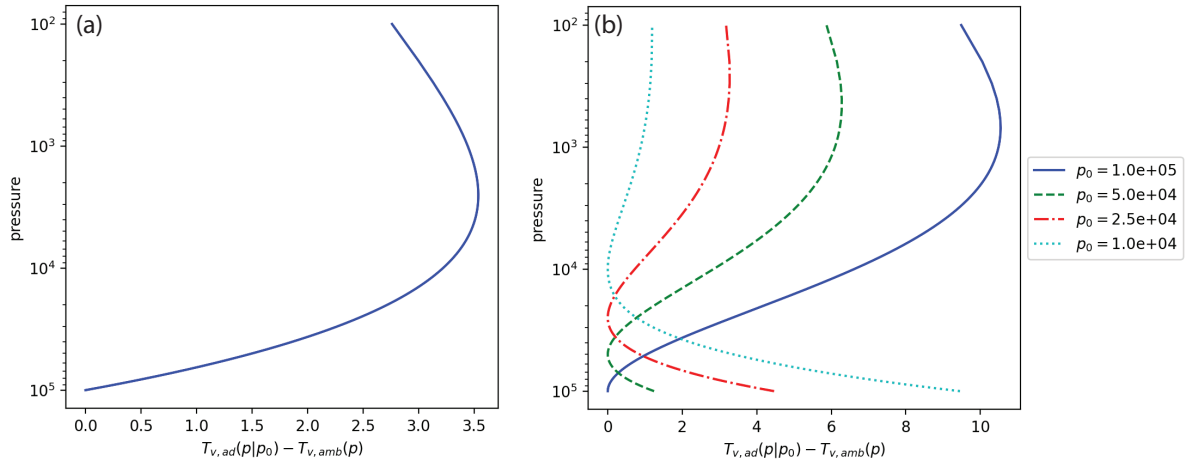

Fig. 2.3 Buoyancy for finite adiabatic displacements from pressure p_0 in an ambient profile. The atmosphere is a mixture of H_2 with water vapour, with water vapor profile $q_v(p) = 10(p/p_0)$, where p_0 is the surface pressure. (a) The ambient profile is the virtual adiabat passing through $p = 5 \cdot 10^4$ Pa and T = 300 K, and the parcel is lifted from $p_0 = 10^5$ Pa. (b) The ambient profile is the Ledoux-stable profile $T_{v,\mathrm{ad}}(p, \frac{1}{2}p_0)$, with $T_{v,\mathrm{ad}} = 300$ K at $p = \frac{1}{2}p_0$, and the parcel is lifted from the various p_0 given in the legend.

To illustrate that a layer deemed locally marginally stable by the Ledoux criterion is not necessarily stable to finite amplitude displacements in Fig. 2.3(b), we compute the buoyancy of displacements from various p_0 of a Ledoux-stable profile computed from Eqn. 2.20 with the same composition and $q_v(p)$ as in the preceding example. As expected, the buoyancy vanishes at each p_0, but increases only quadratically with displacement; the latter confirms marginal stability to small displacements. However, for large displacements in the upward or downward directions, buoyancy for this profile is positive: a parcel lifted by a finite amount will continue to rise. A parcel displaced downward by a finite amount will have positive buoyancy and ascend back towards the original position, but thereafter probably overshoot into a positive displacement and continue to rise, thus triggering instability. The instability to finite amplitude displacements arises from $\beta_{\mathrm{mix}}(p)$. If the layer were well-mixed, resulting in a constant β_{mix} throughout the layer, it would guarantee global marginal stability within the layer.

Virtual Potential Temperature

We can define a virtual potential temperature θ_v corresponding to adiabatic unmixed displacements from pressure level p to some reference pressure level p_{00}:

$$\theta_v \equiv T_v(p)\left(\frac{p}{p_{00}}\right)^{-\beta_{\text{mix}}(p)}. \tag{2.22}$$

Note that in Eqn. 2.22 the exponent β_{mix} is evaluated at the parcel's origin p, because an unmixed parcel retains the q_v, and hence β_{mix} of its origin. For a compositionally homogeneous atmosphere, which has uniform β_{mix}, the choice of reference pressure p_{00} changes the profile of $\theta_v(p)$ by a multiplication constant and does not change the shape of the profile. Uniform θ_v within a layer indicates global marginal stability to displacements between any pair of points within the layer. However, when β_{mix} depends on p, a profile of θ_v that is uniform for one choice of p_{00} will not generally be uniform for a different choice of p_{00}. This is another way of phrasing the result illustrated in Fig. 2.3. Defining a virtual adiabat based on displacement from one position does not guarantee zero buoyancy when a parcel is displaced from a different position.

We have shown in Fig. 2.3 that the effects of variation of β_{mix} on buoyancy are small. In practice, few inaccuracies are produced by using an approximate virtual temperature based on fixed $\overline{\beta}_{\text{mix}}$;

$$\theta_v = T_v(p)\left(\frac{p}{p_{00}}\right)^{-\overline{\beta}_{\text{mix}}}, \tag{2.23}$$

where $\overline{\beta}_{\text{mix}}$ is chosen to be typical of the value of β_{mix} within the layer. Constant approximate virtual potential temperature within a layer guarantees approximate marginal stability for finite amplitude adiabatic unmixed displacements between any two points within the layer.

We can also define a virtual potential temperature-like quantity based on the Ledoux-stable profile in Eqn. 2.20,

$$\tilde{\theta}_v = T_v(p)e^{-\int_{\ln p_{00}}^{\ln p}\beta_{\text{mix}}(p)d\ln p}. \tag{2.24}$$

If $\tilde{\theta}_v$ is constant within a layer, then the layer is marginally stable to infinitesimal displacements starting from any point within the layer. This is the virtual potential temperature referred to in Leconte et al. (2017). However, Eqn. 2.24 is not a true potential temperature in the usual sense, because it does not correspond to the correct temperature change upon adiabatic unmixed displacements. Uniformity of $\tilde{\theta}_v$ does not guarantee global marginal stability. In practice, the distinction between Eqn. 2.24 and a true virtual potential temperature is mostly irrelevant, because Eqn. 2.24 reduces to Eqn. 2.23 when β_{mix} is constant, or the variations in β_{mix} are generally too small to yield important effects.

For a compositionally inhomogeneous atmosphere, if the final mixed state has remaining compositional inhomogeneities, the most general marginal stability condition that can be demanded is that the end state profiles satisfy the Ledoux local marginal stability condition everywhere. The effect of the variation of β_{mix} on buoyancy is small, even when there are considerable variations in q_v. Therefore, the virtual adiabats are nearly the same regardless of which level a parcel is displaced from. Similarly, the marginally Ledoux stable profile is nearly marginally stable to finite amplitude displacements. We have found that taking into account variations in β_{mix} yields only small changes in the stabilized virtual temperature profile as compared to fixing β_{mix} at some value representative of its typical value within the mixed region. Thus, we define an approximate virtual adiabat with fixed β_{mix}, even if the mixed state has some remaining compositional variations as,

$$T_{v,\text{ad}}(p) = T_v(p_{00}) \left(\frac{p}{p_{00}} \right)^{\overline{\beta}_{\text{mix}}}. \tag{2.25}$$

Similarly, we can define an approximate virtual potential temperature whose constancy within the mixed region defines global marginal stability. In the subsequent discussion, we will drop the term “approximate" and simply refer to “virtual adiabat" given by Eqn. 2.25 and “virtual potential temperature" given by Eqn. 2.23. Note that the fixed β_{mix} approximation does not eliminate the degeneracy in the family of final marginally stable temperature and

composition profiles. The marginally stable virtual temperature profile is uniquely determined by a virtual adiabat, but the effect of q_v on temperature for fixed virtual temperature is still large.

2.2.3 Condensing Compositional Convection & The Guillot Local Stability Criterion

If the atmospheric tracer can condense in the temperature-pressure range of the atmosphere, then a key difference to the non-condensing atmosphere, is that the mass mixing ratio profile is constrained by the temperature through the saturation vapor pressure. Assuming that the density of condensates is much greater than the gas density, the Clausius-Clapeyron equation allows us to determine the saturation vapor pressure as,

$$\frac{d\ln e_{\rm sat}}{d\ln T} = \frac{L_v}{R_v T}, \tag{2.26}$$

where $e_{\rm sat}$ is the saturation vapor pressure of the condensable tracer at a given temperature T, L_v is the latent heat of vaporization, and R_v is the gas constant of the condensable tracer. For a given temperature, we can determine the mass mixing ratio at which the tracer is saturated,

$$q_{v,\rm sat} = \epsilon\left(\frac{e_{\rm sat}}{p - e_{\rm sat}}\right), \tag{2.27}$$

where p is the total atmospheric pressure. To determine if the tracer is saturated at a given (p, T), we compare the partial pressure of the tracer to its saturation vapor pressure,

$$RH = \frac{p_v}{e_{\rm sat}} = \left(\frac{q_v}{\epsilon + q_v}\right)\left(\frac{p}{e_{\rm sat}}\right) \tag{2.28}$$

where p_v is the partial pressure of the tracer at (p, T) and RH is the relative humidity. For a saturated air parcel, the entropy per unit total mass is,

$$\delta S = C_{p,\mathrm{mix}} \ln T - R_{\mathrm{mix}} d \ln p + \left(\frac{1}{1+q_v} \frac{L_v}{T} \right) d q_{v,\mathrm{sat}}. \tag{2.29}$$

$q_{v,\mathrm{sat}}$ can be evaluated using Eqn. 2.26 - 2.27 and

$$d q_{v,\mathrm{sat}} = \left. \frac{d q_{v,\mathrm{sat}}}{dT} \right|_p + \left. \frac{d q_{v,\mathrm{sat}}}{dp} \right|_T. \tag{2.30}$$

Assuming the saturated air parcel is displaced approximately adiabatically without any mixing with its surroundings,

$$\frac{d \ln T^*_{ad}}{d \ln P} = \beta_{\mathrm{mix}} \left[\frac{1 + q_{v,\mathrm{sat}} \left(\frac{L_v}{R_b T} \right)}{1 + q_{v,\mathrm{sat}} \left(\frac{L_v}{C_{p,\mathrm{mix}} T} \right) \left(\frac{L}{R_v T} \right) \left(\frac{1+q_{v,\mathrm{sat}}/\epsilon}{1+q_{v,\mathrm{sat}}} \right)} \right]. \tag{2.31}$$

Eqn. 2.31 is the moist adiabat and gives the temperature-pressure profile of a saturated air parcel as it is displaced *pseudoadiabatically*. The moist adiabat is a pseudoadiabatic processes because if the condensate is removed from the system, then the process is not truly reversible. Similar to Guillot (1995); Leconte et al. (2017), we will assume the volume of the condensed phase is negligible compared to the vapor phase of the atmospheric tracer. Additionally, we assume that all condensed phases are instantaneously removed and do not consider the compositional gradient of condensed phases in determining atmospheric stability.

To determine the stability of a saturated atmosphere to convection while accounting for compositional gradients, we need to determine how condensation affects the mean molecular weight gradient of a displaced parcel and the ambient atmosphere. As a saturated air parcel is displaced, condensation leads to a change in the composition of the parcel. Additionally, the (saturated) background atmosphere has a compositional gradient since the

mass mixing ratio varies as a function of altitude due to the saturation vapor pressure curve. The compositional gradient is,

$$\frac{d\ln\mu}{d\ln p} = \frac{d\ln\mu}{d\ln q_{v,\mathrm{sat}}}\frac{d\ln q_{v,\mathrm{sat}}}{d\ln p} \tag{2.32}$$

where again, μ is the total mean molecular weight gradient in the atmosphere given by Eqn. 2.16. The first term on the right-hand side of the equation, $\frac{d\ln\mu}{d\ln q_v}$ can be evaluated directly using Eqn. 2.16. The second term, represents how the mass mixing ratio varies with altitude and is given by,

$$\frac{d\ln q_{v,\mathrm{sat}}}{d\ln p} = \left.\frac{d\ln q_{v,\mathrm{sat}}}{d\ln T}\right|_p \frac{d\ln T}{d\ln p} + \left.\frac{d\ln q_{v,\mathrm{sat}}}{d\ln p}\right|_T, \tag{2.33}$$

where $\frac{d\ln T}{d\ln P}$ is the temperature gradient of either the parcel or the ambient atmosphere. $q_{v,\mathrm{sat}}$ varies as a function of temperature via the Clausius-Clapeyron relation and $\left.\frac{d\ln q_{v,\mathrm{sat}}}{d\ln T}\right|_p$ can be determined using Eqn. 2.26. The final term, $\left.\frac{d\ln q_{v,\mathrm{sat}}}{d\ln p}\right|_T$ is given by differentiating Eqn. 2.27. After evaluating individual terms and simplifying the result, the mean molecular weight gradient is (Guillot, 1995; Leconte et al., 2017),

$$\frac{d\ln\mu}{d\ln p} = q_{v,\mathrm{sat}}\left(\frac{1-1/\epsilon}{1+q_{v,\mathrm{sat}}}\right)\left[\left(\frac{L_v}{R_v T}\right)\left(\frac{d\ln T}{d\ln p}\right) - 1\right]. \tag{2.34}$$

The Guillot Local Stability Criterion

Stability to convection is determined by comparing the density of a displaced saturated air parcel to the density of the ambient saturated atmosphere. Again, we can use virtual temperature to represent the composition effects where a parcel is stable to convection when $T_{v,\mathrm{parcel}} < T_{v,\mathrm{amb}}$. To compare the virtual temperature directly, we would need to solve Eqn. 2.34 and Eqn. 2.31 and account for the change in the composition of the displaced air parcel due to condensation. Alternatively, we consider stability against infinitesimal

displacements and compare the gradient of virtual temperature of a saturated parcel to that of the ambient saturated atmosphere where $\frac{d\ln T_v}{d\ln p} = \frac{d\ln T}{d\ln p} - \frac{d\ln \mu}{d\ln p}$. A saturated parcel is stable against infinitesimal displacements when,

$$\left(\frac{d\ln T}{d\ln p} - \frac{d\ln \mu}{d\ln p}\right)\Big|_{\text{amb}} - \left(\frac{d\ln T}{d\ln p} - \frac{d\ln \mu}{d\ln p}\right)\Big|_{\text{parcel}} \leq 0 \tag{2.35}$$

where $\frac{d\ln \mu}{d\ln p}$ is given by Eqn. 2.34 and $\left(\frac{d\ln T}{d\ln p}\right)\Big|_{\text{parcel}}$ is given by Eqn. 2.31. Simplifying this expression using Eqn. 2.34 yields,

$$\left(\frac{d\ln T_{\text{amb}}}{d\ln p} - \frac{d\ln T^*_{\text{ad}}}{d\ln p}\right)\left(1 - \left(\frac{q_{v,\text{sat}}}{1+q_{v,\text{sat}}}\right)(1-1/\epsilon)\left(\frac{L_v}{R_v T}\right)\right) \leq 0, \tag{2.36}$$

where $\frac{d\ln T^*_{\text{ad}}}{d\ln p}$ is the temperature gradient of the saturated parcel given by the moist adiabat. Eqn. 2.36 is the Guillot criterion for local stability (Guillot, 1995).

When the atmospheric tracer is lighter than the background atmosphere so that $\epsilon < 1$, the mean molecular weight term, $(1-1/\epsilon)$ will always be negative meaning that the compositional term in Eqn. 2.36 is always positive. Conversely, when $\epsilon > 1$, a compositional gradient can stabilize an unstable atmospheric temperature. Consider $\frac{d\ln T_{\text{amb}}}{d\ln p} > \frac{d\ln T^*_{\text{ad}}}{d\ln p}$, in the absence of a compositional gradient the ambient temperature profile is unstable and convection will occur. However, when accounting for the compositional effects, the compositional gradient can stabilize an unstable atmosphere to infinitesimal displacements and inhibit convection when $q_{v,\text{sat}} \geq q_{\text{crit}}$ where

$$q_{\text{crit}} = \frac{R_v T}{L_v(1-1/\epsilon) - R_v T} \tag{2.37}$$

(Guillot, 1995). Compositional gradients of condensable tracers in H_2-dominated atmospheres can provide a strong stabilizing mean molecular weight gradient that can inhibit convection in these planetary atmospheres where $q_v > q_{\text{crit}}$. In Chapter 4, we use 3D

convection-permitting simulations to explore the atmospheric structure when accounting for compositional stabilization in H_2-dominated atmospheres. Leconte et al. (2017) suggested that when convection is inhibited, a radiative layer would form between the upper and lower atmosphere, see Fig. 2.1, where the temperature profile is superadiabatic. We use 3D simulations to determine if this result is realized and explore condensation as a mechanism to transport heat between stable atmospheric layers.

In general, the Guillot criterion is a local stability criterion and does not guarantee neutral stability when a parcel is displaced a finite amount. As in the non-condensing case, stability to finite amplitude displacements is determined using a CAPE analysis.

2.2.4 CAPE Analysis

We use convective available potential energy (CAPE) to assess the stability of an atmosphere to finite amplitude displacements and to determine the amount of energy available for mixing. CAPE represents the work per unit mass the buoyancy force exerts to lift an air parcel containing a mixture of an atmospheric tracer and background air (Emanuel, 1994, Chap. 6). CAPE is defined as,

$$\mathrm{CAPE} = \int_{\mathrm{LNB}}^{p_{\mathrm{init}}} R_b \left[T_{v,\mathrm{parcel}}(p) - T_{v,\mathrm{amb}}(p) \right] d\ln p, \tag{2.38}$$

where p_{init} is the initial parcel location, LNB is the level of neutral buoyancy, $T_{\mathrm{v,parcel}}(p)$ is the virtual temperature profile of a rising air parcel containing an atmospheric tracer, and $T_{\mathrm{v,amb}}(p)$ is the virtual temperature profile of the ambient atmosphere. Eqn. 2.38 assumes there are no retained condensates. The LNB is the pressure at which a rising air parcel has zero buoyancy and the $T_{\mathrm{v,parcel}}$ is equal to $T_{\mathrm{v,amb}}$. When a rising air parcel has positive CAPE it will freely rise within the atmosphere beyond the LNB to the Level of Maximum Ascent (LMA) which is where the kinetic energy of the rising air parcel becomes zero. After the

rising air parcel reaches the LMA, the parcel would oscillate around the LNB until, under the action of friction, it settles at some point near the LNB (i.e. neutral stability).

Analyzing the CAPE of air parcels lifted by finite amounts from various heights within the atmospheric allows one to determine the global stability of the atmosphere. Regions of positive CAPE are convectively unstable and will mix if perturbed. Regions of negative CAPE are stably stratified. If an air parcel with negative CAPE is perturbed upwards, it will sink within the atmosphere to its initial location unless it has enough external energy to rise above the region of negative CAPE. Regions of negative CAPE usually imply that convection will be inhibited unless there is an external energy source (Emanuel, 1994, Chap. 6). Finally, when CAPE = 0, the system is marginally stable.

3

Modeling Non-Condensing Compositional Convection for Applications to Super-Earth and Sub-Neptune Exoplanet Atmospheres

This chapter is a modified version of Habib and Pierrehumbert 2023.

3.1 Summary

The main objective of the work presented in this chapter is to determine stable end-states after convective mixing in an initially inhomogeneous composition atmosphere. We explore non-condensing compositional convection in both high mean molecular weight and H_2-

dominated atmospheres, in an idealized setting. Our simulations are restricted to explore compositional effects on convection where there is no condensation of tracers nor radiation to study compositional convection in its simplest form.

Specifically, we perform 3D nonlinear, initial value problem simulations of initially unstable atmospheric profiles involving mixtures of water vapor with Earth air, CO_2, and H_2 atmospheres using the 3D non-hydrostatic, convection resolving model, Cloud Model 1 (CM1, Bryan, 2009). We explore both compositional suppression of buoyancy, for applications to H_2 atmospheres, and compositional enhancement of buoyancy, for applications to higher mean molecular weight atmospheres.

In an unforced initial value problem, an initial perturbation to the state of rest triggers the conversion of potential energy into kinetic energy, mixing the system and eventually, viciously dissipating as heat. Mixing results in a new state of rest, which must be stable to at least infinitesimal perturbations. It is commonly assumed that a displaced parcel in the end state is marginally stable, meaning it has zero buoyancy relative to the surroundings, so that it neither rises nor sinks. In essence, convection is assumed to do the minimum amount of mixing needed to prevent further growth of any perturbations to the end state.

Our study aims to determine how convective mixing in an initial, unstable inhomogeneous composition atmosphere affects the final atmospheric temperature and compositional profiles. For a compositionally homogeneous atmosphere, convection mixes the final atmospheric state to a dry adiabat which is uniquely defined once the boundaries of the mixed layer are determined. The final atmospheric state after convective mixing in a compositionally homogeneous situation is a global, marginally stable state.

However, for a compositionally inhomogeneous atmosphere, there is a continuous family of marginally stable states that the system could mix to that satisfy the Ledoux local stability criterion (see Section 2.2.2). One of the main goals of our work is to shed light on the which of the possible final temperature and compositional profiles is left behind after convective

mixing. We use 3D convection resolving simulations to address the following questions within this work:

1. What is the final compositional profile after mixing in an initially inhomogeneous composition atmosphere?

2. Does convection mix the final atmospheric state in an initially inhomogeneous composition atmosphere to a local or global marginally stable state?

3. If convection mixes the atmosphere to a locally stable state, can it be described by the virtual adiabat?

4. How do large-scale versus small-scale initial perturbations affect the final state of convective mixing?

Knowing how convection mixes the compositional profile is important to discern which among the many possible final state profiles is realized.

Further, we use our initial value problem simulations to inform the development of a convective adjustment scheme that can better represent non-condensing compositional convection in GCM modeling of super-Earth and sub-Neptune atmospheres. Any convective adjustment scheme must (1) determine if the atmosphere adjusts to a marginally stable state, (2) identify the temperature and compositional profiles that represent this marginally stable state. For a homogeneous composition atmosphere, convection is assumed to mix to a marginally stable state that follows an adiabat and uniquely defines the end state. However, when the initial state has a compositional gradient, assuming convection mixes to a final marginally stable state no longer uniquely defines the end state. A non-condensing convection parameterization is a necessary first step, as any convection scheme must be able to handle the non-condensing case accurately.

In a realistic atmospheric situation, convective instability would be continually created by radiative heating and cooling or by heat flux from the planetary interior. The rate of

generation of instability is balanced against the rate of relaxation towards a marginally stable profile by buoyancy-driven fluid mixing, leading to a statistical-equilibrium turbulent state. The statistical equilibrium problem is more challenging to analyze, but initial value problems provide essential information about the pace of adjustment and the layer affected by mixing. If the turbulent mixing is rapid compared to the rate of regeneration of instability, then the initial value problem provides direct information about the equilibrium state. This is the underlying assumption of convective adjustment parameterizations.

In this chapter, we focus on situations in which water vapor does not condense, in order to explore 3D compositional convection in its simplest form. Our simulation results apply to exoplanets which have atmospheres that are too hot for water to condense within the convecting atmospheric layer. Examples of such exoplanets include; sub-Neptune GJ 1214 b, if we assume a H_2-dominated atmosphere, sub-Neptune K2 18 b where H_2O condensation is limited to a thin layer of the upper atmosphere, and super-Earth 55 Cnc e, if we assume a CO or N_2 based atmosphere.

3.2 Compositional Convection Modeling with CM1

Cloud Model 1 (CM1; Bryan 2009) is a numerical model in 3D Cartesian coordinates that is designed to study microscale (1 – 1000 m) and mesoscale (1 – 1000 km) convective phenomena in idealized simulations. The full equations used within CM1 are described in (Bannon, 2002; Bryan, 2009; Bryan and Morrison, 2012), and a summary of CM1 is provided in the Appendix.

CM1 is originally developed for Earth convection studies. To accommodate modeling exoplanet atmospheres, we made two modifications to the CM1 code. First, we modified CM1 to allow the user to change the composition of both the bulk atmosphere and the atmospheric tracers. Numerically, the atmospheric composition defines the thermodynamic constants such as the ideal gas constant (R), specific heat capacity at constant pressure (C_p)

and constant volume (C_v), as well as, any latent heating terms for the atmospheric tracer which are used in the equations of motion. To allow the user to specify thermodynamic gas constants, we modified CM1 to read a user generated input file which lists the planetary atmospheric parameters that are dependent upon composition for both the background atmosphere and atmospheric tracer. Within this work, we consider Earth-air, H_2, and CO_2 atmospheres with a H_2O vapor non-condensing atmospheric tracer. The gas specific parameters that are used within this study for the three atmospheric compositions are listed in Table 3.1. All simulations use a gravity value of 9.8 m s^{-2} and neglect the Coriolis force.

Table 3.1 Atmospheric constants used within the CM1 non-condensing simulations. All simulations use a gravity value of 9.8 m s^{-2}.

	C_p J(kg K)$^{-1}$	C_v J(kg K)$^{-1}$	R J(kg K)$^{-1}$	$\varepsilon = M_v/M_b$
Earth-air	1005.7	718.6	287.0	0.621
Hydrogen (H_2)	14304.0	10160.0	4124.2	8.94
Carbon Dioxide (CO_2)	844.0	655.0	188.9	0.409
Water Vapor (Atmospheric tracer)	1870.0	1408.5	461.5	N/A

The second modification made to the CM1 code was to accommodate a non-dilute mass mixing ratio. In CM1, the buoyancy equation assumes a dilute mass mixing ratio (see Bryan, 2009). To accommodate non-dilute values, we modified the CM1 code to use a more general form of the buoyancy given by, $B = -g(\rho'/\rho_o)$, where B is the buoyancy, ρ'_b is the deviation of the density from a reference hydrostatic state given by ρ_o, and g is the planetary gravity (Emanuel, 1994, Chap. 1).

We performed simplified initial value problem simulations with CM1 version 20.3. All of our CM1 test cases in this chapter are performed without any condensation, latent heat release, cloud microphysics, or radiation. We can better understand the underlying fluid dynamics of compositional effects on convection by first exploring compositional convection in its simplest form. For simplicity, the planetary radius and gravity used within the CM1 simulations are the given Earth values. While these parameters are based on Earth,

they do not impact the final results of our simulations. The domain of our convection box is small enough that spherical geometry does not have a significant effect. The surface pressure is set to 10^5 Pa within all of the CM1 test cases, and there are no initial winds. To explore the effect of compositional convection, we test the behavior of a non-condensing water vapor atmospheric tracer in three different planetary atmospheres of Earth-air, H_2, and CO_2 composition with two different initial sounding states described by:

1. An isothermal atmosphere at $T = T_s$ with a step mass mixing ratio profile of a non-condensing H_2O tracer given by,

$$q_v(p) = \begin{cases} q_{v,s} & \text{when } p_s > p > p_1 \\ \left(\frac{p-p_2}{p_1-p_2}\right) q_{v,s} & \text{when } p_1 > p > p_2 \\ 0.0 & \text{when } p_2 > p > p_{\text{TOA}}. \end{cases}$$

2. An initial atmospheric sounding state with both a temperature and mass mixing ratio step profile given by,

$$q_v(p) = \begin{cases} q_{v,s} & \text{when } p_s > p > p_1 \\ \left(\frac{p-p_2}{p_1-p_2}\right) q_{v,s} & \text{when } p_1 > p > p_2 \\ 0.0 & \text{when } p_2 > p > p_{\text{TOA}} \end{cases}$$

$$T(p) = \begin{cases} T_s & \text{when } p_s > p > p_1 \\ \left(\frac{T_1-T_s}{p_2-p_1}\right)(p-p_1) + T_s & \text{when } p_1 > p > p_2 \\ T_1 & \text{when } p_2 > p > p_{\text{TOA}}. \end{cases}$$

p_1 and p_2 are arbitrarily chosen pressure levels taken in the lower part of the atmosphere with $p_2 < p_1$. The discontinuity locations p_1 and p_2 are specified in the CM1 code to occur

at $p(\mathrm{nz}/4)$ and $p(\mathrm{nz}/3)$ respectively, where nz is the number of uniformly spaced vertical grid points. In both initial sounding profiles, a high density atmospheric layer is lying above a lower density atmospheric layer, this is unstable and will ultimately lead to turbulent mixing that eliminates the instability. A high density layer over a low density layer is a classic fluid dynamics instability known as the Rayleigh-Taylor instability (Bud'ko and Liberman, 1992; Bernstein and Book, 1983; Gauthier and Le Creurer, 2010).

In sounding profile 1, only the compositional gradient is creating a density difference between the upper and lower atmospheric layers. While in sounding profile 2, the temperature and compositional profiles contribute to the density difference between the upper and lower atmosphere. Between p_1 and p_2 the mass mixing ratio and temperature (when applicable) profiles linearly vary with height. A linear gradient is used to smear out the density profile (i.e. prevent a sharp discontinuity in density at the step interface) to make the initial atmospheric state more stable and allow the CM1 code to run to convergence without becoming numerically unstable. For a step interface in a Rayleigh-Taylor unstable system, the growth rate of the instability increases indefinitely as the wavelength of the perturbation decreases. In numerical simulations this leads to unresolved grid-scale motions if not suppressed. By using a smeared out density transition within the CM1 simulations, a shortwave cutoff is introduced (Bud'ko and Liberman, 1992), which prevents unresolved scales from emerging. In all of the simulations performed within this work, the Mach number is small. Therefore, while compressibility affects the temperature, sound wave and shock generation does not occur to any appreciable extent.

We perform two sets of CM1 simulations. First, we run a series of high resolution CM1 simulations, and second, we perform a parameter study in which CM1 is run with a lower resolution compared to the high resolution simulations. Even though we do not resolve the smallest scale plumes in the parameter study, the final atmospheric profiles of the parameter study are consistent with the results from the high resolution simulations. For all of the

CM1 test cases performed, we use a partial slip bottom boundary condition and a free slip top boundary condition for the winds. The bottom boundary is a solid surface with a fixed surface temperature following the original CM1 formulation. We use doubly periodic horizontal boundary conditions, and large eddy simulation mode with the turbulent kinetic energy (TKE) sub-grid turbulence scheme (Deardorff, 1980). We use the TKE scheme to represent turbulent diffusion and allow for mixing within the CM1 simulations on a sub-grid scale. Turbulent mixing will increase the entropy of the system relative to the initial atmospheric state. The turbulence parameterization represents the cascade of composition and potential temperature variability down to scales where molecular diffusion provides the final stage of mixing that ultimately leads the entropy to increase.

Additionally, we implemented a Rayleigh dampening layer in the top 7000 m of the vertical domain with a dampening coefficient of $\alpha = 1/300$ s to damp out upward propagating gravity waves. Table 3.2 lists the initial parameters for all CM1 test cases explored in this study. For simplicity, we label each test case with a number which is listed in Table 3.2.

Table 3.2 Initial atmospheric sounding parameters and domain size used for the CM1 initial value problem simulations.

CM1 Test Case	T_s K	T_1 K	$q_{v,s}$ kg/kg	$q_{v,1}$ kg/kg	z_1 m	z_2 m	Domain (Lx, Ly, Lz) km	nx	nz
1 Isothermal Earth Air	450	450	0.5	0.0	18638	24863	(30, 30, 75)	200	1000
2 Isothermal H_2	450	450	0.0	0.5	216195	288405	(400, 400, 870)	200	1000
3 Isothermal CO_2	450	450	0.5	0.0	18638	24863	(30, 30, 75)	200	1000
4 Non-isothermal Earth Air	450	400	0.5	0.0	18638	24863	(30, 30, 75)	200	1000
5 Non-isothermal H_2	700	400	0.5	0.0	216195	288405	(400, 400, 870)	200	1000
6 Non-isothermal CO_2	450	400	0.3	0.0	18638	24863	(30, 30, 75)	200	1000
7 CTE T(p) Earth Air	450	400	0.1 - 0.7	0.0	18375	24625	(300, 300, 75)	200	300
8 CTE T(p) H_2	700	400	0.1 - 0.7	0.0	218250	290250	(1200, 1200, 900)	200	200
9 CTE T(p) CO_2	450	400	0.1 - 0.5	0.0	18375	24625	(300, 300, 75)	200	300
10 CTE q_v(p) Earth Air	400	450, 500, 550	0.3	0.0	18375	24625	(300, 300, 75)	200	300
11 CTE q_v(p) H_2	700	500, 600, 700	0.3	0.0	218250	290250	(1200, 1200, 900)	200	200
12 CTE q_v(p) CO_2	450	450, 500, 550	0.3	0.0	18375	24625	(300, 300, 75)	200	300

Cases 1 - 6 list the CM1 parameters for the high resolution simulations. Cases 7 - 12 list the CM1 setup for the parameter study simulations. Cases 1 - 3 use sounding profile 1, and Cases 4 - 12 use sounding profile 2. z_1 and z_2 represent the heights specified within CM1 at which the density discontinuity starts and ends, corresponding to p_1 and p_2 respectively. The domain is provided in km, and nx and nz are the number of grid points in the horizontal and vertical respectively. In Case 5, we use T_s = 700 K because surface temperatures set between 450 K to 650 K (in increments of 50 K) showed minimal to no convection when $q_{v,s}$ = 0.5. Various domain sizes and resolutions were tested initially. We settled on a domain size and resolution where the computation time was relatively fast compared to other setups, and the resolution was high enough to resolve the convective plumes when the simulation is initialized with random perturbations only. In the parameter study (Case 7 - 12) the resolution was reduced to save computational time but the simulation outputs were compared with the high resolution cases to ensure the resolution did not substantially affect the predicted 1D temperature and mass mixing ratio profile of the final state.

3.2.1 High Resolution CM1 Simulations

For the high-resolution simulations, we use $q_{v,s}$ = 0.5 kg/kg, T_s = 450 K and T_1 = 400 K for the Earth-air atmosphere case with both sounding profiles and the CO_2 atmospheres with sounding profile 1. For the CO_2 atmosphere case with sounding profile 2, having $q_{v,s}$ = 0.5 kg/kg caused the full atmospheric domain to mix which led CM1 to become numerically unstable in the high resolution simulations. With $q_{v,s}$ = 0.5 kg/kg and sounding profile 2, we observed numerical artifacts from the interaction of convection with the upper boundary of the simulation domain. For this case, we set $q_{v,s}$ = 0.3 kg/kg to run CM1 in a more stable configuration with T_s = 450 K and T_1 = 400 K.

For the isothermal hydrogen atmosphere test case (sounding profile 1), having a water vapor tracer in the lower part of a hydrogen atmosphere is convectively stable. Therefore, we initially place the water vapor tracer in the upper atmosphere with no H_2O(v) in the lower part of the atmosphere and use a step mass mixing ratio profile given by $q_v = 0$ from $p_s > p > p_1$ and $q_v = 0.5$ from $p_2 > p > p_{\mathrm{TOA}}$. Again, a linear relationship between mass mixing ratio and height is used to smear out the density interface between p_1 and p_2. Secondly, for the non-isothermal hydrogen atmosphere test case (sounding profile 2), we use T_s = 700 K and T_1 = 400 K to create positive buoyancy of the atmospheric parcels in the lower half of the atmosphere where H_2O is present with $q_v = 0.5$. Note, here the absolute value of temperature does not affect the simulation results since the temperature and mass mixing ratio are set independently of each other. We chose to set the minimum atmospheric temperature at 400 K since water does not condense at this temperature. For the H_2 atmosphere case, the lower atmosphere temperature was set to be the first temperature at which we observed any significant convection within the CM1 simulation results when $q_{v,s} = 0.5$.

The CM1 domain for the Earth-air and CO_2 atmosphere is (Lx, Ly, Lz) = (30, 30, 75) km, and for the H_2 atmosphere is (Lx, Ly, Lz) = (400, 400, 870) km. The vertical domain height

was set such that p_{TOA} is approximately $\mathcal{O}(10^3)$ Pa and the vertical domain is representative of an atmospheric column. A vertical resolution of 75 m and horizontal resolution of 150 m is used for the Earth-air and CO_2 atmosphere simulations. For the H_2 atmosphere, we used a 870 m and 1000 m vertical and horizontal resolution respectively.

Finally, for all six high resolution CM1 test cases, we explored the effect of two different initializations. First, we ran all of the test cases with initial small-scale random perturbations in potential temperature (θ) with an amplitude of $\pm$ 0.5 K. Second, we performed the CM1 test cases initialized with both random small-scale perturbations and a large-scale sinusoidal perturbation of the form,

$$\theta' = \sin\left(\frac{2\pi \mathrm{x}}{0.75\mathrm{W}}\right)\sin\left(\frac{2\pi \mathrm{y}}{0.75\mathrm{W}}\right)\sin\left(\frac{2\pi \mathrm{z}}{2\mathrm{H}}\right), \tag{3.1}$$

where θ' is the potential temperature perturbation, W is the width of the CM1 horizontal domain for the given test case, and H is a vertical scale height which is set to 50 km for the Earth-air and CO_2 atmosphere and 500 km for the H_2 atmosphere test cases. Using only random perturbations in θ produces small-scale vertical displacements of the initial state, which allows us to explore the Ledoux criterion condition with CM1 (Eqn. 2.19). When using random small-scale initial perturbation, the shortest wavelengths resolved are the most unstable and will lead to the formation of small-scale turbulent plumes. Conversely, the sinusoidal perturbation in θ creates a large, finite displacement of an atmospheric air parcel. Random perturbations were added in conjunction with the sinusoidal wave to add variation to the horizontal domain. When the initial condition is dominated by a large-scale perturbation, a large-scale coherent plume has the potential to grow to a finite amplitude before the small-scale instabilities take over. Using a large-scale perturbation allows us to explore compositional convection with finite amplitude vertical displacements of an air parcel, test the sensitivity of the final state to spatial scales excited in the system, and evaluate whether the Ledoux criterion is still sufficient in describing the final atmospheric

state. All CM1 cases were run long enough for the atmospheric state to converge to a final marginally stable state. The Earth-air and CO_2 atmosphere were run for 3600 seconds, while the H_2 atmosphere test cases were run for 8640 seconds.

For CM1 Case 1–3, which use sounding profile 1, the compositional gradient creates atmospheric instability which overcomes the stable isothermal temperature profile. For Case 4 and 6, both the temperature and compositional gradient render the initial profile unstable to convection. For Case 5, the H_2 atmosphere with sounding profile 2, the compositional gradient stabilizes the atmosphere while the temperature gradient creates an initial profile that is unstable to convection. Case 1, which models an isothermal Earth-air atmosphere, is similar to a *hot Earth* but with a greater compositional enhancement of buoyancy due to the larger value of q_v considered in this work. This case is relevant to planets with N_2 background atmospheres over an ocean, which are much hotter than Earth and therefore have a higher q_v. Hot Earth planets would be saturated and thus have condensation and latent heat release. Our non-condensing calculation does capture part of the hot Earth case, but latent heat release would make convective mixing more vigorous. Case 3, the isothermal CO_2 atmosphere, would be relevant for terrestrial exoplanets with a higher molecular weight atmosphere over a CO_2 ocean. Lastly, the hydrogen atmosphere cases look to explore compositional effects for sub-Neptune exoplanet atmospheres. Even though the simulations here do not fully represent the exoplanets we aim to study, they are important because they illustrate the role compositional buoyancy would play in such atmospheres.

3.2.2 CM1 Parameter Study

The parameter study explores how varying the initial compositional and temperature gradient respectively would affect the final atmospheric profiles after mixing. The parameter study is performed using sounding profile 2. In the parameter study, we run a set of simulations where we (1) varied the initial lower atmospheric mass mixing ratio value, $q_{\mathrm{v,s,initial}}$,

while keeping the temperature profile constant; (2) varied the initial lower atmosphere T_s value while keeping the q_v profile fixed. In CM1, the start of the smeared out discontinuity location is fixed to occur at a given height. Since both composition and temperature contribute to density, the start of the density discontinuity occurs at different pressure levels for the same given height within a set of simulations for a given atmosphere.

For the constant T(p) parameter study simulations, we vary $q_{\mathrm{v,s,initial}}$ from 0.1 to 0.7 in increments of 0.2. For the CO_2 atmosphere, the test case with $q_{\mathrm{v,s,initial}} = 0.7$ became numerically unstable and is excluded from the results. For the Earth-air and CO_2 atmospheres, T(p) is given by a step profile described by sounding profile 2 with $T_{\mathrm{s,initial}} = 450$ K and $T_{\mathrm{1,initial}} = 400$ K. For the H_2 atmosphere, $T_{\mathrm{s,initial}} = 700$ K and $T_{\mathrm{1,initial}} = 400$ K.

For the constant q_v(p) parameter study simulations, we vary $T_{\mathrm{s,initial}}$ from 400 to 550 K in increments of 50 K for the Earth-air and CO_2 atmospheres simulations, and vary $T_{\mathrm{s,initial}}$ from 500 to 700 K in increments of 100 K for the H_2 atmosphere simulations. For all three atmospheric compositions, $T_{\mathrm{1,initial}} = 400$ K and the mass mixing ratio profile is given by the step profile described by sounding profile 2 where $q_{\mathrm{v,s,initial}} = 0.3$ and $q_{\mathrm{1,initial}} = 0.0$.

The CM1 simulation setup for the parameter study is summarized by Cases 7 - 12 in Table 3.2. We employ a CM1 domain for the Earth-air and CO_2 atmospheres with dimensions $(Lx, Ly, Lz) = (300, 300, 75)$ km with a horizontal resolution of 1500 and vertical resolution of dz = 250 m. For the H_2 atmosphere, the domain is $(Lx, Ly, Lz) = (1200, 1200, 900)$ km with a horizontal resolution of 6000 m and vertical resolution of 4500 m. All CM1 simulations in the parameter study were run with initial small-scale random perturbations to trigger convection, and the simulations were run for 8640 seconds. Due to the lower resolution employed in the parameter study, we do not fully resolve the smallest scale plumes that form at the initial stages of the simulation. But, we do find that the final atmospheric state from the low resolution simulation matches the results from corresponding high resolution simulations. We reduced the resolution of these runs to save computational time.

3.3 CM1 Simulation Results & Discussion

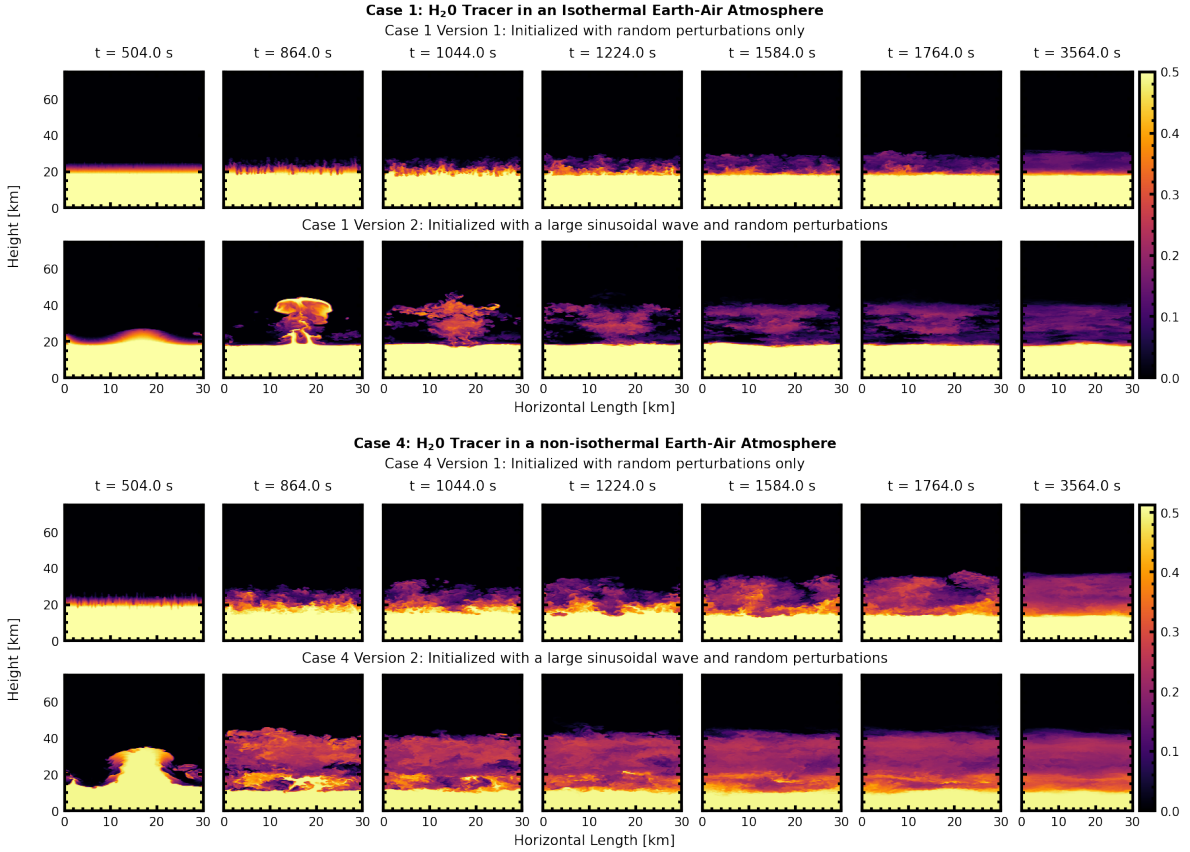

Fig. 3.1 2D plots showing vertical cross-sections of mass mixing ratio taken in the middle of the y-domain for CM1 Case 1 and Case 4 which have an Earth Air Atmosphere. The top panel shows the q_v cross-sections for Case 1, isothermal Earth air atmosphere, while the bottom panel shows the q_v cross-section for Case 4, Earth-Air atmosphere with initial temperature and mass mixing ratio step profile. Within each panel, the top row shows the results when using only initial random perturbations to trigger convection, while the bottom row shows the results when using the initial perturbation given by Eqn. 3.1 in conjunction with random perturbations. The mass mixing ratio is shown for seven different time steps during the CM1 simulation. The color bar indicates the value of q_v. The plots show the formation, growth, and mixing of convective plumes. Eventually, the atmosphere reaches a marginally stable state where discrete layers of varying composition form. The observed *compositional staircases* are analogous to the compositional staircases presented in compositional convection modeling for stellar atmospheres (Garaud et al., 2015).

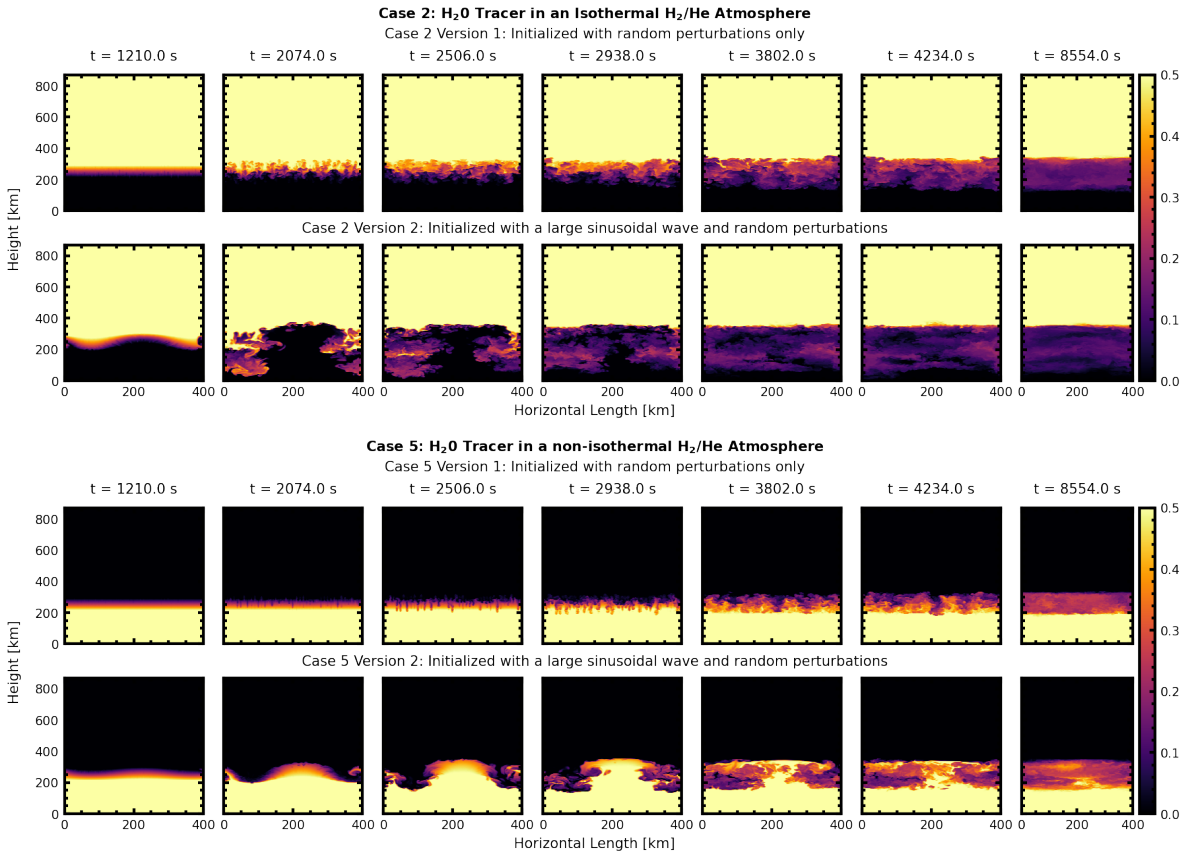

Fig. 3.2 Same as Fig. 3.1 but for the H_2 atmosphere test cases. The top panel shows 2D vertical cross-sections of the mass mixing ratio taken in the middle of the y-domain for Case 2, while the bottom panel shows the results for Case 5.

3.3.1 High Resolution CM1 Simulation Results Overview

Figs. 3.1–3.3 show vertical cross-sections of mass mixing ratio taken in the middle of the y-domain at seven time steps throughout the CM1 simulation for all six high resolution test cases. Fig. 3.1 shows the vertical cross-sections for the Earth air atmosphere with Cases 1 and 4 in the top and bottom panel respectively. Fig. 3.2 shows the vertical cross-sections for the H_2 atmosphere with Case 2 in the top panel and Case 5 in the bottom panel. Fig. 3.3 shows q_v vertical cross-sections for CO_2 atmosphere with Case 3 in the top panel and Case 6 in the bottom panel. Within each panel, the top row of Figs. 3.1–3.3 shows the q_v cross-sections when CM1 is initialized with initial random perturbations in θ, while the bottom row shows

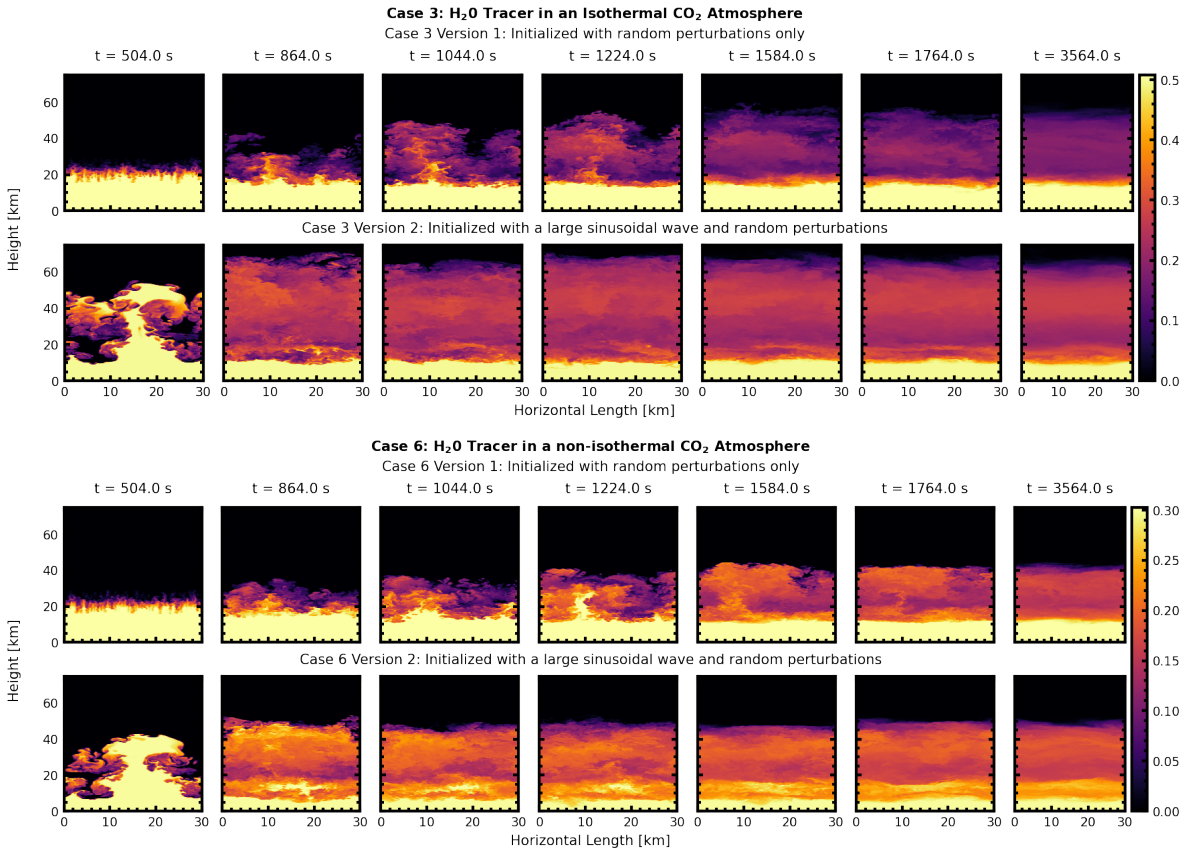

Fig. 3.3 Same as Fig. 3.1 but for the CO_2 atmosphere test cases. The top panel shows 2D vertical cross-sections of the mass mixing ratio taken in the middle of the y-domain for Case 3, while the bottom panel shows the results for Case 6. Note that in Case 6, $q_v, s = 0.3$ kg/kg, and thus the color bar for Case 6 is not equivalent to the color bar shown for Case 3.

the mass mixing ratio when CM1 is run with an initial large sinusoidal perturbation in addition to random perturbations in θ. In Case 2 shown in the top panel of Fig. 3.2, the yellow and black regions are flipped compared to the other test cases since H_2O tracer was placed in the upper part of the atmosphere to create an initial unstable compositional gradient.

The initial step profile which is the basis for our compositional convection CM1 test cases is an instance of the Rayleigh-Taylor instability. The Rayleigh-Taylor instability describes a fluid dynamic instability at the interface of two fluids, where a lighter fluid is pushing a heavier fluid (Zhou, 2017; Gauthier and Le Creurer, 2010). A visual characteristic of Rayleigh-

Taylor instabilities are mushroom-shaped plumes. Rayleigh-Taylor instabilities manifest as normal mode instabilities of the system linearized about the state of rest, and grow exponentially until adjacent plumes start mixing and the instability transitions to a turbulent mixing regime (Zhou, 2017). The formation, growth, and mixing of mushroom-shaped clouds is clearly visible within the mass mixing ratio cross-sections shown in Figs. 3.1–3.3.

The vertical cross-sections of q_v in Figs. 3.1–3.3 show that the large-scale initial perturbation creates a single coherent plume which rises a finite amount and then mixes horizontally within the domain. The simulations initialized with a large-scale perturbation show that the convecting plume penetrates deeper into the vertical domain, creating a deeper mixing layer relative to the simulations initialized with small-scale perturbations. Additionally, the mass mixing ratio does not mix as uniformly within the horizontal domain in the simulations initialized with a large-scale perturbation. Conversely, when CM1 is initialized with random perturbations, small-scale plumes form within the horizontal domain, grow and start to mix the horizontal domain and a subset of the vertical domain, but do not penetrate as deep into the vertical domain compared to the simulation results when using an initial large sinusoidal perturbation.

The vertical cross-sections presented in Figs. 3.1–3.3 supports our assumption in Section 2.2.2 that an air parcel maintains its composition as it rises adiabatically within the atmosphere. It is clear in the bottom rows of Figs. 3.1–3.3 that as an air parcel is rising, it keeps its composition from the parcel's initial location. After the air parcel seems to have reached marginal stability, convection begins to mix the composition of the parcel with the environment.

Additionally, when comparing Case 1 to the Case 4 in Fig. 3.1, it is visually apparent that Case 4 mixes deeper within the vertical domain. This is because Case 4 uses sounding profile 2 in which positive buoyancy is generated by both the T and q_v profiles. In contrast, in Case 1, buoyancy is generated solely from the compositional gradient. This trend is not

observed when comparing Case 3 and Case 6 in Fig. 3.3 because we reduced the $q_v, s = 0.3$ in Case 6 due to CM1 becoming too numerically unstable. If we had used $q_{v,s} = 0.5$ for the initial state in Case 6, we would expect convective mixing deeper in the atmospheric column compared to Case 3. The bottom panel of Fig. 3.2 shows Case 5, where we had a large temperature gradient overcome the compositional suppression of buoyancy. Case 5 shows the least amount of mixing of the H_2O tracer within the atmospheric column, which can be attributed to the competing effects of the temperature and compositional gradient. In all six high resolution test cases, the H_2O tracer does not fully homogenize the vertical column but is seen to form stable layers of varying composition.

We evaluated the CAPE of the initial atmospheric sounding state, using Eqn. 2.38, for all of our high resolution CM1 test cases to determine the predicted mixing zone – the region in which we expect convection to occur. The predicted mixing zone is the region within the atmosphere where an air parcel, if perturbed a finite amount, can generate positive CAPE. The predicted mixing zone represents the region in the initial atmospheric state that is convectively unstable. To determine the predicted mixing zone, we evaluate the CAPE of air parcels starting from various heights within the initial virtual temperature profile. For the given initial atmospheric sounding state, an air parcel starting at p_1 (the pressure at the start of the smeared out density discontinuity) generates the maximum amount of positive CAPE, which sets the upper bound for the predicted mixing zone. Any parcel starting $p_1 > p > p_2$, will generate positive CAPE when lifted a finite amount but produces less CAPE than the parcel that is lifted from p_1. Any parcel starting from $p < p_2$ will only generate negative CAPE and is convectively stable. An air parcel starting from $p_1 < p < p_{\text{min CAPE}}$ will first generate negative CAPE, but if the parcel is lifted enough, at some point the rising air parcel's adiabat will intersect the atmospheric virtual temperature profile. At this point, the air parcel has reached an unstable neutral buoyancy point, and if the parcel is lifted upward an infinitesimal amount the parcel will freely rise in the atmosphere until it reaches its LNB.

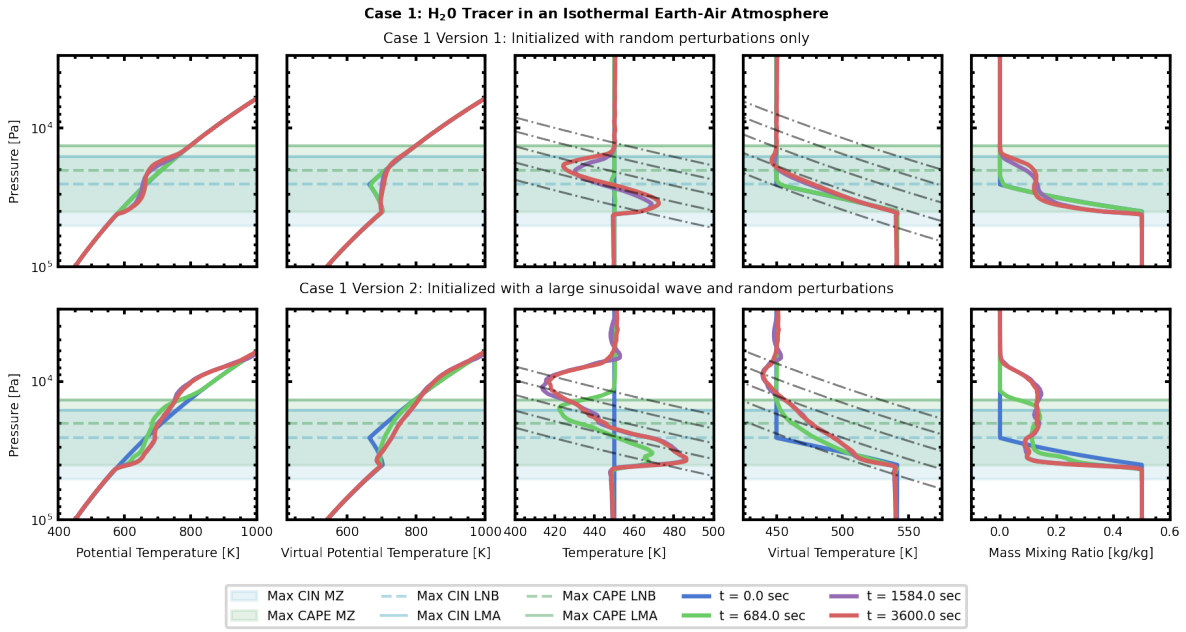

Fig. 3.4 Vertical profiles from left to right of $\theta(p)$, $\theta_v(p)$, $T(p)$, $T_v(p)$, and $q_v(p)$ with respect to pressure for Case 1, isothermal Earth-air atmosphere with an initial non-condensing H_2O in the lower half of the atmosphere. The vertical profiles for $\theta(p)$, $T(p)$, and $q_v(p)$ are determined by taking the horizontal average of the output 3D CM1 data. $T_v(p)$ and $\theta_v(p)$ are calculated using horizontally averaged $T(p)$ and $q_v(p)$ profiles. The colored lines represent the atmospheric vertical profiles at different four time steps during the CM1 simulation, where the initial state is given by a blue line and the final state is the red line. The blacked dashed lines show uniform composition dry adiabats, calculated using Eqn. 2.14,in the temperature panel, and virtual adiabats, calculated using Eqn. 2.17, in the virtual temperature panel. The blue-green shaded region shows the predicted mixing zone from a CAPE analysis performed on the initial atmospheric sounding state using Eqn. 2.38. Finally, the top row shows the vertical profiles when CM1 Case 1 was run using only random perturbations to trigger convection, while the bottom row shows the results when convection is triggered with both random perturbations and a large sinusoidal wave given by Eqn. 3.1. Case 1 version 2 shows the least agreement of where convection occurred to the predicted mixing zone.

$p_{\text{min CAPE}}$ is the pressure location greater than p_1, where an air parcel's virtual adiabat would intersect at p_2. An air parcel rising from $p \geq p_{\text{min CAPE}}$ will only generate negative CAPE and is convectively stable. $p_{\text{min CAPE}}$ represents the lower bound in the atmospheric column from where an air parcel can no longer generate positive CAPE. We set the lower bound of the predicted mixing zone at $p_{\text{min CAPE}}$. In some cases $p_{\text{min CAPE}}$ was calculated to be

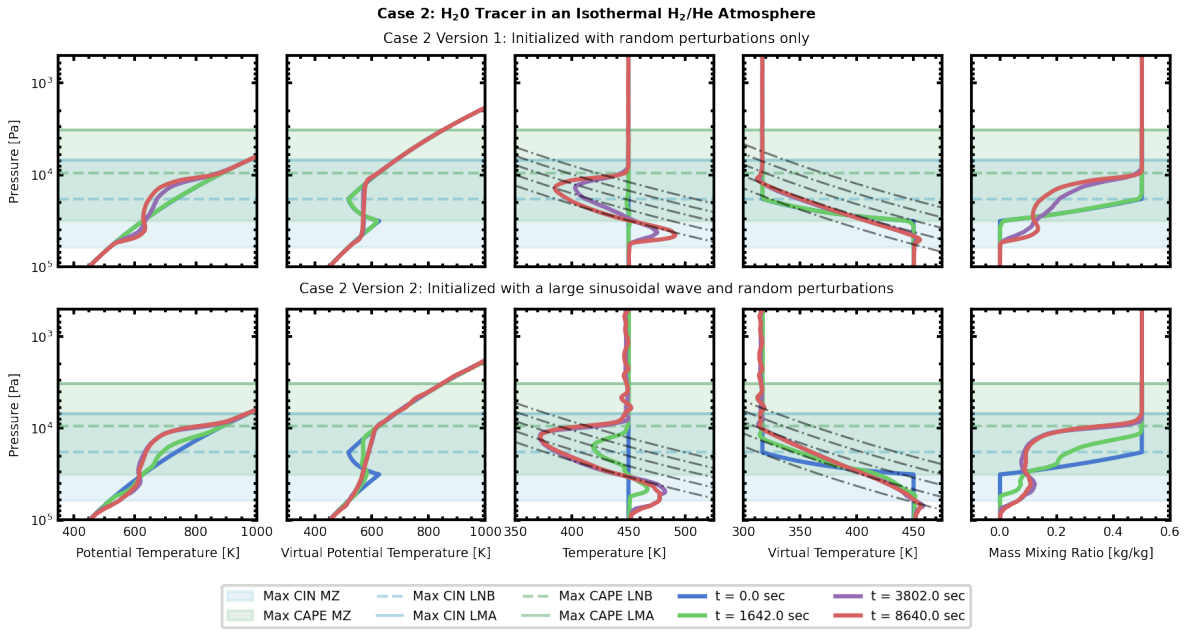

Fig. 3.5 Same as Fig. 3.4 but showing the CM1 vertical profiles for Case 2, isothermal H_2 atmosphere with an initial non-condensing H_2O in the lower half of the atmosphere. In Case 2, we observe more mixing in the blue region of the predicted mixing zone compared to the other test cases, which can be attributed to compositionally dense air sinking from the upper part of the atmosphere to the lower part of the atmosphere.

greater than p_s, so we adjusted $p_{\text{min CAPE}} = p_s$. The lower region of the predicted mixing zone represents the maximum amount of negative CAPE a parcel needs to overcome to freely rise within the initial sounding state.

In Figs. 3.4-3.9, we show the predicted mixing zone as the shaded blue-green region. The green shaded region represents the upper bound of the mixing zone and is determined by a parcel starting at p_1, while the blue shaded region is the lower bound of the predicted mixing zone given by a parcel rising from $p_{\text{min CAPE}}$. White regions represent convectively stable regions. Both the blue and green regions start at their respective initial parcel locations and end at their respective LMA. The dark green region is the overlap of the blue and light green regions. Within each panel of Figs. 3.4–3.9 we show the LNB as a dashed horizontal line and LMA as a solid horizontal line for the both the upper and lower bound of the predicted mixing zone in green and blue respectively.

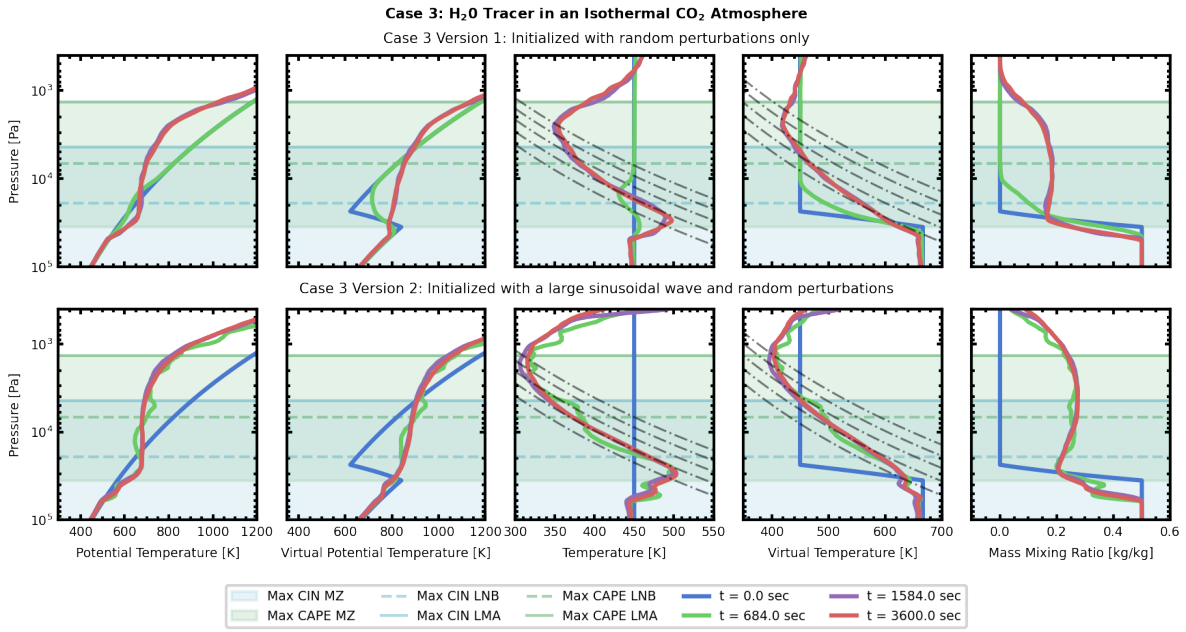

Fig. 3.6 Same as Fig. 3.4 but showing the CM1 vertical profiles for Case 3, isothermal CO_2 atmosphere with an initial non-condensing H_2O in the lower half of the atmosphere. As expected, we observe greater compositional enhancement of buoyancy in the CO_2 atmosphere compared to the Earth air atmosphere with the same initial $q_v(p)$ profile shown in Fig. 3.4.

Figs. 3.4–3.9 show the vertical atmospheric sounding state for each of the high resolution CM1 test cases respectively. In each figure, the top row shows the final atmospheric state of the CM1 test case initialized with small-scale random perturbations in θ. The bottom row shows the final atmospheric state for the same CM1 test case, but initially perturbed in θ with both random perturbations and a sinusoidal wave given by Eqn. 3.1. The five panels in each row show (from left to right) the vertical atmospheric profile of potential temperature, virtual potential temperature, temperature, virtual temperature, and mass mixing ratio at four different time steps from the CM1 simulation as shown by different colored solid lines. The vertical profiles for temperature, potential temperature, and mass mixing ratio are calculated by taking the horizontal average of the output 3D CM1 data for T, θ, and q_v as a function of height. The virtual temperature and virtual potential temperature profiles are calculated by using the horizontally averaged 1D temperature and

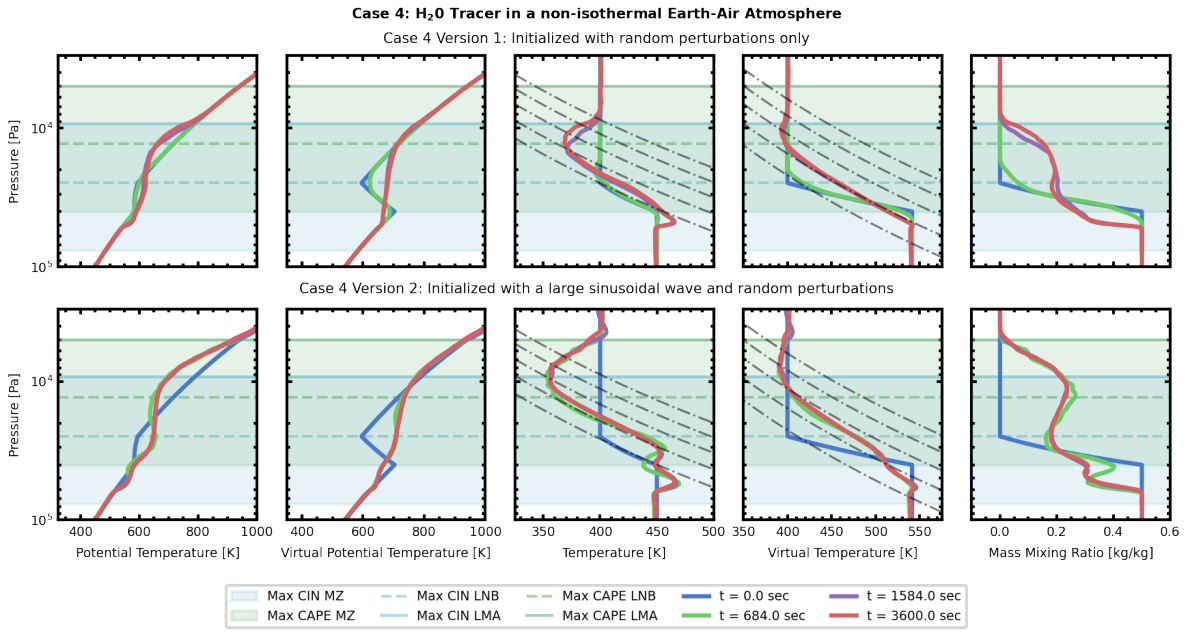

Fig. 3.7 Same as Fig. 3.4 but showing the CM1 vertical profiles for Case 4, Earth air atmosphere with an initial step profile in both T and q_v profiles. Case 4 has a larger predicted mixing zone than Case 1 due to both temperature and composition contributing to buoyancy.

mass mixing ratio profiles. The black dashed lines plot uniform composition dry adiabats in the temperature panel, calculated using Eqn. 2.14, where β_{mix} is constant and has a value of $R_b/C_{p,b}$. The black dashed lines plot virtual adiabats, calculated using Eqn. 2.25, in the virtual temperature profile panel, where β_{mix} is assumed to be an approximately constant value given by $\beta_{\text{mix}}(p_1)$. The effect of using different values for β_{mix} in calculating the virtual adiabat is relatively minor.

3.3.2 Discussion of CM1 Results

What is the final compositional profile after convective mixing in an initially inhomogeneous composition atmosphere?

Within Figs. 3.4–3.9, the mass mixing ratio panel shows that q_v does not fully homogenize within the predicted mixing zone since a stable atmospheric state was reached before this

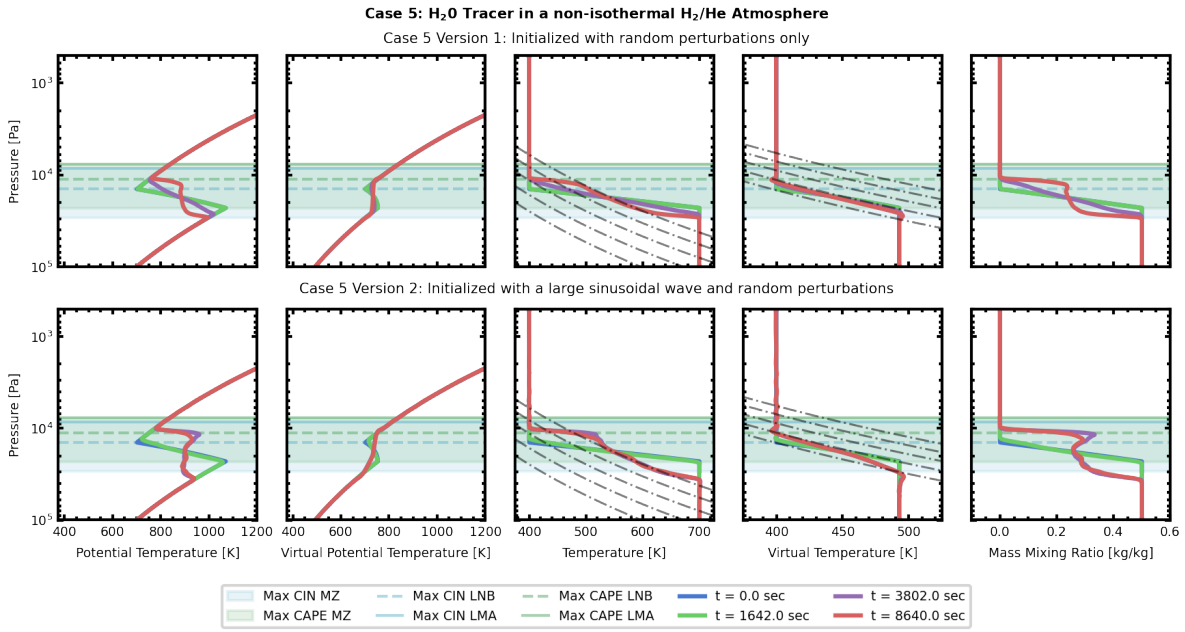

Fig. 3.8 Same as Fig. 3.4 but showing the CM1 vertical profiles for Case 5, H_2 atmosphere with an initial step profile in both T and q_v profiles. Case 5 is the only CM1 test case performed where the compositional gradient suppresses buoyancy while the thermal gradient enhances buoyancy. Case 5 shows the least amount of convective mixing within the vertical domain, which illustrates that the compositional gradient can strongly stabilize the atmospheric profile against convection in H_2 atmospheres.

could occur. Mixing is observed to occur within a subset of the predicted mixing zone for all six high resolution test cases, creating a staircase-like profile for the final state mass mixing ratio. Case 3 version 2 shown by the bottom panel in Fig. 3.6 is observed to have the largest amount of mixing and nearly homogenizes the final state mass mixing ratio. When using the large sinusoidal perturbation (version 2 results) in Case 4 shown in Fig. 3.7, and Case 6 shown in Fig. 3.9, there seem to be two *stairs* of q_v that form within the predicted mixing zone. The mass mixing ratio profile's *compositional staircases* are similar to results of compositional convection effects in stellar atmospheres and thermohaline convection within Earth's oceans (Stern, 1960; Radko, 2003; Garaud, 2018). However, it should be noted that compositional staircases in Earth's ocean are formed due to double-diffusive convection of heat and salinity, whereas our simulations model inhomogenous mixing which show the formation of mixing

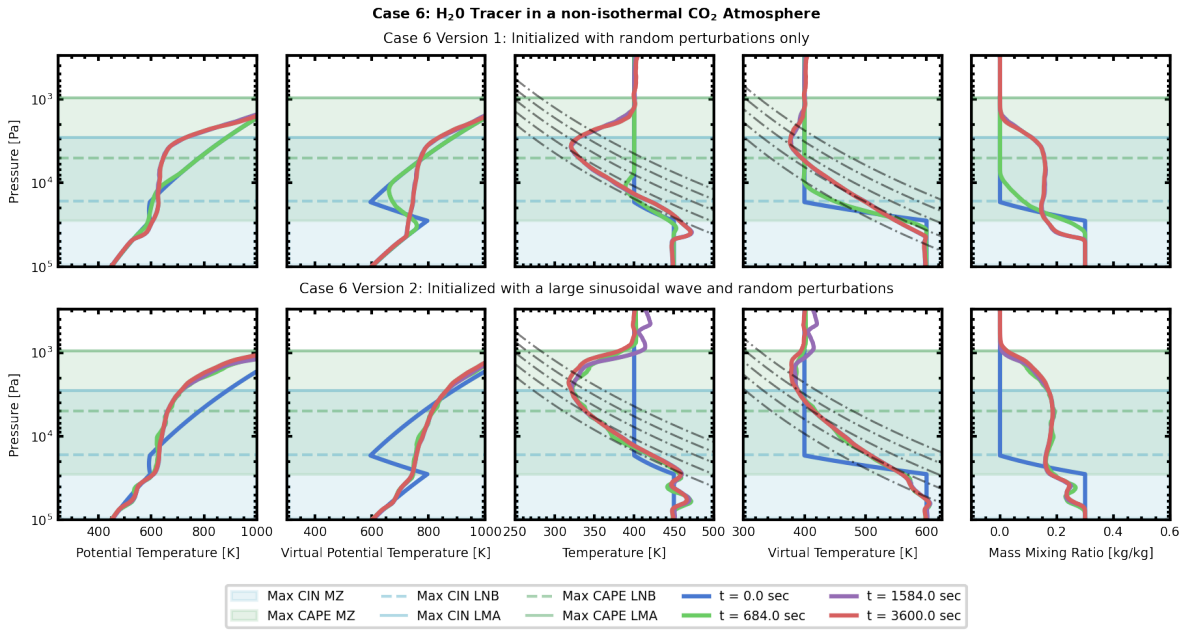

Fig. 3.9 Same as Fig. 3.4 but showing the CM1 vertical profiles for Case 6, CO_2 atmosphere with an initial step profile in both T and q_v profiles. Case 6 used an initial value of $q_v, s = 0.3$ kg/kg in the lower atmosphere due to CM1 becoming too unstable and crashing when using higher values of q_v, s.

barriers due to the fluid becoming convectively stable. The formation of compositional staircases suggests that there are discrete layers of varying values of q_v that form within the final state. This is also seen in the 2D vertical cross-sections of q_v shown in Figs. 3.1–3.3 for all six high resolution test cases. Note, the formation of compositional staircases poses a challenge for accurate parameterization of compositional convection, because the shape of the final q_v profile becomes hard to predict without numerical simulations.

To further explore how convection mixes the atmospheric tracer in initially inhomogeneous composition atmospheres, we performed two parametric studies with sounding profile 2 where we (1) varied the initial lower atmospheric mass mixing ratio value, $q_{\text{v,s,initial}}$, while keeping the temperature profile constant shown in Fig. 3.10; (2) varied the initial lower atmosphere T_s value while keeping the q_v profile fixed shown in Fig. 3.11. Varying the lower atmospheric mass mixing ratio and temperature leads to varying the compositional and temperature gradient respectively for our CM1 simulation setup.

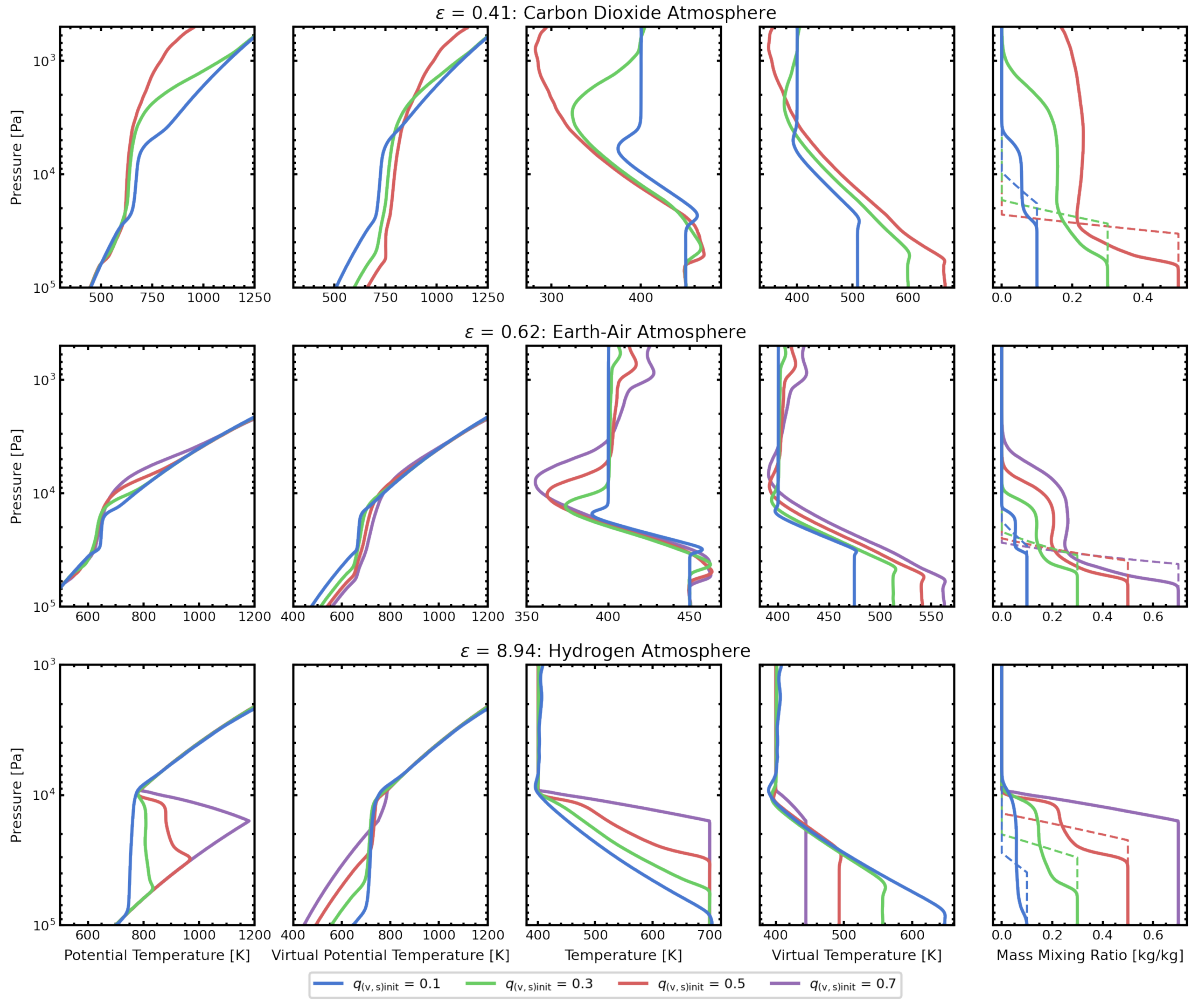

Fig. 3.10 Parameter study of the effect of varying the initial compositional gradient while keeping the initial temperature profile fixed. The initial atmospheric state for these simulations is defined by sounding profile 2 with: 1. temperature step profile with $T_{\text{upper}} = 400$ K and $T_{\text{lower}} = 450$ K for $\epsilon < 1$ cases, and $T_{\text{lower}} = 700$ K for $\epsilon > 1$ case; 2. an initial q_v step profile with $q_{\text{v, upper}} = 0.0$ and $q_{\text{v, lower}}$ varying from 0.1 to 0.7. The dashed profiles in the mass mixing ratio panel plot the initial atmospheric state q_v profiles for reference. For the $\epsilon < 1$ cases, increasing the compositional gradient leads to more vigorous convective mixing and for the CO_2 atmosphere, more homogenization of the final state mass mixing ratio profile. Conversely, for the $\epsilon > 1$ case, increasing the compositional gradient leads to the suppression of convection. The vertical profiles presented here are averages of the horizontal domain. All simulations presented here are run for 8640 seconds. The resolution was reduced to save computation time.

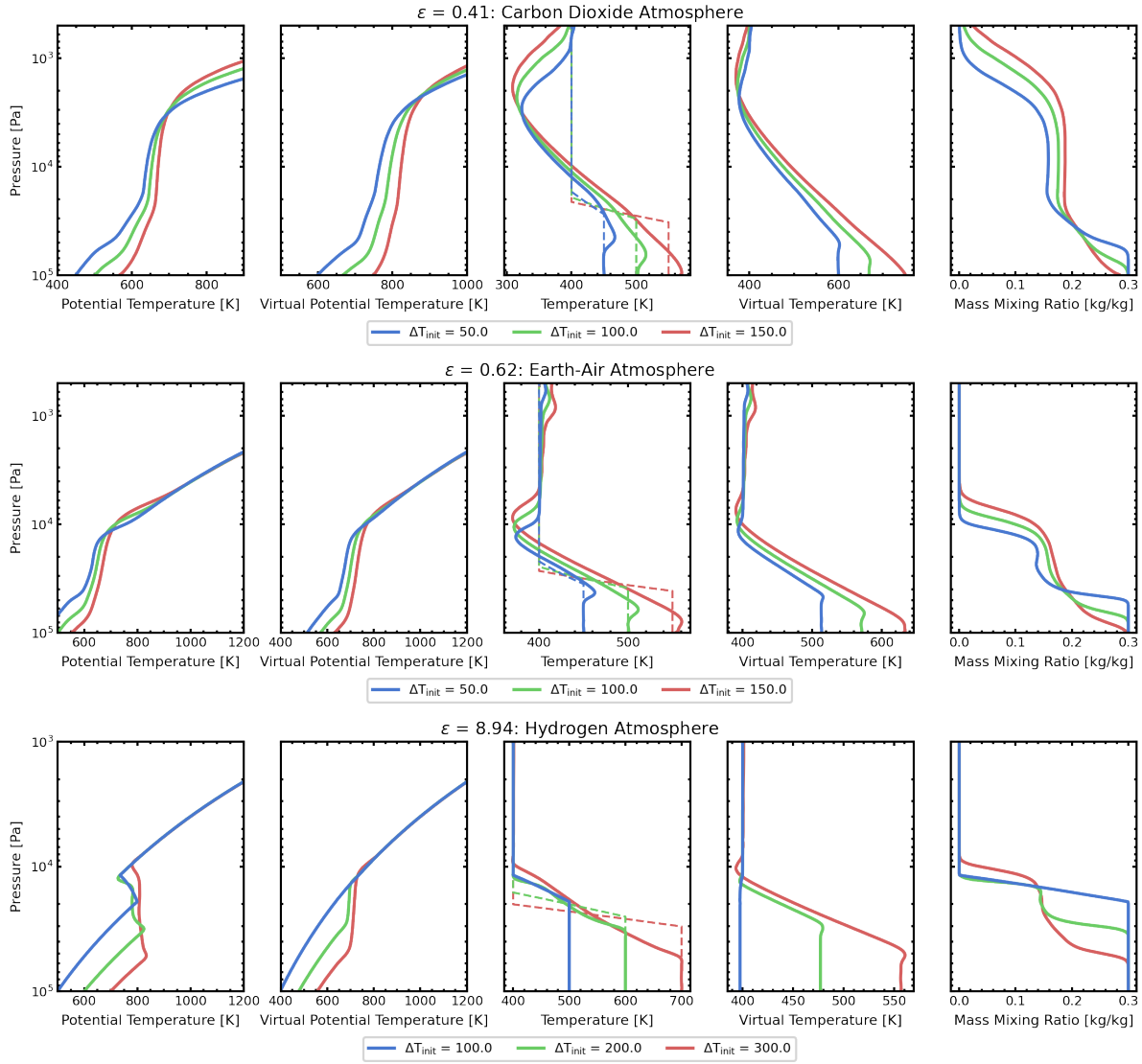

Fig. 3.11 Parameter study of the effect of varying the initial temperature gradient while keeping the initial compositional profile fixed. The initial atmospheric state for these simulations is defined by sounding profile 2 with: 1. temperature step profile with T_{upper} = 400 K and T_{lower} varying from 450 K to 550 K for $\epsilon < 1$, and T_{lower} varying from 500 K to 700 K for $\epsilon > 1$ case; 2. an initial q_v step profile with $q_{\text{v, upper}} = 0.0$ and $q_{\text{v, lower}} = 0.3$. The dashed profiles in the temperature panel plot the initial atmospheric state profiles for reference. $\Delta T_{\text{init}} = T_{\text{lower}} - T_{\text{upper}}$ for the initial state atmosphere. For the $\epsilon < 1$ cases, increasing the temperature gradient leads to more vigorous convective mixing and more homogenization of the final state mass mixing ratio profile. For the $\epsilon > 1$ case, increasing the temperature gradient leads to the formation of larger compositional staircases. The vertical profiles presented here represent averages of the horizontal domain. All simulations presented here are run for 8640 seconds. The resolution was reduced to save computation time.

Fig. 3.10 shows the final state atmospheric profiles for CM1 simulations starting with $q_{\mathrm{v,s,initial}}$ ranging from 0.1 to 0.7 while keeping the temperature profile constant. In the cases where $\epsilon < 1$, shown in the top (CO_2 atmosphere) and middle row (Earth Air atmosphere) of Fig. 3.10, increasing the initial amount of atmospheric tracer in the lower atmosphere further enhances convective buoyancy and results in more mixing. The CO_2 atmosphere case experiences a significantly larger compositional enhancement of buoyancy compared to the Earth Air atmosphere case. Due to this, having a larger initial $q_{\mathrm{v,s,initial}}$ in the CO_2 atmosphere leads to more homogenization of the final state compositional profile relative to the Earth air atmosphere.

In the case where $\epsilon > 1$ illustrated in the bottom row of Fig. 3.10, increasing the compositional gradient leads to less vertical mixing and eventually, the compositional gradient completely shuts off convection. When $q_{\mathrm{v,s,initial}} = 0.1$, convection mixes the final state lower atmosphere area to be uniform because the temperature gradient is able to overcome the compositional suppression of buoyancy. However, when $0.1 > q_{\mathrm{v,s,initial}} > 0.7$, we see the clear formation of compositional staircases. At $q_{\mathrm{v,s,initial}} = 0.7$, we observe no convection because the compositional gradient completely stabilizes the temperature gradient. In this case, the initial atmospheric state is Ledoux stable, $T_{\mathrm{v,parcel}} < T_{\mathrm{v,amb}}$ everywhere, therefore no convection was observed within CM1. Note, that in the $\epsilon > 1$ case we used a temperature step profile with ΔT between the upper and lower atmosphere of 300 K compared to the $\epsilon < 1$ case where $\Delta T = 50$ K. A large temperature step is needed in the H_2 atmosphere case to overcome the strong stabilization of convection due to the compositional gradient. We do not observe any convection in the H_2 atmosphere case when $\Delta T = 50$ K, even for the $q_{\mathrm{v,s,initial}} = 0.1$ case, because the initial sounding state is Ledoux stable.

Similarly, we show the effect of varying the initial lower atmosphere T_s while keeping the initial mass mixing ratio profile fixed with $q_{\mathrm{v,s,initial}} = 0.3$ and $q_{\mathrm{v,1,initial}} = 0.0$ using sounding profile 2 in Fig. 3.11. When $\epsilon < 1$, shown in the top (CO_2 atmosphere) and middle rows (Earth

Air atmosphere), increasing the temperature gradient leads to more vigorous convective mixing. When $\epsilon < 1$, increasing the initial temperature gradient causes the final atmospheric q_v to transition from a compositional staircase like regime to a more well-mixed homogeneous state. When $\epsilon > 1$, shown in the bottom row of Fig. 3.11, increasing the temperature gradient does increase the convective mixing but at a much slower rate relative to the $\epsilon < 1$ cases. In all three simulations run in the $\epsilon > 1$ case, the final mass mixing ratio profiles still show the formation of compositional staircases.

The parameter study in Figs. 3.10 - 3.11 is presented to highlight that the final state after convective mixing in an initially inhomogeneous composition atmosphere can still have a compositional gradient. For a large portion of the parameter study, we observe the formation of compositional staircases. The formation of compositional staircases suggests that a marginally stable final atmospheric state is reached prior to convection being able to fully homogenize the mixing layer (the region which was initially unstable to convection). Again, the formation of compositional staircases poses a challenge to accurately parameterizing compositional convection.

Does convection mix the final atmospheric state of an initially inhomogeneous composition atmosphere to a local or global neutrally stable state?

Convection relaxes to a state of global neutral stability when q_v homogenizes within the convectively unstable layer. When the final atmospheric state has compositional inhomogeneities within the mixing layer, the most general marginal stability condition is Ledoux local marginal stability (see Section 2.2.2). A large portion of the CM1 simulation results presented here show the formation of compositional staircases and variation of q_v within the predicted mixing zone suggesting that convection will likely mix an initially inhomogeneous composition atmosphere to a final *local* marginally stable state.

In Figs. 3.4–3.9, convective mixing observed within the simulations is limited to a subportion of the vertical domain that was initially unstable (blue-green shaded region) and is seldom observed to penetrate into regions that are initially statically stable. Regions outside the area where convective mixing primarily occurred kept their initial statically stable profiles. We only observe the convective plumes penetrating into statically stable regions in Case 1 and 3 when using the large-scale initial perturbation (version 2). In both of these test cases, the convective plume penetrated into the statically stable region before mixing with the horizontal domain. Note, accurately modeling penetrating convective plumes is a challenge in developing a convection parameterization scheme.

The virtual potential temperature profiles in Figs. 3.4–3.9, mimic a staircase like structure as well, suggesting the final state forms stably stratified layers. The same trend is observed in $\theta(p)$ for all cases except Case 5. In Case 5, shown in Fig. 3.8, the potential temperature profile shows a region where $d\theta/dz < 0$, however, the corresponding $d\theta_v/dz$ is approximately constant, suggesting that the compositional profile is still stabilizing the temperature profile in the final atmospheric state.

For the atmosphere to mix to a global marginally stable state, additional energy would need to be supplied to the system to further mix the atmosphere. Case 3 and 6 are the two cases that nearly reach global stability. Both of these cases have a large amount of CAPE in the initial atmospheric sounding, and also have the largest predicted mixing zones. Within the parameter study, the cases that are seen to nearly homogenize are cases where the density difference between the upper and lower atmosphere is the largest, and the system has substantially more CAPE in the initial state. Within the parameter study, again the CO_2 atmosphere test cases are the ones which are observed to mix towards homogenizing the atmosphere. We do not observe the Earth Air atmosphere cases mixing toward a global marginally stable state. This is because the CO_2 atmosphere has a significantly larger compositional enhancement of buoyancy compared to the Earth Air atmosphere.

CAPE can be a good indicator for determining whether the atmospheric system has enough energy to mix to a state of global or local marginal stability. Convection will mix an initially inhomogeneous composition atmosphere to a final state of local stability unless the initial state of the atmosphere has enough CAPE to fully mix the convectively unstable regions.

If convection mixes the atmosphere to a locally stable state, can it be described by the virtual adaibat?

The virtual temperature profiles shown in Figs. 3.4–3.9 evolve towards a virtual adiabat. When using small-scale initial displacements (top row of Figs. 3.4–3.9), the virtual temperature profile clearly evolves to have a final state that lies on a virtual adiabat. When using the large-scale initial perturbation, (bottom row of Figs. 3.4–3.9), the trend of the final atmospheric state evolving towards a virtual adiabat is still present but less clear. When using the large-scale initial perturbation, we observed in Figs. 3.1-3.3 that the horizontal domain does not mix as uniformly as when only using small-scale perturbations. Some of the deviation of the final $T_v(p)$ state from the virtual adiabat in the bottom row of Figs. 3.4–3.9 can be attributed to the horizontal domain variation, since these profiles are calculated as horizontal averages. In Case 1 version 2, shown in Fig. 3.4, convection started at a $p < p_1$, and the virtual adiabats plotted in Fig. 3.4 are calculated for a parcel rising from p_1.

The final state observed within the CM1 simulations is a virtual adiabat which describes a marginally Ledoux stable state. The final atmospheric state depends on both the final temperature and mass mixing ratio profiles. Without compositional variation in the final atmospheric state, the uniform composition dry adiabat specifies a unique state for the marginally stable system. When there is compositional variation in the final atmospheric state, there is a whole range of marginally stable final temperature and compositional profiles that correspond to the same virtual adiabat. Our CM1 simulations show that one

of the possible marginally stable compositional profiles is realized instead of the case were q_v completely homogenizes in the predicted mixing zone. This implies that a convection parameterization scheme needs to account for how convection redistributes composition.

Figs. 3.4-3.7, and Fig. 3.9 show the final $T(p)$ profile does not fully lie on the uniform composition dry adiabat but rather increases in the lower part of the atmosphere and cools in the upper part of the atmosphere. The temperature evolution can be attributed to compositionally buoyant air parcels rising from the lower part of the atmosphere and cooling the atmosphere adiabatically as the air parcels ascend, and vice versa. The extra compositional buoyancy allowed plumes to rise further than they otherwise would. For case 5 shown in Fig. 3.8, the temperature decreases in the lower part of the predicted mixing zone and heats in the upper part of the atmosphere. Case 5 is the only case where we have compositional suppression of buoyancy and the compositional buoyancy is opposing the thermal buoyancy. When the atmosphere mixes in Case 5, convection expends energy to lift a heavy air parcel from the lower part of the atmosphere, causing the temperature to decrease in the lower part of the predicted mixing zone. As a dense air parcel sinks, energy is released and the upper region of the predicted mixing zone heats. For all CM1 test cases studied here, convection transports energy upwards, which is seen by the virtual temperature profile heating the upper part of the mixing region while cooling in the lower part of the mixing zone.

Our simulation results for Case 5 show a trend in the final atmospheric temperature profile that is similar to the findings from compositional convection simulations presented in Daley-Yates et al. (2021). In their study, Daley-Yates et al. (2021) used a 3D hydrodynamics code to simulate a hot, rocky exoplanet atmosphere with a chemical reaction (i.e. forcing term) in the upper atmosphere that converted CO to CO_2, thus maintaining a compositional gradient within the atmosphere. The Daley-Yates et al. (2021) simulation setup used an initial stabilizing temperature gradient with an initial destabilizing compositional gradient

– compositional and thermal buoyancy are opposing each other. Even though the details of the simulation setup in Daley-Yates et al. (2021) differ from that presented in this work, their final temperature profile shows the same trend we observe for Case 5 where the lower atmospheric temperature deceases and the upper atmospheric temperature increases.

How do large-scale versus small-scale perturbations affect the final state after convective mixing?

Comparing results from the top and bottom rows of Figs. 3.4–3.9 show that using different initial perturbations results in notable differences in the final atmospheric state predicted by CM1. When using only random perturbations (seen in the top row of Figs. 3.4–3.9) convection starts at the discontinuity location p_1, and mixing occurs primarily in a subset of the predicted mixing zone given by the green region of the predicted mixing zone which is from [p_1, LMA maximum CAPE limit]. When using a large-scale sinusoidal perturbation (bottom row of Figs. 3.4–3.9), convective mixing is observed to occur in a larger extent of the predicted mixing zone. In particular, there is more observed mixing within the lower part of the blue shaded region and the upper part of the green maximum CAPE region. In some cases, the system *over-stabilizes*, i.e. leaves the virtual adiabat more stable than it needs to be, when using the large-scale perturbation. This is most pronounced in Cases 1, 3 and 6. Accounting for over-stabilization is an additional challenge to consider when developing a convection parameterization scheme.

For test case 1 version 2 in Fig. 3.4, and case 3 version 2 in Fig. 3.6 there is observed mixing outside of the predicted mixing zone. We believe the mixing outside of the predicted mixing zone bounds is due to convective overshoot, and is not enough to homogenize the atmospheric tracer or adjust to a virtual adiabat. Overall, when using a large-scale initial perturbation, an unstable air parcel; 1. can penetrate deeper in the atmosphere without mixing due to small-scale turbulent process, 2. accesses more CAPE which leads to

greater mixing than a parcel which is only displaced a small amount. Using the large-scale initial perturbation suppresses the faster-growing small-scale instabilities which equilibrate non-linearly at smaller amplitudes, with less penetration.

In general, the CM1 simulations show that the final state is sensitive to the scale of the initial atmospheric perturbation that triggers convection. The vertical extent within the predicted mixing zone where convection is observed to occur within all six high resolution test cases, varies based on the initial scale of the perturbation. This is difficult to represent within a convection parameterization scheme, because a priori, the scale of the atmospheric perturbation is unknown.

3.4 Non-Condensing Convection Adjustment Scheme

One of the main findings from our CM1 modelling results is that the final atmospheric state, after convective mixing in initially inhomogeneous composition atmospheres, is most generally described by a marginally stable state that is defined by the virtual adiabat. We use this result as the starting point to develop a non-condensing convective adjustment scheme that can account for compositional variation. Our convective adjustment scheme (1) limits convection only to occur within the predicted mixing zone and; (2) adjusts the final atmospheric state to lie on virtual adiabat.

Our convective adjustment scheme uses a CAPE analysis of the initial atmospheric state to determine the region in which convection occurs. We use the same CAPE analysis performed previously to create the blue-green shaded region to determine the bounds in which we expect convection to occur. We set the lower convection bound to match the lower bound of the blue shaded region: the lowest point within the atmosphere from which a parcel can rise to create a positive CAPE. We set the upper bound of the convection region to be the LMA of the maximum CAPE region, which corresponds to the green shaded region in Figs. 3.4–3.9. The upper and lower bounds were chosen to be inclusive of all areas in which

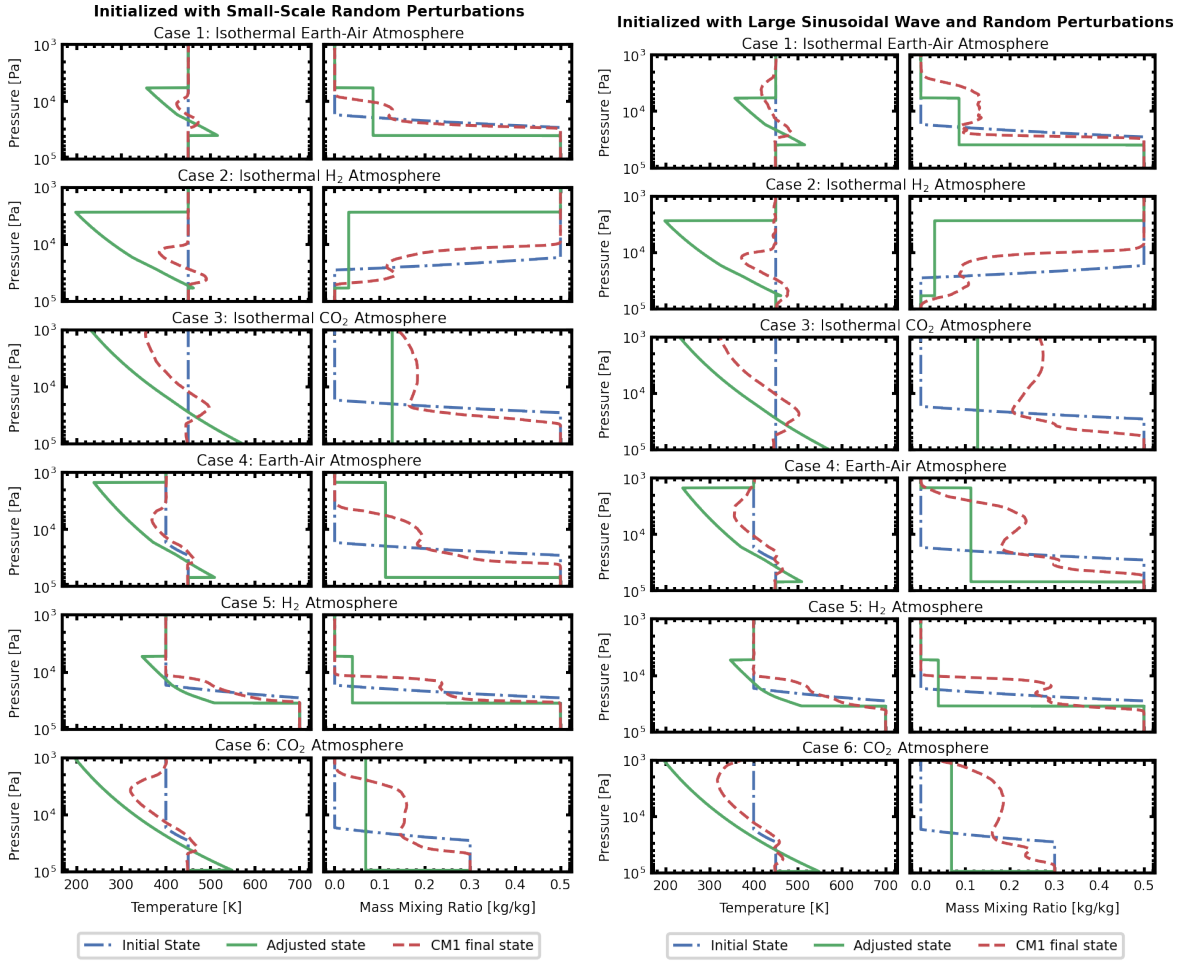

Fig. 3.12 Comparison of the non-condensing convective adjustment scheme to CM1 simulation results for CM1 Cases 1-6. The blue dash-dotted line plots the initial atmospheric state, the red dashed line plots the final atmospheric state from the CM1 simulation, and the green solid line shows the predicted final state using our non-condensing convective adjustment scheme. The left panel shows the comparison of the CM1 results to the convective adjustment scheme for the CM1 simulation run using only random perturbations to trigger convection, while the right panel shows the results when convection is started using random perturbations and a large sinusoidal wave given by Eqn. 3.1. We observe relatively good agreement between the adjustment scheme and CM1 results. A noticeable discrepancy is that the adjustment scheme is unable to represent convective overshoot and has sharp cut-offs for the adjusted atmospheric profile due to using the predicted mixing zone as hard bounds.

convection is observed within our CM1 simulations. This does mean that the mixing layer within the convective adjustment scheme can be larger than what was actually observed in the CM1 simulation results, especially for the simulation test cases that used a small-scale initial perturbation.

The virtual adiabat depends on both the final temperature and mass mixing ratio profiles. There is a whole family of temperature and mass mixing ratio profiles that can create the same virtual adiabat. Therefore, to create a convective adjustment scheme that adjusts the initial atmospheric state to a virtual adiabat, we need to a priori make an assumption regarding either the final state temperature or mass mixing ratio profile. Adjusting to a virtual adiabat is a degenerate problem because T_v is dependent on both T and q_v. For the convective adjustment scheme presented in this work, we make an assumption regarding the final state mass mixing ratio. We assume that the final state mass mixing ratio will uniformly mix within the region where convection occurs, allowing us to adjust the temperature profile to lie on a virtual adiabat. Simply, we take the pressure-weighted mean of the mixing ratio within the predicted mixing zone as determined by the CAPE analysis. This assumption is imperfect and not fully representative of the CM1 simulation results, but it provides an initial framework to incorporate compositional buoyancy effects in convection parameterizations.

It is worth noting that the final state atmospheric profiles are dependent on the initial compositional profile in two ways when assuming q_v homogenizes in the predicted mixing zone. First, the initial mass mixing ratio profile impacts the CAPE analysis used to define the boundaries of convection for our convection parameterization scheme. CAPE is calculated using the $T_v(p)_{\text{initial}}$ profile which is a function of $q_v(p)_{\text{initial}}$ and $T(p)_{\text{initial}}$. Second, since the convective adjustment scheme only homogenizes the final state mass mixing ratio within the predicted mixing zone, any region outside the CAPE analysis will retain its original value from the initial state q_v profile. This approach allows us to be able to create a compositional staircase like structure within the final state and maintain a compositional gradient within

$q_v(p)_{\text{final}}$. The impact of the initial mass mixing ratio profile on the final q_v state is more pronounced when the predicted mixing zone occupies a smaller portion of the vertical domain. However, due to the assumption we make regarding the final q_v profile, our *compositional stairs* will be inaccurate compared to the CM1 simulation results.

Only in the case where the predicted mixing zone encompasses the entire vertical domain does the final state atmospheric profiles become independent of the initial compositional gradient in the convective adjustment scheme. In this particular case, the convection adjustment scheme predicts the final state to be well mixed everywhere, resulting in a fully uniform final q_v profile. The virtual adiabat for a well-mixed atmosphere becomes equivalent to the dry adiabat with the appropriate β_{mix} value for the well mixed atmosphere. In this particular case, the final state profile is solely dependent on the total amount of the initial tracer.

The output for our convective adjustment scheme is shown in Fig. 3.12. We applied our convective adjustment scheme on the same initial atmospheric sounding profiles that we used to run the CM1 test cases 1 – 6. In Fig. 3.12, the left panel shows the temperature and mass mixing ratio for the 6 high resolution test cases explored in this work initialized with small-scale perturbations. The right panel shows q_v and T profiles for all 6 high resolution test cases initialized with the large-scale sinusoidal perturbation. In each plot, the initial atmospheric state is shown by the blue dash-dotted line, the CM1 final state is shown by the red dashed line, and the final state predicted by the convective adjustment scheme is shown by the green solid line. Overall, the convective adjustment scheme is able to match the CM1 outputs decently. The adjustment scheme does predict sharp cut-offs in the vertical profiles due to the hard bound of convection only occurring within the predicted mixing zone from the CAPE analysis. There is some discrepancy between the final state predicted from the adjustment scheme compared to our CM1 outputs that we attribute to our assumption of determining the convection bounds and the q_v of the final adjusted state.

For the simulations that used small initial random perturbations in θ to trigger convection, a better assumption for the upper bound of convection would have been the LNB of the maximum CAPE region (green shaded region), since convection was not observed above this point in those simulations. However, when using a large-scale initial perturbation to trigger convection, we do observe mixing in some simulations between the LNB and LMA for the maximum CAPE region. Since we cannot predict the scale of the initial disturbance that will trigger convection, to be more inclusive, we use the LMA of the maximum CAPE region as the upper bound of the predicted mixing zone for our convective adjustment scheme.

Assuming q_v becomes uniform within the mixing zone is a decent first order approximation. However, this approximation implies that the q_v profile variation within the predicted mixing zone, and multiple steps seen in Case 4 and Case 6 are not captured by the convective adjustment scheme. Additionally, we are not able to match the final q_v value in the mixing zone for Case 2 and Cases 4 - 6. Fig. 3.12 shows that the convection bounds used for these cases are too large compared to the region in which convection was observed within the CM1 simulations. By assuming a homogeneous q_v within the predicted mixing zone, we are susceptible to under-predicting the value of q_v in the convective adjustment scheme. Despite the inaccuracy, the assumption of a well-mixed end state within the mixing zone still captures the key features of the end state temperature profile in most cases. Additionally, our convectively adjustment scheme while energetically consistent and yielding a stable final state, is unable to produce compositional staircases within the predicted mixing zone, account for convective overshoot or penetrative convection. The CM1 simulations highlight these phenomena are important, and future convection parameterization schemes need to address these shortcomings. Our convective adjustment scheme is imperfect, but provides a starting point to represent non-condensing compositional convection in GCMs and is better than ignoring compositional buoyancy altogether for sub-Neptune and super-Earth atmospheres.

3.5 Conclusions

We performed initial value problem simulations of compositional convection within three different planetary atmospheres including an Earth-air, CO_2, and H_2 atmosphere. The high resolution CM1 simulations modeled a convectively unstable initial atmosphere with two initial atmospheric states and two initial perturbations to trigger convection. We also performed two parameter study simulation sets to explore how sensitive the final atmospheric state is to the initial compositional and thermal gradient respectively. The main finding of our CM1 modeling results are:

1. The final atmospheric compositional profile shows the formation of compositional staircases in a large parameter space. The formation of compositional staircases is more frequently observed than convection homogenizing the mass mixing ratio within the entire mixing layer.

2. In the convectively mixed region, the final atmospheric state is a locally marginally stable state, satisfying marginal stability according to the Ledoux criterion.

3. The final atmospheric virtual temperature profile is well approximated by a virtual adiabat in the mixing layer, where we assume β_{mix} is a representative constant for the region mixed by convection. However, the temperature profile itself is sensitive to the presence of compositional staircases remaining in the final state.

4. The CM1 simulations results show sensitivity to large-scale vs small-scale convection triggers. Mixing is observed to occur over a larger extent of the vertical domain for simulations that initially trigger convection using a large-scale perturbation. The predicted mixing zone captures the primary region in which convection occurs, but always overestimates the region in which mixing occurs when convection is triggered using small-scale initial perturbations. The predicted mixing zone was observed to

overestimate the region in which mixing occurred when using the large-scale perturbation for the H_2 atmosphere case, which has strong compositional stabilization of buoyancy.

5. Development of a convective adjustment scheme is challenging because it must be able to account for;

   (a) The formation of compositional staircases in the final q_v profile in many circumstances.

   (b) Sensitivity to large-scale versus small-scale convection triggers

Based on the CM1 simulations, we developed a non-condensing convective adjustment scheme that relaxes an initial atmospheric state to a final state defined by the virtual adiabat. Adjusting to a local, marginally stable state described by the virtual adiabat is a degenerate problem. In order to adjust the final atmospheric state to a virtual adiabat, a priori knowledge or an assumption regarding either the final compositional or temperature profile is required. We compared our convective adjustment scheme to our CM1 simulation outputs and found decent agreement. However, the convective adjustment scheme is currently not able to account for all the observed phenomena from the CM1 simulations. Based on observed features in the CM1 simulation results, future convection parameterization schemes that account for compositional convection should be able to:

1. Predict the compositional staircases in the final mass mixing ratio profile

2. Better represent the bounds of convection (i.e. mixing layer) based on the scale of the initial atmospheric perturbation

3. Account for convective overshoot

4. Account for cases which may have convective penetration.

Future work of modeling compositional convection needs to incorporate the effects of condensation and radiative forcing. We still need to test how expectations from our initial value problem simulations align with statistical equilibrium situations influenced by radiative heating and cooling. Additionally, further work is needed to improve representation of compositional convection in convection parameterization schemes.

The CM1 simulations performed in this work are aimed at improving atmospheric modeling for sub-Neptunes and super-Earths. In particular, the Earth-air and CO_2 atmosphere cases are relevant for terrestrial planets with an ocean in the non-dilute regime, e.g. hot atmospheres which are not steam dominated. The H_2 atmosphere cases are important to better understand sub-Neptune atmospheres, but also planets with a primordial H_2 atmosphere which have recently formed and have not yet lost their primordial atmospheres (Young et al., 2023). There is still a lot of work needed to be done to fully understand these planetary atmospheres and how compositional convection might impact observations of these worlds.

Convection can potentially influence exoplanet observations. Convection could result in significant water vapor injections into the upper atmosphere leading to observable cloud events (see Li and Ingersoll, 2015), or enable observable chemical mixing events by dredging up molecules from the deep atmosphere (see Tsai et al., 2021). Li and Ingersoll (2015) suggested that the giant storm observed in Saturn's atmosphere in 2011 is the outcome of the interior atmosphere heating sufficiently to overcome the compositional convective inhibition caused by water vapor present within Saturn's lower atmosphere. Additionally, Misener and Schlichting (2022) proposed that convective inhibition due to silicate vapors in the H_2 atmospheres of magma ocean worlds can affect the atmospheric structure of these worlds. Misener and Schlichting (2022) argued that the atmospheric layers created by convective inhibition make the planetary radius smaller than it would be if the planet had a purely convective, H_2 atmosphere. To better evaluate the potential impacts of compositional

convection on exoplanet observables, it is essential to first model and comprehend the behavior of convection.

4

Modeling Condensing Compositional Convection for Hydrogen-Dominated Atmospheres

4.1 Summary

The main objective of the work presented in this chapter is to determine the final atmospheric state in H_2-dominated atmospheres while considering the effects of condensing compositional convection. In Chapter 2, we discussed how condensing compositional convection could lead to convective inhibition in H_2-dominated atmospheres. Guillot (1995) proposed that convection could be inhibited when the mass mixing ratio of a condensing tracer exceeds a critical threshold in H_2-dominated atmospheres. Building upon this,

Leconte et al. (2017) argued that the condensation-driven convective inhibition criterion also applies to double-diffusive convection, effectively suggesting that radiation is the predominant mechanism for heat transport in these atmospheres. Leconte et al. (2017) argue that the temperature structure in H_2-dominated atmospheres will have a superadiabatic layer, where the temperature decreases with altitude faster compared to an adiabatic profile. The presence of a radiative, superadiabatic layer implies that the deep internal temperature of H_2-dominated atmospheres is hotter than it would be under a purely convective atmospheric temperature profile.

In this chapter, we use 3D convection permitting simulations to determine the final atmospheric temperature and compositional profile in H_2-dominated atmospheres when condensation-inhibited convective layers form within the atmosphere. We perform convection permitting simulations using Cloud Model 1 (CM1 Bryan, 2009) to model a saturated water vapor tracer in a H_2-dominated atmosphere, allowing for tracer condensation. Unlike the previous chapter, the simulations presented here incorporate the effects of radiation using a gray gas radiation scheme. We have integrated a generalized gray gas radiation scheme to our modified CM1 v20.3 code for modeling convection in a broad planetary context. Our CM1 model development builds upon Lefèvre et al. (2022) and Tan et al. (2021).

We focus on H_2-dominated atmospheres because condensing compositional convection can significantly impact the distribution of tracers and the temperature structure in these atmospheres. Understanding the atmospheric state of planets with H_2-dominated atmospheres allows us to improve our ability to represent convection in global general circulation models and to better interpret observations of these worlds. The simulations presented in this chapter are relevant for any planet with a H_2-dominated atmosphere such as the Solar System's giant planets, sub-Neptune exoplanets like K2 18 b, and planets that have recently formed and still retain a primordial H_2-rich atmosphere (Young et al., 2023).

4.2 Compositional Convection Modeling with CM1

We use Cloud Model 1 (CM1 Bryan, 2009) to perform idealized simulations of condensing compositional convection. CM1 is a non-hydrostatic convection-resolving model that has been extensively used in studying atmospheric flows. A summary of the CM1 code is provided in the Appendix. In this work, we utilize CM1 version 20.3, incorporating the modifications discussed in Chapter 3. These modifications to the original code include (1) setting the thermodynamic constants and planetary parameters using an input file, and (2) revising the buoyancy equation to account for non-dilute concentrations of atmospheric tracers.

Table 4.1 Atmospheric constants used within the CM1 condensing compositional convection simulations

	C_p J/(kg K)	C_v J/(kg K)	R J/(kg K)	$\varepsilon = M_v/M_b$
Hydrogen (Background Atmosphere)	14304.0	10160.0	4144.0	8.94
Water Vapour (Atmospheric tracer)	1870.0	1408.5	461.5	N/A

In this chapter, we model a hydrogen atmosphere with a water vapor atmospheric tracer. The thermodynamic constants used in this study are listed in Table 4.1. We run CM1 using the fully compressible equations in Large-Eddy Simulation (LES) mode. Sub-grid scale turbulent mixing is included using a turbulent kinetic energy closure (Deardorff, 1980) to parameterize mixing at unresolved scales as in (Tan et al., 2021; Lefèvre et al., 2022; Habib and Pierrehumbert, 2023). Additionally, we apply a Rayleigh dampening layer in the top 10 km of the domain to damp out any upward propagating waves.

We use the TWOSTR (Kylling et al., 1995) numerical package to solve the gray gas radiative transfer equations. TWOSTR is a two stream plane-parallel radiative transfer model that uses a gray gas approximation. We assume a constant background opacity of $\kappa_b = 1.18x10^{-4}$ m^2 kg^{-1} and a constant water vapor opacity of $\kappa_v = 0.01$ m^2 kg^{-1} based on

previous studies (Menou, 2011; Freedman et al., 2014; Innes and Pierrehumbert, 2022). The total opacity κ varies as a function of pressure p and is determined by,

$$\kappa(p) = \frac{\kappa_b + \kappa_v * q_v(p)}{1 + q_v}, \tag{4.1}$$

where q_v is the mass mixing ratio of the atmospheric tracer, κ_b and κ_v are the opacity of the background air and atmospheric tracer, respectively. Additionally, we neglect shortwave heating of the upper atmosphere and the effects of scattering. We use a fixed surface temperature as the lower boundary condition, but the atmospheric temperature at the bottom of the column (lowest grid point) can vary over time. We run CM1 with no moisture (evaporative) surface fluxes. The turbulent heat and momentum exchange at the bottom boundary is calculated using the original CM1 formulation. In our modeling setup, the atmosphere is assumed to be transparent to shortwave radiation. Our setup for radiation is simplified, but it allows us to capture the effects of radiation on the temperature profile without the complexity and computational demand of a more realistic radiative transfer scheme. Our CM1 setup represents a sub-Neptune with a deep interior containing water vapor, but without a condensed ocean reservoir at the bottom.

We use the Rotunno and Emanuel (1987) condensation scheme to account for condensation of the water vapor tracer, rainout and evaporation. We only consider the vapor and liquid phase in this work. The Rotunno and Emanuel condensation scheme is included in the source CM1 code. Within this condensation scheme, the mass mixing ratio for the vapor is, $q_v = \frac{\rho_v}{\rho_b}$, and the liquid condensate is $q_l = \frac{\rho_l}{\rho_b}$, where ρ_l is the density of liquid condensate, ρ_b is the background atmosphere density, and ρ_v is the density of the atmospheric tracer in vapor form. Further, in this scheme a distinction is made between *cloud* and *rain* water. Condensate with $q_l \leq 1g\ kg^{-1}$ is cloud condensate and has a terminal fall velocity of V = 0 m s^{-1}, while condensates with $q_l > 1g\ kg^{-1}$ is rain condensate and has a terminal fall velocity of V = 10 m s^{-1}.

Condensation is modeled as a two-step process where first, precipitation occurs *in situ* and second, the condensate is removed by rainout if V > 0. Condensation occurs at a given timestep when $q_v(p) > q_{v,\mathrm{sat}}(p)$ where $q_{v,\mathrm{sat}}(p)$ is the mass mixing ratio if the air parcel at the given (T, p) is fully saturated. In this scheme, condensation occurs to remove excess water vapor relative to saturation such that after condensation $q_v(p) = q_{v,\mathrm{sat}}(p)$. When condensation occurs, a small amount of liquid condensate forms, the vapor pressure of the tracer is adjusted to the saturation vapor pressure, and the latent heat release of condensation causes the local temperature to increase slightly. Condensates can evaporate in a grid cell if $q_v(p) < q_{v,\mathrm{sat}}(p)$ and $q_l > 0$. Evaporation occurs until the condensate is depleted or $q_v(p) = q_{v,\mathrm{sat}}(p)$, depending on which occurs first. When evaporation occurs, the temperature decreases slightly due to the latent heat required to evaporate the liquid, and the vapor pressure of the tracer is again adjusted accordingly. We do not model detailed cloud condensation growth or microphysics. Condensates are assumed to fall out instantaneously and re-evaporated in sub-saturated regions.

We perform two sets of condensing compositional convection simulations in this work. First, we model a saturated isothermal atmosphere. In the saturated isothermal simulations, we anticipate rapid convection to stabilize the system, but our goal is to determine whether the system can evolve to a final atmospheric state that is non-adiabatic. Without compositional effects, isothermal atmospheres are stable to convection. The destabilization of isothermal layers is an important novel feature, particularly since the lower portions of thick atmospheres in pure radiative equilibrium often exhibit isothermal radiative layers. Second, we perform condensing compositional convection simulations which are initialized on adiabatic profiles. Here, we explore if layers of convective inhibition can form and how this impacts stable end-states of the temperature and compositional profile. In particular, we aim to determine if stable superadiabatic layers can form and whether 3D simulations support the atmospheric structure suggested by Leconte et al. (2017). The simulation setup for

the isothermal and adiabatic simulations are described in the following sections respectively and summarized in Table 4.2.

Table 4.2 Initial atmospheric sounding parameters and domain size used for the CM1 condensing compositional convection simulations.

	P_s [Pa]	T_s [K]	$q_{v,s}$ [kg/kg]	q_{crit} [kg/kg]	L_x [km]	L_z [km]	nx	nz	Time [hrs]
Initial Isothermal Simulations									
No Radiation	10^5	273	0.055	0.057	1152	350	192	65	1111
Isothermal $q_v < q_{crit}$	10^5	225	0.001	0.058	1152	750	192	150	3333
Isothermal $q_v \approx q_{crit}$	10^5	273	0.055	0.057	1152	350	192	65	1111
Isothermal $q_v > q_{crit}$	10^5	300	0.321	0.066	1152	150	192	30	2778
Initial Adiabatic Simulations									
Moist Adiabat	$3x10^7$	460	0.30	0.10	1200	750	200	125	2500
Dry then Moist Adiabat	$3x10^7$	850	0.30	0.21	1200	1100	200	125	556

Note, L_x and L_z are the horizontal domain width and vertical domain height respectively. The horizontal domain is a square such that $L_x = L_y$, and the horizontal resolution is the same in the x and y direction. The critical mass mixing ratio value is calculated at the surface using Eqn. 2.37 and the values provided for T_s and $q_{v,s}$. In the isothermal simulations the domain height was set such that the top of the atmosphere is where $q_v = 1$. The "no radiation" case is the isothermal test case where T = 273 K and $q_v = q_{crit}$ but with the radiation scheme turned off in CM1. None of the simulations reach a statistical equilibrium state within their simulation run time.

4.2.1 Isothermal Condensing Compositional Convection Simulations

We performed a set of four isothermal simulations. All simulations were initialized with the assumption that the atmosphere is saturated throughout. Given that the initial temperature is constant across the domain, a saturated isothermal profile implies an increase in the mass mixing ratio of the tracer as pressure decreases. This effect is mathematically represented in Eqn. 2.27. Here, if T is constant, then e_{sat}, which is determined by the Clausius Clapeyron equation, remains constant, and therefore as pressure decreases, $q_{v,sat}$ increases. However, increasing $q_{v,sat}$ indefinitely will cause CM1 to become numerically unstable. Therefore, we

set the top of the atmosphere in these simulations to be at the point where $q_{v,\mathrm{sat}} = 1$. This definition means that the simulation domain height depends on the isothermal temperature we set for the atmosphere.

For all of our saturated isothermal test cases, the initial atmospheric state is unstable to dry compositional convection according to the Ledoux criterion. Atmospheric stability against condensing compositional convection can be determined by considering the Guillot criterion which is reproduced here,

$$(\nabla_{\mathrm{amb}} - \nabla^*_{\mathrm{ad}}) \left(1 - (1 - 1/\epsilon) \left(\frac{q_{v,\mathrm{sat}}}{1 + q_{v,\mathrm{sat}}}\right) \left(\frac{L_v}{R_v T}\right)\right) \leq 0 \tag{2.36}$$

where $\nabla = \frac{d \ln T_x}{d \ln p}$, "amb" represents the atmospheric temperature gradient and the "ad" represents the temperature gradient defined by the moist adiabat. In the case of an isothermal atmosphere, $(\nabla_{\mathrm{amb}} - \nabla^*_{\mathrm{ad}}) < 0$. Therefore, the atmosphere is locally stable against convection when $q_v(p) \leq q_{\mathrm{crit}}$ and unstable by the Guillot criterion when $q_v(p) > q_{\mathrm{crit}}$.

We perform three saturated isothermal test cases where we set the atmospheric temperature such that the surface saturated mass mixing ratio, $q_{v,\mathrm{sat}}(p_s)$, is greater, approximately equal, and less than the critical mass mixing ratio q_{crit} given by Eqn. 2.37. Specifically, we run simulations at T = 225 K, where $q_{v,\mathrm{sat}}(p_s) < q_{\mathrm{crit}}$, T = 273 K where $q_{v,\mathrm{sat}}(p_s) \approx q_{\mathrm{crit}}$ and T = 300 K where $q_{v,\mathrm{sat}}(p_s) > q_{\mathrm{crit}}$. We also run the 273 K test case without radiation as a control test case where the final state is solely representative of condensing compositional convection. In the $q_{v,\mathrm{sat}}(p_s) > q_{\mathrm{crit}}$ simulation, the initial atmospheric state is unstable to condensing compositional convection while in the $q_{v,\mathrm{sat}}(p_s) < q_{\mathrm{crit}}$ the initial atmospheric state is locally stable to condensing compositional convection. We recognize that the temperature values chosen in this work are nonphysical. The initial conditions were chosen to highlight the compositional destabilization and the nature of evolution towards an end state. A better way to achieve the desired regimes would be to change the surface pressure instead, but we present our results as they are now, and will explore this issue in future work. These

calculations can be considered as a preliminary result. The domain size, resolution, and simulation time for the CM1 test cases are given in Table 4.2.

4.2.2 Adiabatic Condensing Compositional Convection Simulations

We performed two adiabatic condensing compositional convection simulations, which were initialized as follows: (1) with the entire atmosphere set to a moist adiabat, and (2) with the lower atmosphere following a dry adiabat with a constant $q_v = 0.3$ kg/kg until the point of saturation, after which the temperature profile transitions to a moist adiabat. With the adiabatic simulations, we are exploring whether superadiabatic layers can form. If the temperature profile is superadiabatic then, $(\nabla_{\rm amb} - \nabla^*_{\rm ad}) > 0$, and convection is completely inhibited when $q_{v,\rm sat}(p) > q_{\rm crit}$. The domain size, resolution, and simulation duration for the CM1 test cases are summarized in Table 4.2.

4.3 CM1 Simulation Results & Discussion

We aim to answer the following questions with our CM1 simulations: Do radiative layers form where convection is inhibited by compositional gradients in H_2-dominated atmospheres? If so, what is the stable atmospheric temperature profile in H_2-dominated atmospheres with compositional gradients?

The isothermal CM1 simulations are used to initialize the system without biasing the end-state after convective mixing to be adiabatic. Isothermal profiles are typically stable to convection. However, in our simulation setup, we have a compositional gradient that is increasing with altitude, meaning that near the top of the domain, the initial state is unstable by the Ledoux criterion to non-condensing convection. In these simulations, convection will begin from near the top of the domain to mix the system to a stable state. Unlike in Chapter 3, we allow for the tracer to condense. As dense fluid from the top of the domain sinks, the air

becomes super-saturated and condensation will occur. We use CM1 simulations to explore how compositional gradients influence convective mixing, the formation of layers where convection is suppressed, and the ways in which radiation can modify the temperature profile.

In the adiabatic simulations, we are directly trying to model whether a superadiabatic region that is stabilized by the compositional gradient can form. The aim of these simulations is to determine if the temperature structure proposed by Leconte et al. (2017) is realized and the timescale this process will take.

In general, we find in all of the simulations performed within this work that the radiative timescales are long. The convection timescale for adjusting the profile is short, as shown by the isothermal initialization cases, but the radiative process is slow. Therefore, none of the simulation results we present in this chapter have truly reached a statistical equilibrium state. In the following discussion, we first review the current results from the isothermal simulations in Section 4.3.1, then present a discussion on the adiabatic simulations in Section 4.3.2. Finally, we discuss the the radiative timescale in Section 4.3.3.

4.3.1 CM1 Results from the Initially Isothermal Simulations

Figs. 4.1-4.4 show the (a) temperature, (b) virtual potential temperature, (c) vapor mass mixing ratio, (d) condensate (liquid water) mixing ratio and (e) relative humidity profiles. In all panels, the blue line shows the initial state of the simulation and the black line shows the final state. No initial state (blue line) is plotted for the condensate mixing ratio as this is zero initially in all simulations. In panel (a), the gray dot-dashed line plots a temperature profile calculated in pure radiative equilibrium, the gray dashed line is the dry adiabat defined by Eqn. 2.14 and the gray solid line plots a moist adiabat defined by Eqn. 2.31. The pure

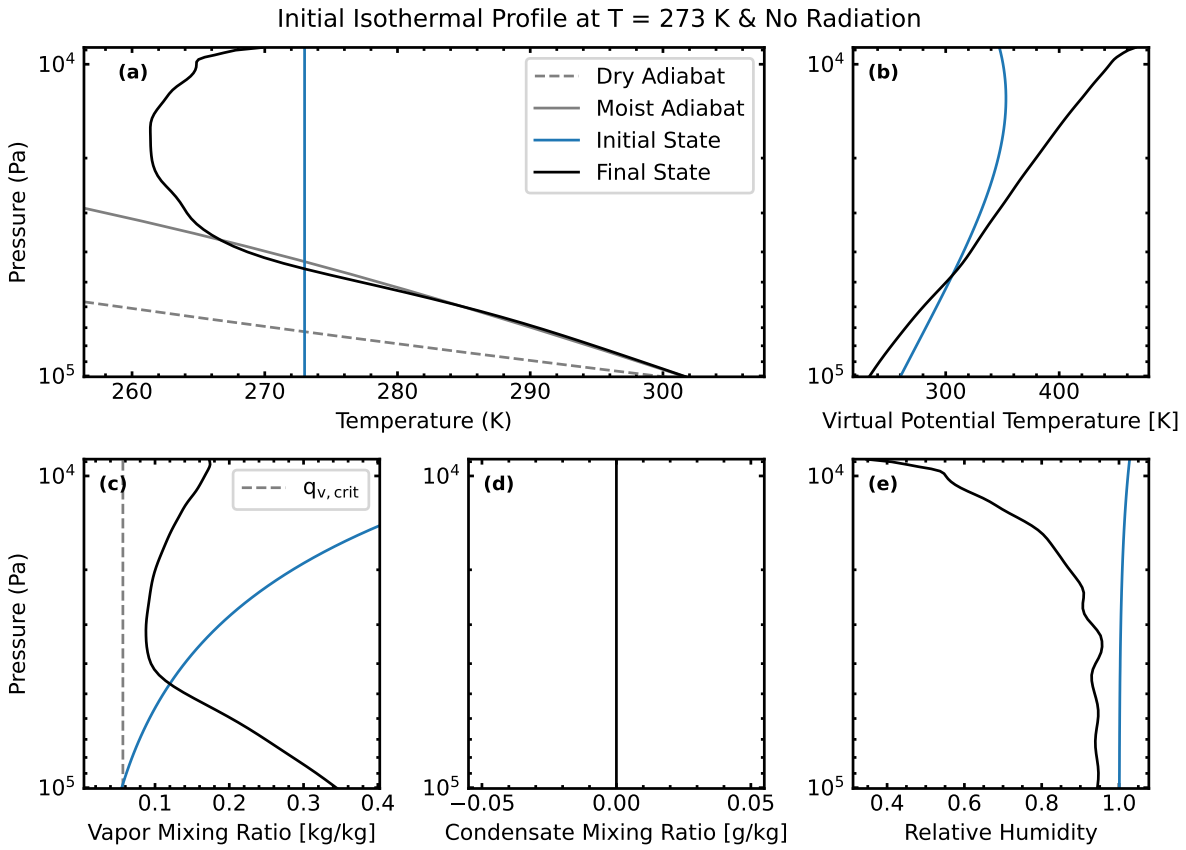

Fig. 4.1 Atmospheric state for the CM1 run without radiation of an initially isothermal atmosphere with $T = 273$ K and $q_{v,s} \approx q_{\text{crit}}$. Profiles of (a) temperature (b) virtual potential temperature (c) vapor mass mixing ratio (d) liquid mass mixing ratio and (e) relative humidity are shown for the final time step of the simulation in black and the initial state in blue. No initial state profile is shown for the condensate mixing ratio, as this was initially zero in all simulations. Note the mass mixing ratio is plotted in units of [kg/kg] while the condensate mixing ratio is plotted in units of [g/kg]. In panel (a), the gray dashed and solid lines plot a dry and moist adiabat from the surface respectively. We do not show a temperature profile in pure radiative equilibrium in this figure because this particular simulation did not include radiation. In panel (c), the dashed gray line shows the critical mass mixing ratio of the initial state.

radiative equilibrium profile is calculated assuming a gray gas atmosphere using,

$$\frac{d\ln T_{\text{RE}}}{d\ln p} = -\frac{1}{4}\frac{1}{(1+\tau_\infty-\tau)}p\frac{d\tau}{dp}, \tag{4.2}$$

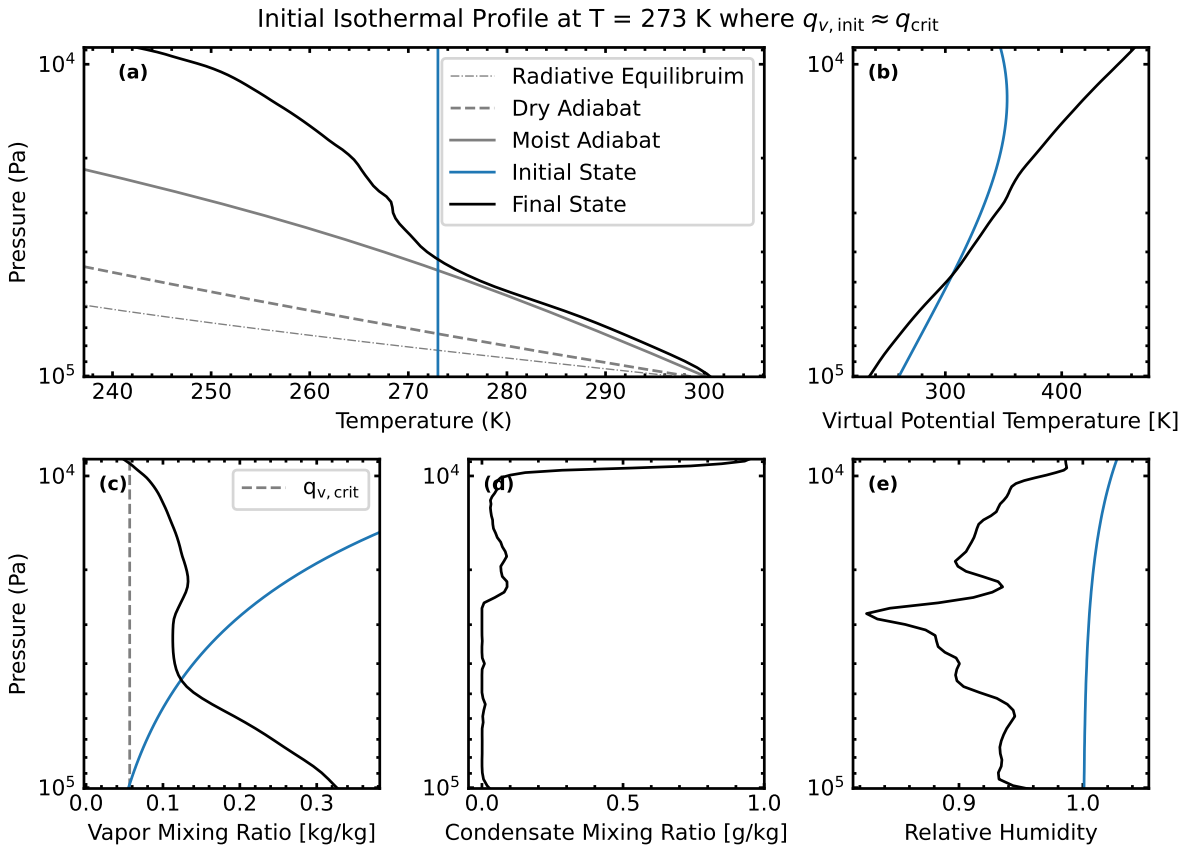

Fig. 4.2 Atmospheric state for the CM1 run of an initially isothermal atmosphere with $T = 273$ K and $q_{v,s} \approx q_{\text{crit}}$ with radiation. Profiles of (a) temperature (b) virtual potential temperature (c) vapor mass mixing ratio (d) liquid mass mixing ratio and (e) relative humidity are shown for the final time step of the simulation in black and the initial state in blue. No initial state profile is shown for the condensate mixing ratio, as this was initially zero in all simulations. Note the mass mixing ratio is plotted in units of [kg/kg] while the condensate mixing ratio is plotted in units of [g/kg]. In panel (a), the gray dashed and solid lines plot a dry and moist adiabat from the surface respectively. The thin gray dot-dashed line plots the temperature profile assuming pure radiative equilibrium in panel (a). In panel (c), the dashed gray line shows the critical mass mixing ratio of the initial state.

where τ is optical depth, and τ_∞ is the total optical depth of the atmosphere (see Chap.4 Pierrehumbert, 2010). The optical depth is related to the atmospheric opacity by $\frac{d\tau}{dp} = -\frac{1}{2g}\kappa(p)$ where the opacity is determined using Eqn. 4.1 with the final state CM1 mass mixing ratio profile. In panel (c) the gray dashed line plots the critical vapor mixing ratio determined by Eqn. 2.37 of the initial atmospheric state. The pressure, temperature, potential temperature, and vapor mixing ratio values are calculated by taking the horizontal average of the CM1

data at the given time step. The virtual potential temperature profile is calculated using Eqn. 2.23 with the horizontally averaged potential temperature and mass mixing ratio profile and assuming a constant β_{mix} determined by the pressure-weighted average of $q_v(p)$. As discussed in Chapter 2 and 3, the effect of choosing different values for β_{mix} is relatively minor. Lastly, the relative humidity is calculated using the 3D temperature, pressure and mass mixing ratio outputs from CM1, and the horizontal average of the relative humidity is plotted.

Figs. 4.1-4.4 show the thermodynamic state from the final time step of the four isothermal simulations. To reiterate, the temperature in these simulations is set such that the initial state $q_{v,\text{sat}}$ at the surface is less than, approximately equal to, or greater than the initial state q_{crit} at the surface. In all four of the isothermal CM1 test cases, the initial atmosphere is unstable near the top of the domain, which can be seen by θ_v decreasing in the upper atmosphere. The region where θ_v is decreasing represents the part of the domain that is initially unstable to the Ledoux criterion. The depth of the initially Ledoux unstable region in the upper atmosphere varies with the temperature, where higher temperature simulations show a deeper Ledoux unstable region. At higher temperatures, the air can hold more water vapor at saturation for the same pressure. As a result, a saturated isothermal atmosphere at a higher temperature will transition into a Ledoux unstable region faster compared to a saturated isothermal case initialized at a lower temperature. The Ledoux unstable region is confined to low pressures in the 225 K isothermal test case while in the 300 K test case, the Ledoux unstable region is nearly half of the vertical domain. The final state virtual potential temperature profile suggests that after convective mixing occurred, the atmospheric state is stable for all of the isothermal CM1 simulations.

First consider the isothermal test cases where the initial state $T(p)$ = 273 K and the surface $q_{v,\text{sat}} \approx q_{\text{crit}}$. Fig. 4.1 shows the atmospheric state without the effects of radiation, whereas Fig. 4.2 shows the atmospheric state while considering radiation. We note that

the final atmospheric $q_v(p)$ is similar in both cases. A key difference between the two simulations is the cloud condensate profile and the upper atmospheric temperature profile. In Fig. 4.1, when there are no radiative effects, the temperature follows a moist adiabat from the surface up until a point in the upper atmosphere where the temperature starts to increase. The region of the atmosphere described by the moist adiabat corresponds to a relative humidity near saturation. In the upper part of the atmosphere, the relative humidity shows the atmosphere is sub-saturated. The upper atmospheric temperature trend is due to compositionally dense air cooling the atmosphere (relative to the initial state) as it sinks adiabatically. The temperature profile's shape in the upper atmosphere is similar to the observed shape of the temperature profile in the non-condensing compositional convection simulations discussed in Chapter 3. This suggests that after initial non-condensing convection in the upper atmosphere, the temperature profile in this region remains unchanged in the simulations without radiation. Whereas, in the deep atmosphere, the temperature profile is given by a moist adaibat because as compositionally dense air sinks, lower atmospheric layers become super-saturated leading condensation to occur which drives moist convection in the deep atmosphere. Further, we find that in the final state, there are no observed clouds or liquid condensate within the entire domain.

Conversely, Fig. 4.2 shows radiation cools the upper atmospheric temperature profile and drives condensation. In Fig. 4.2 we see the formation of a cloud in the upper atmosphere where radiative cooling is driving condensation. Additionally, when we include the effects of radiation, we find that the atmospheric temperature profile can be described by a moist adiabat in the lower atmosphere, but the upper atmosphere is affected by radiation in the $q_{v,\mathrm{sat}} \approx q_{\mathrm{crit}}$ test case with radiation. In the region where the temperature profile is affected by radiation, we observe a cloud deck form. Note, the relative humidity in $q_{v,\mathrm{sat}} \approx q_{\mathrm{crit}}$ case with radiation remains near saturation within the entire domain.

Fig. 4.5 shows cross-sections of the vertical velocity taken in the middle of the y-domain for all four isothermal simulations at five different time steps throughout the simulation. The vertical velocity cross-sections of the $q_{v,s} \approx q_{\text{crit}}$ case without radiation (top-most row) show that after the initial convective mixing a stable atmospheric state is reached and there is no more mixing or convection that occurs afterwards. Conversely, in the $q_{v,s} \approx q_{\text{crit}}$ case with radiation (second row), the vertical velocity shows weak mixing and rainout of condensates.

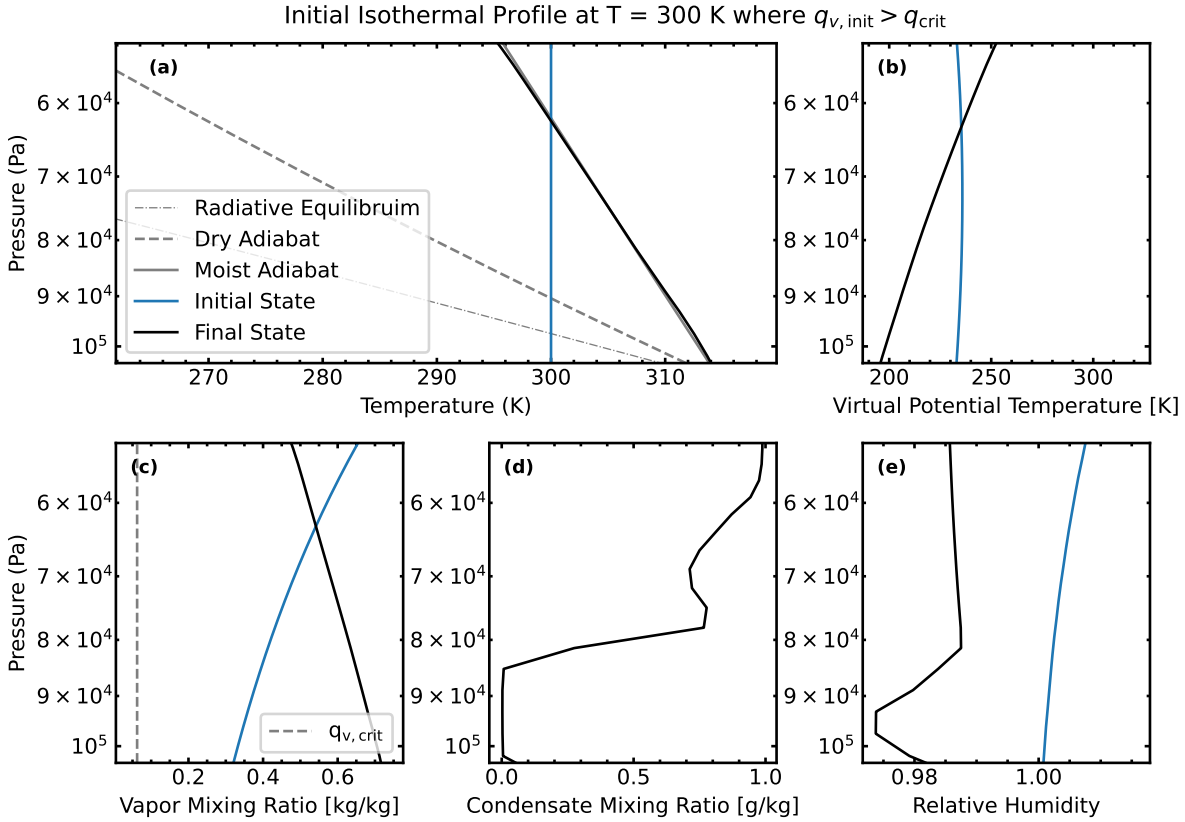

Fig. 4.3 Same as Fig. 4.2 but showing the atmospheric state for the CM1 run of an initially isothermal atmosphere with $T = 300$ K and $q_{v,s} > q_{\text{crit}}$.

In the CM1 simulation initialized with an isothermal profile at $T = 300$ K, where $q_{v,s} > q_{\text{crit}}$, we observe that the final atmospheric temperature profile aligns with a moist adiabat and the whole domain is near saturation. Notably, after the initial convective mixing, we do not observe the formation of any radiative layers in the atmospheric temperature profile. After the initial convective mixing, $q_{\text{v,final}}(p) > q_{\text{crit,final}}$ throughout the domain meaning

that the final state of the entire domain is stable against convection by the Guillot criterion. Additionally, the vertical velocity cross-sections for the $q_{v,s} > q_{\text{crit}}$ case, shown in the third row of Fig. 4.5, suggest that after a convectively stable state is reached the only contribution to the vertical velocity is due to precipitation and falling condensates.

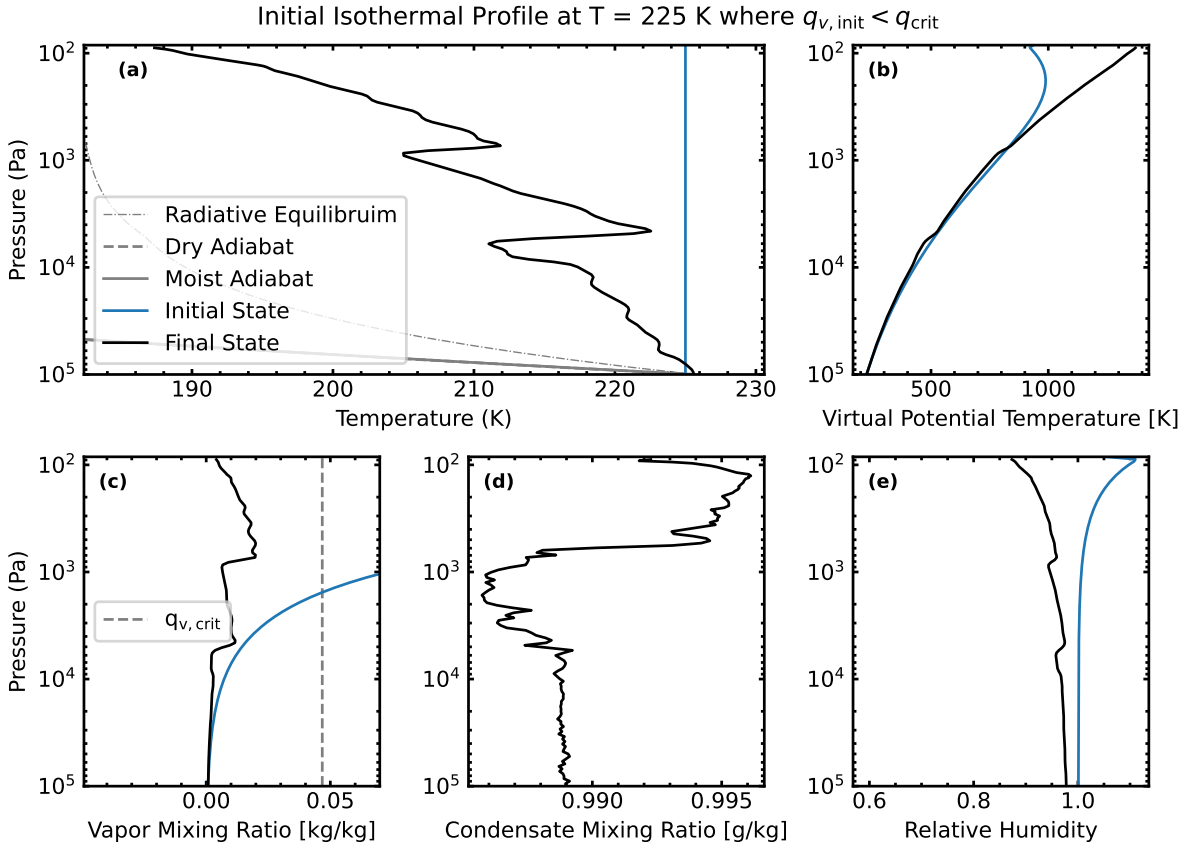

Fig. 4.4 Same as Fig. 4.2 but showing the atmospheric state for the CM1 run of an initially isothermal atmosphere with $T = 225$ K and $q_{v,s} < q_{\text{crit}}$. Note, in this case, the dry and moist adiabat are nearly identical.

In the final isothermal CM1 test case, which is initialized such that $T = 225$ K and $q_{v,s} < q_{\text{crit}}$ as shown in Fig. 4.4, we observe the formation of compositional staircases. Note, we expect this case to be similar to the non-condensing cases presented in the previous chapter due to the low temperature. In the final atmospheric state, $q_v(p)$ is now less than q_{crit}. The temperature profile also exhibits a staircase-like behavior, mirroring the compositional profile. In this simulation, non-condensing convection rapidly mixed the atmosphere to a

stable state, leading to the formation of the compositional staircases. Subsequent radiative cooling steepened the temperature profile, and led to condensation within the domain. The formation of distinct layers in the temperature profile may be attributed to variations in the local radiative cooling rates. The final atmospheric state for the $q_{v,s} < q_{\text{crit}}$ CM1 case is stable and can be observed by $\theta_v(p)$ increasing with height. The vertical velocity cross-sections for the $q_{v,s} < q_{\text{crit}}$ case, shown in the bottom row of Fig. 4.5, show initial condensation in the upper atmosphere, but at later times no convection is observed. In this case, the final atmospheric state is stable by the Ledoux criterion and further convective mixing is not expected.

In general, the isothermal simulations show that an isothermal atmospheric state can be destabilized by a compositional gradient. The simulations do not show the formation of superadiabatic layers, but rather suggest that rapid convection occurs to mix the atmosphere to a stable state. Radiative cooling in the upper atmosphere drives condensation and cloud formation in the simulations. However, the isothermal simulations with radiation have not reached a statistical equilibrium state. The radiative relaxation timescale is discussed in Section 4.3.3.

4.3.2 CM1 Results from the Initially Adiabatic Simulations

Fig. 4.6 and Fig. 4.7 show cross-sections in (x,z) taken in the middle of the y-domain at five different time steps throughout the CM1 simulation of vertical velocity in [m/s] and the condensate mixing ratio in [g/kg]. Fig. 4.6 shows the cross-sections for the adiabatic simulation initialized on the moist adiabat, while Fig. 4.7 shows vertical velocity and condensate mixing ratio cross-sections for the adiabatic simulation initialized on the dry then moist adiabat. In both test cases, we see the formation of a distinct layer where convection is entirely inhibited and the vertical velocities are zero. Additionally, in both cases, we observe the formation of a cloud deck that corresponds to a layer of moist convection in the upper atmosphere.

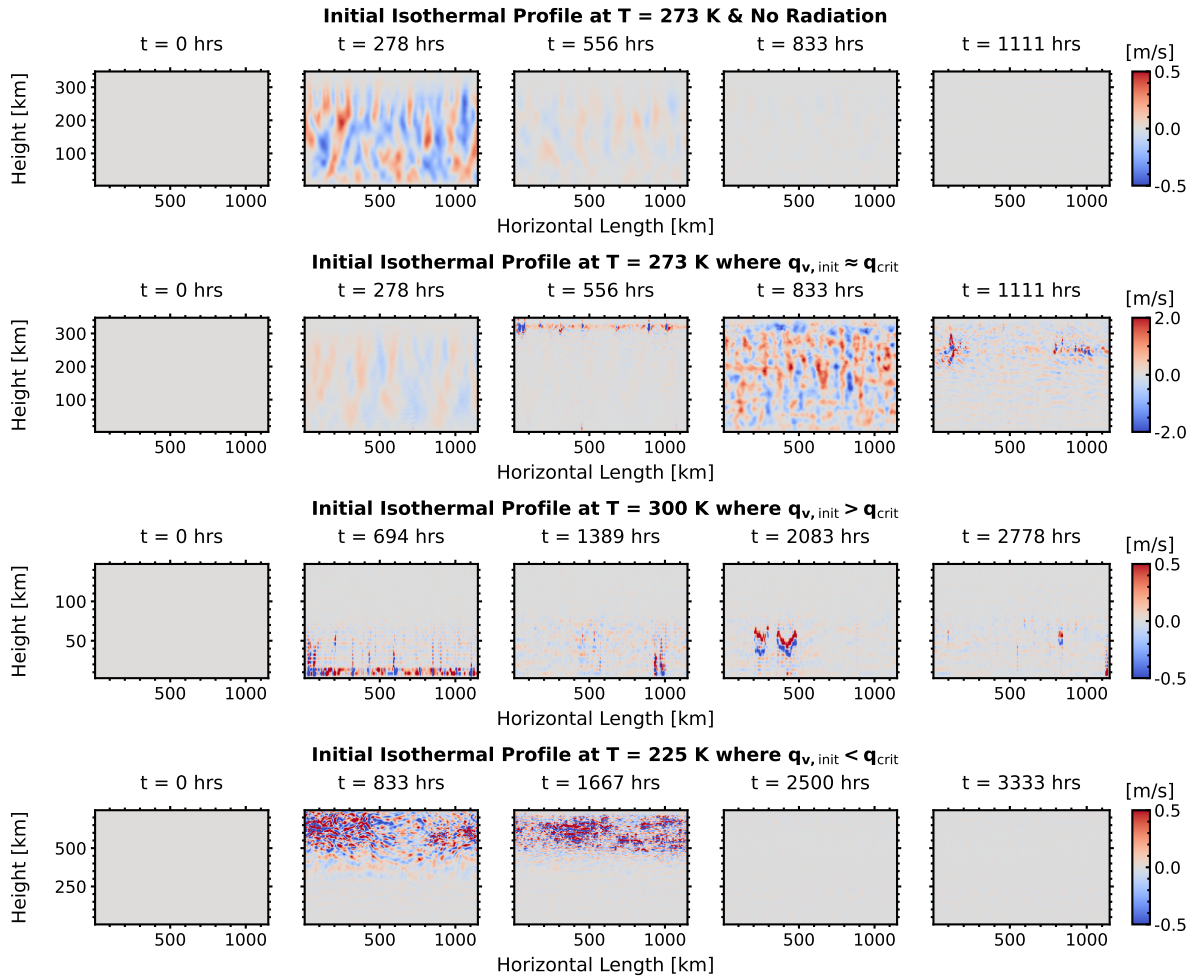

Fig. 4.5 Vertical velocity cross-sections in (x,z) taken in the middle of the y-domain, of the isothermal CM1 simulations. Each panel shows the vertical velocity cross-section at various times throughout the CM1 simulation. The vertical velocity suggests that rapid convection occurs initially to adjust the system to a stable state. Afterwards, no convective mixing is observed and the vertical velocity is primarily due to falling condensates. Condensation is driven by radiative cooling of the upper atmosphere.

In Fig. 4.7 we also observe a layer near the surface of dry convection since the lower part of the atmosphere was initialized on a dry adiabat. In the convectively inhibited region, condensates with $q_l > 1$ g kg^{-1} are observed to fall through and re-evaporate in this region.

Figs. 4.8 and Fig. 4.9 show the atmospheric state from the initial and final time step of the CM1 simulations. In Figs. 4.8 and 4.9, the black solid line indicates the final state and the blue solid line shows the initial state of the simulation. Figs. 4.8 and 4.9 plot the

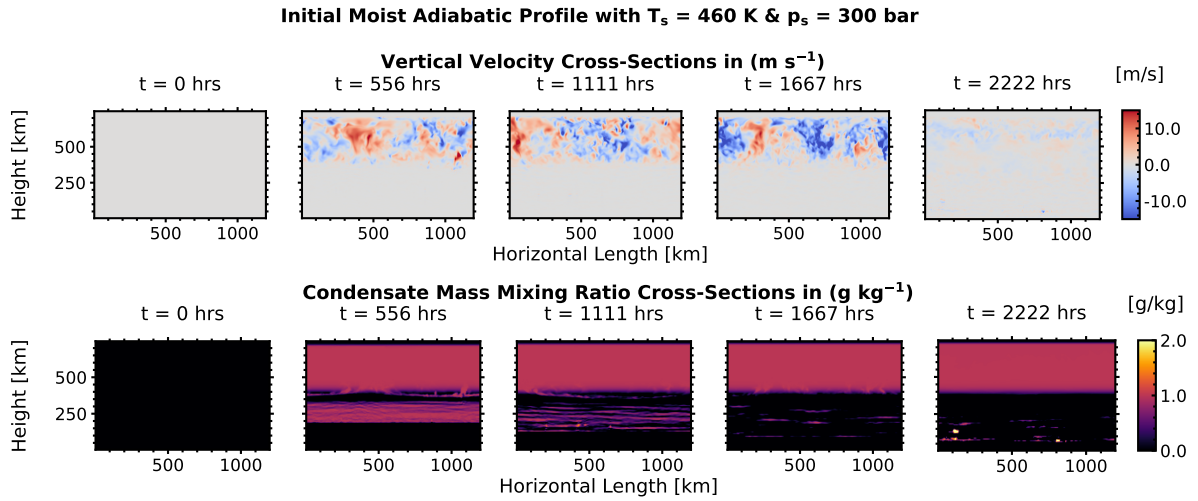

Fig. 4.6 Vertical velocity and condensate cross-sections in (x,z) taken in the middle of the y-domain from adiabatic simulation initialized on the moist adiabat. The top row shows the vertical velocity in [m/s] at different times throughout the CM1 simulation. The bottom row shows the condensate mixing ratio in [g/kg] at different times throughout the CM1 simulation. The cross-sections show that a moist convective region is present in the upper atmosphere, but convection is completely inhibited in the lower atmosphere where the vertical velocities are nearly zero. A thick cloud layer forms in the upper atmosphere in the region of moist convection, while rain condensates fall through and re-evaporate in the convectively inhibited region.

horizontally averaged profiles for (a) temperature, (b) temperature difference ($T_{\text{final}} - T_{\text{initial}}$), (c) virtual potential temperature, (d) vapor mass mixing ratio, (e) condensate mass mixing ratio, and (f) relative humidity. As previously, $T(p)$, $\theta(p)$, $q_v(p)$, $q_l(p)$ are determined by taking the horizontal average of the 3D CM1 output at the given timestep. The relative humidity is calculated using the 3D CM1 output for T and q_v and the horizontal average of the relative humidity is plotted. θ_v is calculated using the horizontally averaged θ and q_v profiles assuming a constant β_{mix} as before. As previously, panel (a) shows the moist adiabat calculated using Eqn. 2.31 as the gray solid line, the dry adiabat calculated using Eqn. 2.14 as the gray dashed line, and the pure radiative equilibrium calculated using Eqn. 4.2 as the gray dot-dashed line. In panel (c), the gray dashed line shows the critical mixing ratio calculated using Eqn. 2.37. In panel (a), the CM1 temperature profiles cover the moist adiabat. Initially, the CM1 simulations have no condensates and $q_l(p) = 0$.

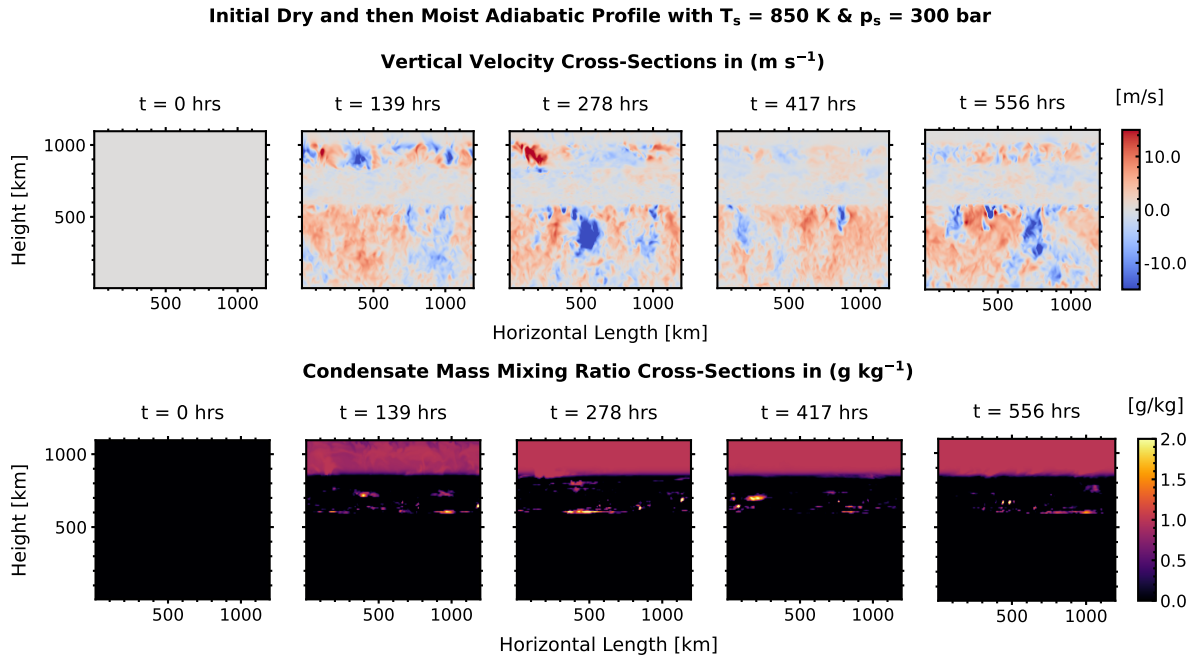

Fig. 4.7 Vertical velocity and condensate cross-sections in (x,z) taken in the middle of the y-domain from adiabatic simulation initialized on the dry adiabat to the level of saturation from which point the initial state followed a moist adiabat. The top row shows the vertical velocity in [m/s] at different times throughout the CM1 simulation. The bottom row shows the condensate mixing ratio in [g/kg] at different times throughout the CM1 simulation. The vertical velocity cross-sections shows 3 distinct layers; a dry convective region near the surface, a layer where convection is completely inhibited and velocities are nearly zero, and a layer of moist convection in the upper atmosphere. The corresponding condensate mixing ratio plots show a cloud deck from in the moist convection layer and we observe condensates falling through and re-evaporating in the region where convection is completely inhibited.

A key distinction in the adiabatic simulations, compared to the isothermal CM1 simulations, is that the initial state in the adiabatic simulations is stable against convection. In our simulation setup, $q_v > q_{\text{crit}}$ in a significant portion of the domain in the two adiabatic simulations, indicating that convection should be inhibited according to the Guillot criterion. The vertical velocity cross-sections do show a layer of convective inhibition. However, the simulation results show minimal change in atmospheric temperature between the initial and final states. The final state temperature profile does not evolve into a steep radiative layer. However, the temperature difference, shown in panel (b), does show that the temperature gradient is steepening, though it is nowhere near having reached equilibrium yet. The deep

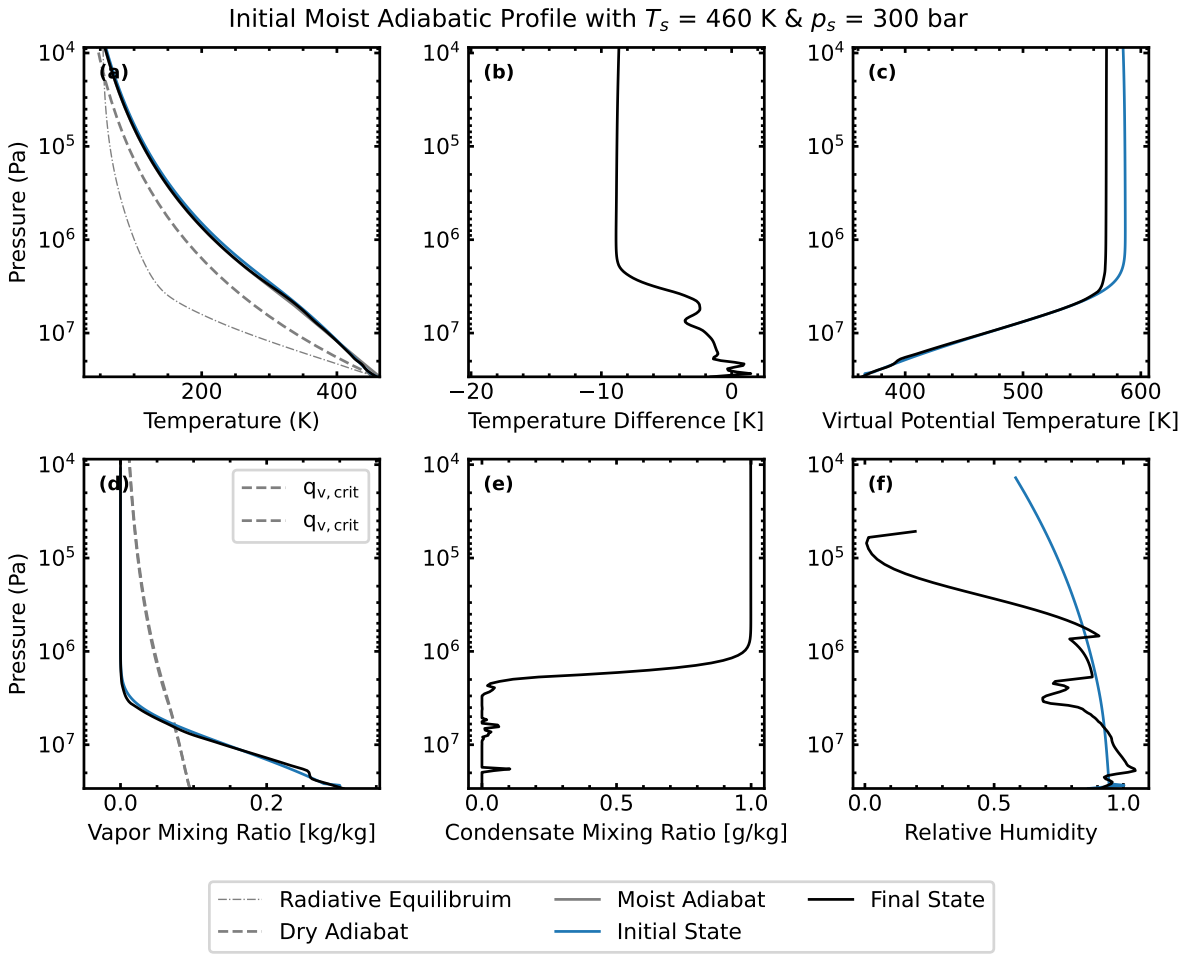

Fig. 4.8 Atmospheric state for CM1 simulation of an initially moist adiabatic atmosphere with $T_s = 460$ K, $p_s = 300$ bar and $q_{v,s} > q_{\text{crit}}$. Profiles of (a) temperature (b) virtual potential temperature (c) vapor mass mixing ratio (d) liquid mass mixing ratio and (e) relative humidity are shown for the final time step of the simulation in black and the initial state in blue. In panel (a), the gray dashed and solid lines plot a dry and moist adiabat from the surface respectively. The gray dot-dashed line plots the temperature profile assuming gray gas pure radiative equilibrium. In panel (c), the dashed gray line shows the critical mass mixing ratio.

atmosphere in the adiabatic simulation, initialized on the dry then moist adiabat shown in Fig. 4.9, is nearly in radiative equilibrium which is expected for regions with constant opacity and no pressure broadening. In the case of the dry then moist adiabat, the deep atmosphere is situated in a region of dry convection where both the mass mixing ratio and opacity are constant.

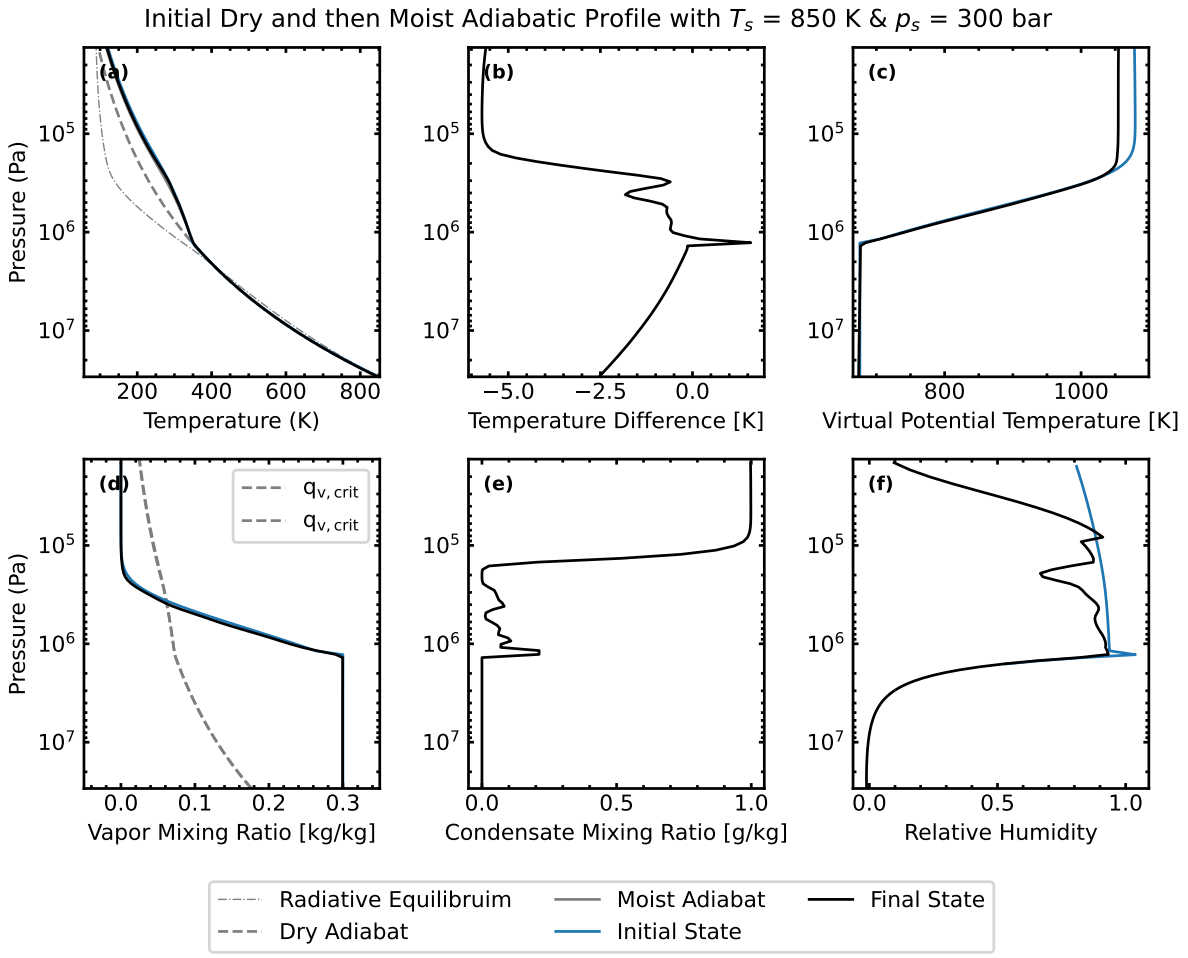

Fig. 4.9 Atmospheric state for the CM1 simulation of an initial state defined by a dry adiabat from the surface until the lifted condensation level, and then a moist adiabat to the top of the atmosphere. The profile is initialized with T_s = 850 K, p_s = 300 bar and $q_{v,s} > q_{\text{crit}}$. Profiles of (a) temperature (b) virtual potential temperature (c) vapor mass mixing ratio (d) liquid mass mixing ratio and (e) relative humidity are shown for the final time step of the simulation in black and the initial state in blue. In panel (a), the gray dashed and solid lines plot a dry and moist adiabats. The gray dot-dashed line plots the temperature profile assuming gray gas pure radiative equilibrium. In panel (c), the dashed gray line shows the critical mass mixing ratio.

The deviations observed in the θ_v and q_v profiles are due to condensation. Similar to the isothermal cases, we find that cooling in the upper atmosphere drives condensation. In Fig. 4.9, we maintain the dry convection layer from the initial state. Within the convectively inhibited layer, the atmosphere remains close to saturation but does not have a cloud deck.

We observe a decrease in relative humidity in the upper atmosphere where moist convection occurs, which we believe is due to numerical effects in CM1. In the upper atmospheric regions, the temperatures drop below 200 K. Thus, the saturation vapor pressure at these temperatures is very small and consequently the amount of tracer needed to be fully saturated is also small. We think numerical round-off errors in the condensation scheme are affecting the condensate and vapor mass mixing ratio CM1 output in the upper atmosphere. It is likely that the source of the condensate cloud deck in the upper atmosphere is spurious. If the atmosphere is truly sub-saturated, the condensate should evaporate. Inconsistencies in the condensation scheme at low temperature will be addressed in near-term future work.

The adiabatic simulations show compositional effects suppress convection and the temperature profile exhibits a slight steepening. Despite the clear formation of the convective inhibition layer, we do not observe the temperature profile to adjust to a steep radiative profile. Our simulations indicate that the timescale for convection to adjust the atmospheric state profile is relatively fast, as shown by the isothermal initialization cases. However, the radiative processes are slow. Since the simulations confirm that convection is inhibited, radiative relaxation should eventually proceed to produce steep radiative layers. We argue in the next section that the relaxation time is too long for steep radiative layers to form in the span of CM1 simulations.

4.3.3 Evaluating CM1 Radiative Timescales & Convergence

We show an overview of the radiation fluxes and temperature tendency calculated by the TWOSTR numerical package in CM1 for the isothermal simulations in Fig. 4.10 and the adiabatic simulations in Fig. 4.11. In panel (a), we plot the difference of the upward and downward longwave infrared flux, $I_+ - I_-$, and in panel (b) we show the temperature ten-

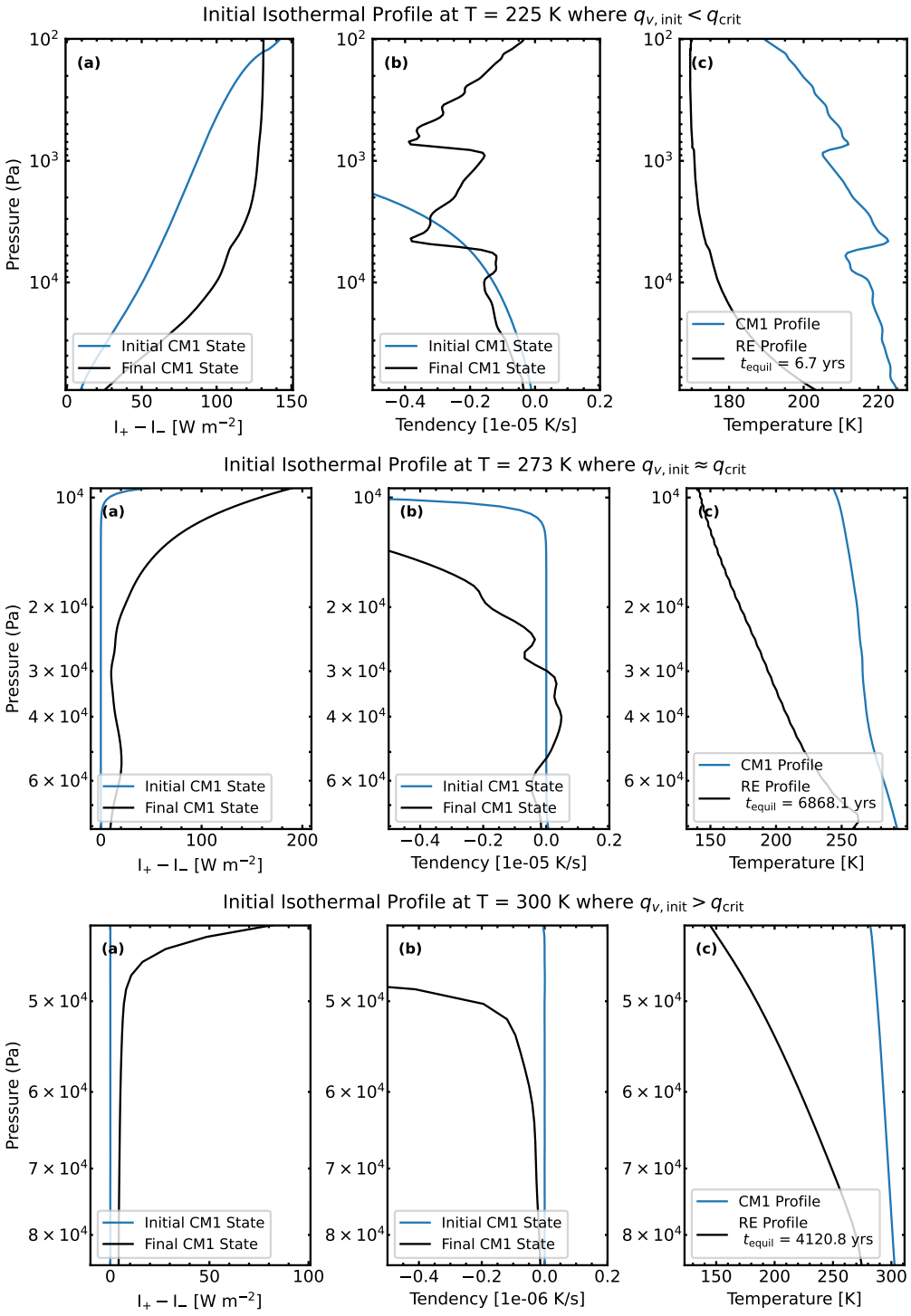

Fig. 4.10 Radiative fluxes for the initially isothermal compositional convection CM1 simulations. Panel (a) shows the difference of the upward and downward longwave infrared flux, $I_+ - I_-$ and panel (b) shows the temperature tendency, $\frac{dT}{dt}$, calculated by the TWOSTR numerical package in CM1. Panel (c) plots the final state CM1 profile in blue and the temperature profile if the CM1 final state is forced to radiative equilibrium (RE) in black. The calculated radiative equilibrium profile provides an indication of the radiative relaxation timescale.

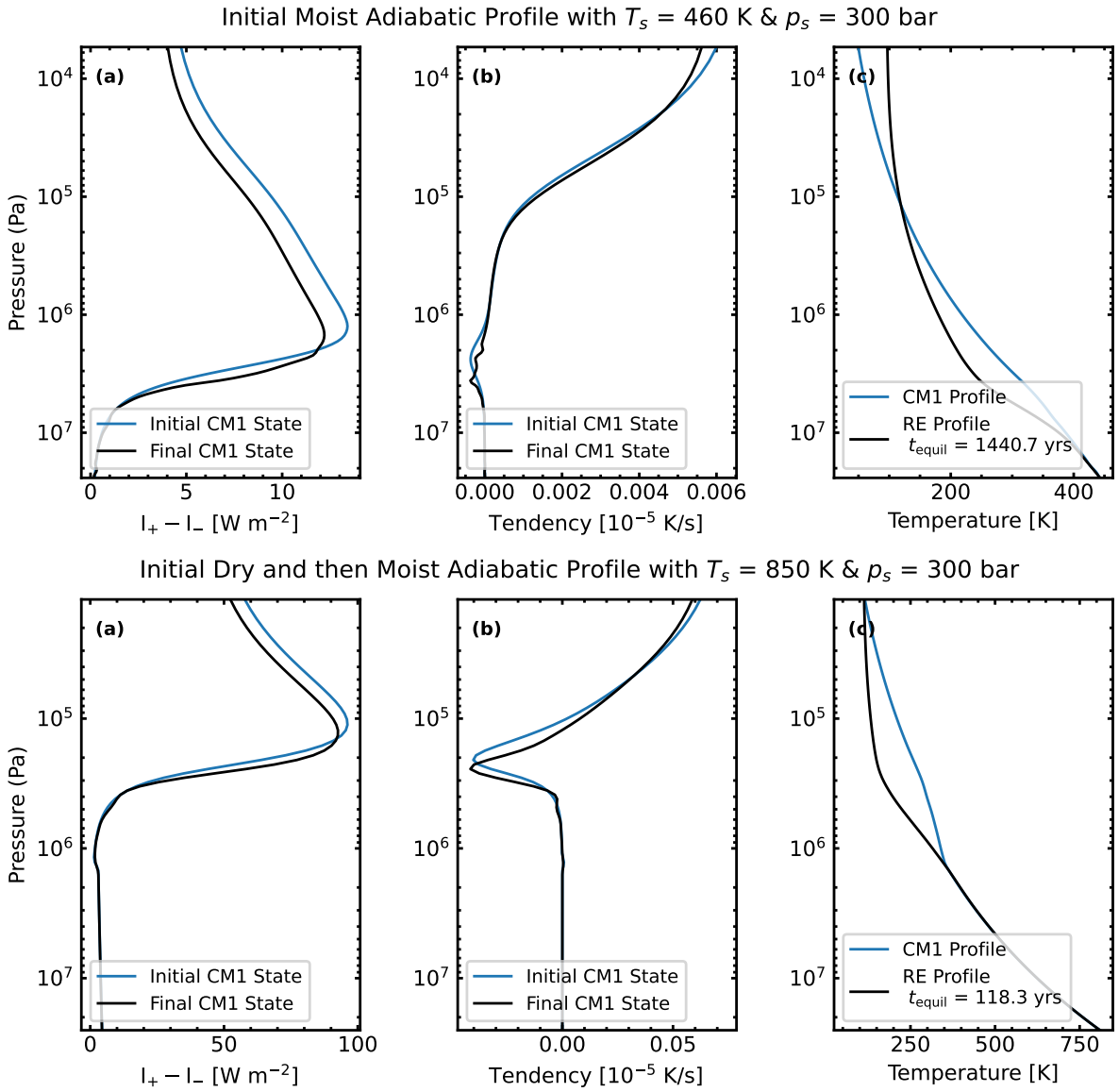

Fig. 4.11 CM1 Radiative fluxes and estimated radiative timescale for initially adiabatic condensing compositional convection simulations. Panel (a) shows the difference of the upward and downward longwave infrared flux, $I_+ - I_-$ and panel (b) shows the temperature tendency, $\frac{dT}{dt}$, calculated by the TWOSTR numerical package in CM1. Panel (c) plots the final state CM1 profile in blue and the temperature profile if the CM1 final state is forced to radiative equilibrium (RE) in black. The calculated radiative equilibrium profile provides an indication of the radiative relaxation timescale and the temperature for the layer where convection is inhibited. Our current estimates show that CM1 would need an additional 1441 years to reach radiative equilibrium in the simulation initialized on a moist adiabat, and 118 years to reach radiative equilibrium for the simulation initialized on a dry then moist adiabat.

dency, $\frac{dT}{dt}$. The temperature tendency is defined,

$$\frac{dT}{dt} = \frac{g}{C_{p,\text{mix}}(p)} \frac{d(I_+ - I_-)}{dp}, \tag{4.3}$$

where g is the gravitational acceleration, $C_{p,\text{mix}}$ is the heat capacity at a given pressure given by Eqn. 2.10. We find in our CM1 simulations that the temperature tendency is on the order of $10^{-5} - 10^{-8}$ $K\ s^{-1}$, suggesting that the radiative relaxation timescale is quite long in all of our simulations. If we consider the adiabatic test case initialized on the moist adiabat, and pick a point near the top of the atmosphere where $\frac{dT}{dt} = 5x10^{-8}$ K/s, the temperature tendency suggests that it would take $2x10^7$ seconds or 6000 hours for the temperature to change by 1 K at that point.

To more accurately quantify the radiative relaxation time, we utilized the final output profile from CM1 to estimate the time required to reach radiative equilibrium and to determine the corresponding temperature profile assuming convection is inhibited everywhere. In panel (c) of Fig. 4.11, we plot the final temperature state from CM1 in blue, alongside the temperature profile that would result if the system were forced into radiative equilibrium, meaning $I_+ - I_-$ is constant with height. To determine the temperature profile in radiative equilibrium, we started with the final CM1 profile and calculated the upward and downward radiative fluxes and temperature tendency using the gray gas Schwarzschild equations. We then heat or cool the CM1 profile by,

$$T(p, t+1) = T(p, t) + \frac{dT}{dt} \cdot dt, \tag{4.4}$$

where $T(p, t+1)$ is the new temperature profile, $\frac{dT}{dt}$ is the calculated temperature tendency, and dt is the time step. The new temperature profile is used to update the temperature tendency using the gray gas radiative transfer equations. We iterated this calculation until

the heating rate, $\frac{dT}{dt}$, became two orders of magnitude smaller than the heating rate of the initial state.

This calculation offers a method to estimate the radiative relaxation time and provides a prediction of the temperature profile in pure radiative equilibrium. This method assumes that the entire atmosphere is no longer convective and neglects the interaction of convective regions with the inhibited region. Therefore, this calculation should be viewed as an indication of how long it would take the inhibited regions to reach equilibrium. Using this method, we find that the adiabatic simulation initialized on the moist adiabat, would require 1441 years to reach radiative equilibrium, while CM1 simulation initialized on the dry then moist adiabat would need 118 years. Additionally, the temperature tendency output from CM1, as shown in panel (b), suggests radiative heating in the upper atmospheric layers. However, the temperature difference plots in Fig.4.9 and Fig.4.8 indicate cooling. It is possible that dynamical effects are causing cooling at the upper levels, with radiation serving to slowing this cooling process.

For the isothermal simulations, the initial state temperature tendency (blue line in panel b) is essentially zero, except near the the top of the atmosphere. This is expected for isothermal atmospheres, and as the temperature gradients develop, the cooling rate increases. Our radiative equilibrium calculation suggests that the isothermal simulations would need 6.7 yrs, 6868 yrs, and 4121 yrs to reach a radiative equilibrium for the test cases initialized with $q_{v,s}$ less than, approximately equal to, and greater than q_{crit}, respectively.

Fig. 4.11 and Fig. 4.10 demonstrates that the CM1 simulation results have not yet achieved a state of statistical equilibrium, and that radiation still has the potential to modify the temperature profile, albeit over an extremely long timescales. The CM1 adiabatic simulations indicate the formation of convectively inhibited layers. However, due to the radiative relaxation time, we have not been able to extensively follow the process in CM1, particularly in

the development of radiative layers. Therefore, we cannot definitively conclude whether any process would counteract the anticipated radiative steepening.

4.4 Conclusions

In this Chapter, we have performed CM1 simulations of condensing compositional convection in H_2-dominated atmospheres. We performed two sets of simulations, first we consider simulations initialized on a saturated isothermal state and second we consider CM1 simulations which are initialized on an adiabat. The isothermal simulations show that an isothermal temperature profile can be destabilized due to a compositional gradient. We see rapid initial convection in these simulations that adjusts the atmospheric state to a stable state defined by radiation when $q_v(p) < q_{\rm crit}$ and moist convection when $q_v(p) > q_{\rm crit}$.

In the adiabatic CM1 simulations, the initial atmospheric state is convectively stable, but we see the formation of a distinct layer where convection is inhibited in the 2D vertical velocity cross-sections where the atmosphere is saturated and $q_v(p) > q_{\rm crit}$. Even though we find that an atmospheric layer forms where convection is inhibited, the temperature change during the duration of the CM1 simulation is slight but does suggest a tendency towards steepening in excess of the adiabatic slope. Due to the of long radiative relaxation times, the system has not proceeded far towards radiative equilibrium in CM1. Instead, we find through a simplified calculation that the radiative relaxation timescale of our simulations is long. To determine if the saturated, steep radiative layers are stable to the Guillot criterion, we should initialize a CM1 simulation in this state and determine if the simulation remains stable to convection. The simulations presented in this chapter shows that radiative-convective simulations with long radiative timescales require more thoughts in order to reach a steady state. Lastly, we do observe condensate falling and re-evaporating in the convectively inhibited layer, suggesting that condensation could be a mechanism for transporting heat in

convectively inhibited layers. This hypothesis still needs to be tested and verified through a comparison of the energy balance in the atmosphere.

5

Summary and Future Work

In this thesis, we presented convection theory and 3D simulations of compositional convection, using the Cloud Model 1 (CM1). Chapter 2 focused on compositional convection theory and stability criteria. We discussed how compositional gradients affect the definition of potential temperature and the non-condensing adiabatic temperature profile. A key concept we introduced in Chapter 2 is the definition of the virtual dry adiabat, which describes the temperature-pressure profile of an air parcel as it is displaced in an atmosphere with an inhomogeneous compositional gradient. We concluded Chapter 2 with a review of the stability criterion for condensing compositional convection.

Chapter 3 presented 3D CM1 simulations of non-condensing compositional convection in high mean molecular weight and hydrogen-dominated atmospheres. Our non-

condensing simulations showed that convection mixed the atmosphere to a final state dependent on both the compositional and temperature profile. Notably, our results indicated that compositional gradients could stabilize unstable temperature profiles even after convective mixing occurred. In Chapter 3, we also developed a simplified convective adjustment scheme that provided a starting point for parameterizing non-condensing compositional convection.

In Chapter 4, CM1 simulations were used to study moist compositional convection in hydrogen-dominated atmospheres. Our simulations showed that compositional gradients in hydrogen-dominated atmospheres could lead to the formation of clear layers where convection was entirely inhibited. However, the simulations did not show radiative superadiabatic layers in the temperature profile due to long radiative relaxation timescales. Near-term future work will address numerical error and uncertainty in the CM1 condensation scheme that affects the relative humidity and condensate mixing ratio of the adiabatic simulations. Further, future work will assess the stability of steep radiative layers to moist compositional convection. Additional simulations are planned, starting on a saturated superadiabatic profile, to determine the stability of this atmospheric state.

Convection resolving simulations are widely used to study convection phenomena on Mars (Spiga et al., 2017), Venus (Lefèvre et al., 2017), Titan (Rafkin et al., 2022), and exoplanets and brown dwarfs (Maxence Lefèvre, 2021; Lefèvre et al., 2022; Tan et al., 2021; Seeley and Wordsworth, 2021). This thesis primarily models compositional convection in a generalized framework to set a foundation for understanding the impact of compositional gradients on convection in the diverse range of exoplanet atmospheres. Despite the insights gained from CM1 in this work, we faced multiple challenges when using this model. During our non-condensing convection simulation work, we encountered NaN errors, issues with MPI integration within the CM1 code, and numerical stability issues. Additionally, the use of virtual potential temperature for a prognostic variable in CM1 created issues for energy and

mass conservation. These issues were addressed during the course of running our CM1 simulations. However, CM1 has proved to be difficult to use when confronted with the challenge of exoplanet atmospheres. Future work involving 3D convection resolving studies should consider alternative convection codes like SNAP (Li and Chen, 2019) or DAM (Seeley and Wordsworth, 2021), which show more adaptability to exotic exoplanet conditions.

Future work should focus on parameterizing both dry and moist compositional convection for use in general circulation models and conducting further 3D convection resolving studies to understand exoplanet climates. Parameterizing compositional convection for sub-Neptune and super-Earth exoplanet atmospheres would allow to study how compositional convection interacts with other atmospheric processes and affects the global climate of these exoplanets.

3D convection resolving simulations can provide insights to some open questions about the climate of exoplanets. For instance, future work could focus on 3D simulations for "Hycean Worlds" – a subset of sub-Neptunes, characterized by large H_2O oceans beneath a H_2-rich atmospheres (Madhusudhan et al., 2021). Hycean Worlds are hypothesized as a type of habitable sub-Neptune, where habitability is defined by the presence of liquid water on the planet's surface. However, Innes and Pierrehumbert (2022) used a 1D radiative-convective model to argue that compositional stabilization due to mean molecular weight gradients in H_2-dominated atmospheres can strongly restrict the conditions under which Hycean worlds can exist. 3D convection resolving simulations similar to those we perform in Chapter 4 can be used to probe what happens when the convection is resolved rather than parameterized.

Additionally, exoplanets that have water-rich atmospheres with a small amount of non-condensible species are hypothesized to be stable to convection (Ding and Pierrehumbert, 2016) in a regime where radiative cooling is balancing condensation. For a pure steam atmosphere, the temperature profile is expected to follow a dew-point adiabat, which has

weak vertical temperature gradients. However, according to the Guillot criterion, introducing even a small amount of H_2 into a pure steam layer would stabilize the atmosphere and cause the temperature profile to approach a steep radiative profile (Innes and Pierrehumbert, 2022). 3D compositional convection simulations should investigate the buoyancy and stability to convection within this regime.

3D convection resolving simulations can also be used to study compositional stabilization in magma ocean planets. Magma ocean planets are thought to have recently formed had have hydrogen-dominated atmospheres above a magma ocean. SiO is expected to be out-gassed by the magma ocean (Misener and Schlichting, 2022; Markham et al., 2022). The convective stabilization of SiO in magma ocean planets could affect the temperature structure of these planet and their subsequent evolution. 3D convection resolving simulations could explore how compositional effects in magma ocean planets alter the atmospheric structure and implication of this for the planetary evolution.

Thermochemcial convection is largely unexplored. 3D convection resolving simulation could also study how chemical reactions in the atmosphere would affect convection (i.e thermochemical convection). Specifically, Misener et al. (2023) proposed SiO reacts with H_2 to form SiH_4 in magma ocean planets. 3D convection resolving simulations could be used to explore how compositional convection and chemical reactions interact and alter the atmospheric structure and explore the implications for the evolution and observables of these exoplanets.

Lastly, JWST observations of the sub-Neptune, K2 18 b have suggested a non-detection of ammonia (Madhusudhan et al., 2023). However, ammonia is expected to form abundantly in the deep atmospheres of sub-Neptune worlds (Tsai et al., 2021). Convection resolving simulations could be used to explore if compositional gradients can prevent ammonia from reaching the upper layers of the atmosphere where it might be observable.

Appendix

An Overview of Cloud Model 1

The equations solved within CM1 are presented and derived in detail in Bannon (2002) and Bryan and Fritsch (2002), and are summarized within this Appendix. We focus on providing an overview of the governing equations of CM1 and additional modules used within the simulations presented in Chapters 3 and 4. The CM1 code and a list of publications using this model are available at `https://www2.mmm.ucar.edu/people/bryan/cm1/`.

CM1 is a non-hydrostatic fluid flow model that is used to simulate idealized atmospheric phenomena in a 3D Cartesian domain (x, y, z) as a function of time, t. The prognostic variables in CM1 are the 3D components of flow velocity (u, v, w), the non-dimensional pressure perturbation (π'), and the non-dimensional temperature perturbation (θ'). The governing equations of CM1 are given by the ideal gas law, conservation of mass, energy, and momentum, per unit mass of the background atmosphere. The governing equations are all presented assuming an atmosphere with some amount of atmospheric tracer described by q_v. In the following sections, I first derive governing equations used in CM1, and then I discuss boundary conditions and turbulence parameterization.

CM1 has been used to model pure steam atmospheres (Tan et al., 2021) and cloud-convection feedback in the atmospheres of brown dwarfs (Lefèvre et al., 2022). The most extensive application of CM1 is the study of convective flows on Earth, covering topics

such as tropical cyclones, thunderstorms, deep moist convection, and idealized studies aimed at enhancing our understanding of Earth's convection (see list of publications at https://www2.mmm.ucar.edu/people/bryan/cm1/). We chose CM1 for our study over other open-source convection resolving models because of its simple code structure and versatility. CM1 is capable of fully compressible, non-hydrostatic atmospheric modeling. In addition, the CM1 code is written to be easily modifiable, and allows users to add or remove complexity from atmospheric model and for user manipulation of the governing equations.

CM1 Governing Equations

To begin, consider an arbitrary fixed volume V, and a flow property per unit volume, χ that is conserved. The change in χ within the volume is given by,

$$\frac{\partial \chi}{\partial t} + \nabla \cdot (\chi u_\chi) = \dot{\chi}, \tag{1}$$

where $\dot{\chi}$ is the rate at which χ is created or destroyed within the volume, and U_χ is the velocity at which χ is transported through the control volume.

Applying Eqn. 1 to the density of the background atmosphere, ρ_b, yields,

$$\frac{D\rho_b}{Dt} + \rho_b \nabla \cdot U = 0, \tag{2}$$

where U is the velocity, $\frac{D}{Dt}$ represents the material derivative which is given by,

$$\frac{D}{Dt} = \frac{\partial}{\partial t} + (U \cdot \nabla), \tag{3}$$

and ∇ is the *del* operator. Note, we use the subscript b to denote the background atmosphere, v to denote an atmospheric tracer and 0 to denote an atmospheric property at the reference initial state. The equations in this appendix are derived in a general framework and the

atmospheric tracer can be condensing or non-condensing. We use the mass mixing ratio to describe the relative amount of atmospheric tracer to the background air, $q_v = \rho_v / \rho_b$, where the total density of atmosphere is given by $\rho = \rho_b(1 + q_v)$.

The velocity of flow property χ may differ than the background air velocity, U. We define the velocity at which the flow property χ moves as,

$$u_\chi = U + v_\chi, \tag{4}$$

where v_χ is the velocity of χ relative to the background atmosphere. For instance, if χ represents an atmospheric tracer velocity then v_χ is the diffusive flux of the tracer component within the atmosphere. Using the definition of v_χ, a general conservation law can be written per unit mass of background atmosphere as,

$$\frac{D}{Dt}\left(\frac{\chi}{\rho_b}\right) = \frac{\dot{\chi}}{\rho_b} - \frac{1}{\rho_b}\nabla \cdot (\chi\, v_\chi). \tag{5}$$

Eqn. 5 states how much the flow property per unity mass of background air χ/ρ_b will change due to a source of χ or convergence of χ moving relative to the background air. Eqn. 5 provides the general framework of how the equations of conservation of mass, momentum, and energy are derived per mass of background air in CM1 (Bannon, 2002).

Consider the continuity equation for an atmospheric tracer with a mass mixing ratio q_v. Applying Eqn. 5 with $\chi = \rho_v$ gives,

$$\frac{Dq_v}{Dt} = -\dot{q}_{\text{cond}} - \dot{q}_{\text{dep}} - \frac{1}{\rho_b}\nabla \cdot (\rho_v\, v_v), \tag{6}$$

where $\dot{q}_{\text{cond}}$ describes the rate at which vapor condenses to the liquid phase, and $\dot{q}_{\text{dep}}$ is the rate of deposition. The last term in Eqn. 6 represents the diffusion of the atmospheric tracer in vapor form relative to the background air. The diffusion term is often small and is

neglected in CM1 by default. Similarly, Eqn. 5 can be applied to the density of liquid, ρ_l, and solid, ρ_s, condensate components which yields,

$$\frac{Dq_l}{Dt} = \dot{q}_{\text{cond}} - \dot{q}_{\text{freeze}} - \frac{1}{\rho_b}\frac{\partial(\rho_b V_l q_l)}{\partial z}, \tag{7}$$

$$\frac{Dq_s}{Dt} = \dot{q}_{\text{dep}} + \dot{q}_{\text{freeze}} - \frac{1}{\rho_b}\frac{\partial(\rho_b V_s q_s)}{\partial z}, \tag{8}$$

where $\dot{q}_{\text{freeze}}$ describes the rate at which the liquid phase freezes, $q_l = \rho_l/\rho_b$ is the mass mixing ratio of the liquid condensate, $q_s = \rho_s/\rho_b$ is the mass mixing ratio of the solid condensate, and V_s and V_l are the terminal fall velocity of the solid and liquid condensates, respectively. The condensation, deposition, and freezing rates are determined by cloud microphysics schemes.

Conservation of momentum is determined by applying the general conservation law given by Eqn. 1 to total momentum, $\chi = (\rho_b + \rho_v)\,\bar{u} + \rho_l\,u_l + \rho_s\,u_s$, where $\bar{u}$, is given by,

$$\bar{u} = \frac{\rho_b\,u_b + \rho_v\,u_v}{\rho_b + \rho_v}. \tag{9}$$

The liquid and solid condensates exert a drag force on air as they fall relative to air. This effect is fully discussed is Bannon (2002) and within CM1 is an optional parameter that can be specified. For simplicity, we will neglect the momentum due to the fallout of solid and liquid condensates and use $\chi = (\rho_b + \rho_v)\,\bar{u}$. Source and sink terms for momentum are: the gravitational force, the fluid pressure gradient, the Coriolis force, and frictional forces which we will neglect but are an optional parameter within CM1. Conservation of momentum written in terms of x, y, z components are,

$$\frac{Du}{Dt} = -\frac{1}{\rho_b(1 + q_v + q_1 + q_s)}\frac{dp}{dx} + fv, \tag{10}$$

$$\frac{Dv}{Dt} = -\frac{1}{\rho_b(1+q_v+q_1+q_s)}\frac{dp}{dy} - fu, \tag{11}$$

$$\frac{Dw}{Dt} = -\frac{1}{\rho_b(1+q_v+q_1+q_s)}\frac{dp}{dz} + B; \tag{12}$$

where u, v, w are the x, y, z components of velocity respectively, f is the Coriolis parameter given by $f = 2\Omega\sin\phi$, Ω is the rotation rate of the planet, p is the pressure, and B is the buoyancy of the air parcel. In the work presented in this thesis, we neglect the Coriolis force and set $f = 0$. The original CM1 code calculates the buoyancy as,

$$B = g\left[\frac{\theta'}{\theta_0} + (q_v - q_{v,0})\left(\frac{1}{\epsilon} - 1\right) - (q_l - q_{l,0}) - (q_s - q_{s,0})\right]. \tag{13}$$

where θ is a non-dimensional temperature, ϵ is the mean molecular weight ratio of the tracer to the background air, and g is the gravitational acceleration. However, Eqn. 13 assumes dilute amounts of q_v, q_l and q_s. We have modified the CM1 code to use a more general form of buoyancy without making the dilute approximation,

$$B = -g\frac{\rho'}{\rho_0}, \tag{14}$$

where ρ' is the total density perturbation at a given time and ρ_0 is the total density of the reference initial state.

Lastly, we use **conservation of energy** to determine the change in thermodynamic pressure and temperature. From the ideal gas law, the total pressure is defined as,

$$p = p_b + p_v \tag{15}$$

$$= \rho_b R_b T + \rho_v R_v T \tag{16}$$

$$= \rho_b R_b T\left(1 + \frac{q_v}{\epsilon}\right), \tag{17}$$

where T is the temperature, ρ is density, R is the gas constant, ϵ is the mean molecular weight ratio of the atmospheric tracer to the background air,

$$\epsilon = \frac{R_b}{R_v} = \frac{M_v}{M_b}. \tag{18}$$

Again, the subscripts b and v are used to denote properties of the background atmosphere and the atmospheric tracer, respectively.

CM1 defines a non-dimensional pressure using a reference pressure, p_{00}, as

$$\pi \equiv \left(\frac{p}{p_{00}}\right)^{\frac{R_b}{C_{p,b}}}, \tag{19}$$

where R is the gas constant of the background atmosphere and $C_{p,b}$ is the heat capacity at constant pressure per unit mass of the background atmosphere. A non-dimensional temperature can be defined in terms of π as,

$$\theta = \frac{T}{\pi}. \tag{20}$$

The equation of state can be written in terms of π as,

$$\pi = \left(\frac{\rho_b R_b \theta (1 + q_v/\epsilon)}{P_{00}}\right)^{\frac{R_b}{C_{v,b}}}, \tag{21}$$

where $C_{v,b}$ is the heat capacity at constant volume per unit mass of the background atmosphere.

Applying the general conservation law, Eqn. 1, the atmospheric temperature gives,

$$C_{v,\mathrm{mix}} \frac{DT}{Dt} = -\frac{P}{\rho_b} \nabla \cdot \bar{u} + \dot{q}_{\mathrm{phase}} + \dot{q}_{\mathrm{rad}} + \dot{q}_{\mathrm{dis}} \tag{22}$$

where $C_{v,\mathrm{mix}}$ is the heat capacity at constant volume for the mixture of background air and atmospheric tracer, $\dot{q}_{\mathrm{rad}}$ is total heating per unit mass of background air due to radiation, $\dot{q}_{\mathrm{dis}}$ is heating due to viscous dissipation of falling condensate phases, and $\dot{q}_{\mathrm{phase}}$ is the heating due to phase changes of the atmospheric tracer. $\dot{q}_{\mathrm{rad}}$ is given by the radiation scheme. $\dot{q}_{\mathrm{phase}}$ is the change in energy due to a phase change and is given by,

$$\dot{q}_{\mathrm{phase}} = L_v \dot{q}_{\mathrm{cond}} + L_s \dot{q}_{\mathrm{dep}} + L_f \dot{q}_{\mathrm{freeze}} \tag{23}$$

where L_v, L_s and L_f are the latent heat release due to condensation, deposition and freezing respectively. The heat capacity at constant pressure for a mixture of background air with an atmospheric tracer is given by,

$$\mathrm{C_{p,mix}} = \frac{1}{1+\mathrm{q_v}}\mathrm{C_{p,b}} + \frac{\mathrm{q_v}}{1+\mathrm{q_v}}\mathrm{C_{p,v}}. \tag{24}$$

CM1 uses non-dimensional temperature, θ instead of temperature. We can convert Eqn. 22 in terms of θ as,

$$\begin{aligned}\frac{D\theta}{Dt} = &-\left(\frac{R_{\mathrm{mix}}}{C_{v,\mathrm{mix}}} - \frac{R_b C_{p,\mathrm{mix}}}{C_{p,b} C_{v,\mathrm{mix}}}\right)\theta\nabla\cdot\bar{u} \\ &+\left(\frac{C_{v,b}}{C_{v,\mathrm{mix}} C_{p,b}\pi}\right)(L_v\dot{q}_{\mathrm{cond}} + L_s\dot{q}_{\mathrm{dep}} + L_f\dot{q}_{\mathrm{freeze}}) \\ &-\theta\frac{R_v}{C_{v,mix}}\left(1 - \frac{R_b C_{p,mix}}{C_{p,b} R_{\mathrm{mix}}}\right)(\dot{q}_{\mathrm{cond}} + \dot{q}_{\mathrm{dep}}) + \dot{q}_{\mathrm{rad}} + \dot{q}_{\mathrm{dis}}\end{aligned} \tag{25}$$

R_{mix} is the gas constant for a mixture of background air with an atmospheric tracer is given by,

$$\mathrm{R_{mix}} = \mathrm{R_b}\left(\frac{1}{1+\mathrm{q_v}}\right) + \mathrm{R_v}\left(\frac{\mathrm{q_v}}{1+\mathrm{q_v}}\right). \tag{26}$$

To get an equation for the pressure, we use Eqn. 25 and the equation of state Eqn. 21 to eliminate temperature;

$$\begin{aligned}\frac{\mathrm{D}\pi}{\mathrm{Dt}} &= -\left(\frac{R_b}{C_b}\frac{C_{p,\mathrm{mix}}}{C_{v,\mathrm{mix}}}\right)\nabla\cdot\bar{u} \\ &+ \frac{R_b}{C_{p,b}C_{v,\mathrm{mix}}\theta}\left(L_v\dot{q}_{\mathrm{cond}} + L_s\dot{q}_{\mathrm{dep}} + L_f\dot{q}_{\mathrm{freeze}}\right) \\ &- \frac{R_b}{C_{p,b}}\left(\pi\frac{R_v C_{p,\mathrm{mix}}}{R_{\mathrm{mix}}C_{v,\mathrm{mix}}}\right)\left(\dot{q}_{\mathrm{cond}} + \dot{q}_{\mathrm{dep}}\right) + \dot{q}_{\mathrm{rad}} + \dot{q}_{\mathrm{dis}}.\end{aligned} \tag{27}$$

Eqn. 27 and 25 are used in CM1 to determine the thermodynamic state of the system.

CM1 allows for optional parameters which include tendencies of sub-grid turbulence, additional optional diffusive tendencies, Newtonian relaxation, cooling and warming due to condensate drag during fallout. These optional effects are described in Bryan (2009).

To initialize CM1, the user must specify the base state by defining the initial π, θ, u, v, w, and q_v as a function of the vertical coordinate z. CM1 uses this base state as the reference state for the buoyancy calculation. CM1 integrates the governing equations using a third order Runge-Kutta time differentiation and fifth order spatial derivatives for the advection terms. The equations are evaluated in a two-step process. In the *dynamical step* all terms involving time are integrated forward, neglecting any phase change terms. The dynamical step is followed by the *microphysical step* where only terms involving phase changes are evaluated. CM1 then iterates between the two steps until θ converges. Once θ converges, CM1 moves on to the next time step. How the governing equations are formulated and integrated numerically is further discussed in Bryan and Fritsch (2002), Bryan (2009), Bryan and Morrison (2012). The CM1 governing equations make the following assumptions:

- The atmosphere behaves as an ideal gas.
- Diffusive effects in the vapor phase are negligible $\frac{1}{\rho_{air}}\nabla\cdot(\chi\, v_\chi) \sim O(10^{-3})$ m s^{-1}

- Condensates are incompressible and have the same temperature as surrounding background atmosphere.
- All heat capacity terms are independent of temperature

CM1 Model Setup

On top of the governing equations, CM1 can include and model sub-grid turbulence, terrain, Newtonian relaxation, additional artificial diffusion, radiation and microphysics. Here, we provide an overview of the model setup used within the CM1 simulations performed within this work. We refer the reader to the CM1 documentation for a comprehensive list of model setup schemes and options that are available (Bryan, 2009).

In the simulations presented in Chapter 3 and 4, we run CM1 with a Large Eddy Simulation (LES) closure for turbulence, we set a fixed surface temperature lower boundary condition with no terrain, no additional diffusion, no additional heat nor moisture fluxes, and we use a Rayleigh dampening layer (Newtonian relaxation) in the upper part of the simulation domain (5 - 10 km from the top of the domain) to damp out any upward propagating waves. In Chapter 4, we use the Rotunno and Emanuel microphysics scheme (Rotunno and Emanuel, 1987) and the TWOSTR gray gas radiative transfer module (Kylling et al., 1995). Both the microphysics and radiation schemes are described in Chapter 4.

Turbulence

We run CM1 with a LES closure for turbulence using a turbulent kinetic energy (TKE) scheme Deardorff (1980). This allows to account for tendencies due to sub-grid scale turbulence and molecular diffusion. CM1 calculates turbulence tendencies for the velocity components, potential temperature, and the vapor, liquid, and solid mass mixing ratio of the atmospheric tracer. Turbulence tendency terms are added to the conservation of

momentum equations (Eqns. 10 – 12), continuity equations for atmospheric tracer (Eqns. 6 – 8), and the thermodynamic equation for θ (Eqn. 25). Turbulence tendency terms affect the non-dimensional pressure through the tendency for θ and q_v. The TKE scheme uses the predicted sub-grid kinetic energy to determine the eddy diffusivity K_h and the eddy viscosity, K_m. These eddy coefficients are directly related to the turbulent tendencies.

Rayleigh Dampening Layer

A Rayleigh dampening layer is used to damp out upward propagating waves in the top portion of the atmospheric domain. The Rayleigh dampening scheme nudges an atmospheric quantity towards the base initial state where it is applied. In CM1, this Newtonian relaxation is only applied to the 3D velocity components given by Eqn. 10 – 12 and the θ equation given by Eqn. 25. The area of the Rayleigh dampening layer is omitted in the results presented in Chapter 3 and 4.

Surface and Boundary Conditions

We use the original CM1 formulation for the surface boundary conditions. In this setup, the surface (ground) temperature and moisture availability remain fixed over time. The user specifies a ground temperature in the input file. CM1 calculates a surface momentum and enthalpy exchange coefficient, which is then used as a turbulent flux to adjust the lowest level atmospheric temperature. The CM1 code also allows the user to override or specify additional surface heat or moisture exchange fluxes. In the simulations presented in Chapter 3 and 4, we do not set any additional heat nor moisture surface fluxes. We use periodic lateral boundary conditions and a partial-slip bottom boundary condition and a free-slip top boundary condition for the atmospheric winds.

References

Arakawa, A. (2004). The cumulus parameterization problem: Past, present, and future. *Journal of Climate*, 17(13):2493–2525.

Bannon, P. R. (2002). Theoretical foundations for models of moist convection. *Journal of the Atmospheric Sciences*, 59(12):1967–1982.

Benneke, B., Knutson, H. A., Lothringer, J., Crossfield, I. J., Moses, J. I., Morley, C., Kreidberg, L., Fulton, B. J., Dragomir, D., Howard, A. W., Wong, I., Désert, J.-M., Mccullough, P. R., Kempton, E. M.-R., Fortney, J., Gilliland, R., Deming, D., and Kammer, J. (2019a). A sub-neptune exoplanet with a low-metallicity methane-depleted atmosphere and mie-scattering clouds. *Nature Astronomy*, 3(9):813–821.

Benneke, B., Wong, I., Piaulet, C., Knutson, H. A., Lothringer, J., Morley, C. V., Crossfield, I. J. M., Gao, P., Greene, T. P., Dressing, C., Dragomir, D., Howard, A. W., McCullough, P. R., Kempton, E. M.-R. R., Fortney, J. J., and Fraine, J. (2019b). Water vapor and clouds on the habitable-zone sub-neptune exoplanet k2-18b. *The Astrophysical Journal*, 887(1):L14.

Bernstein, I. B. and Book, D. L. (1983). Effect of compressibility on the rayleigh–taylor instability. *The Physics of Fluids*, 26(2):453–458.

Bézard, B., Charnay, B., and Blain, D. (2022). Methane as a dominant absorber in the habitable-zone sub-neptune k2-18 b. *Nature Astronomy*, 6(5):537–540.

Bryan, G. H. (2009). The governing equations for cloud model 1.

Bryan, G. H. and Fritsch, J. M. (2002). A benchmark simulation for moist nonhydrostatic numerical models. *Monthly Weather Review*, 130(12):2917–2928.

Bryan, G. H. and Morrison, H. (2012). Sensitivity of a simulated squall line to horizontal resolution and parameterization of microphysics. *Monthly Weather Review*, 140(1):202–225.

Bud'ko, A. and Liberman, M. (1992). Stabilization of the rayleigh–taylor instability by convection in smooth density gradient: Wentzel–kramers–brillouin analysis. *Physics of Fluids B: Plasma Physics*, 4(11):3499–3506.

Charbonneau, D., Brown, T. M., Noyes, R. W., and Gilliland, R. L. (2002). Detection of an extrasolar planet atmosphere. *The Astrophysical Journal*, 568(1):377–384.

Charnay, B., Blain, D., Bézard, B., Leconte, J., Turbet, M., and Falco, A. (2021). Formation and dynamics of water clouds on temperate sub-neptunes: the example of k2-18b. *Astronomy & Astrophysics*, 646:A171.

Charnay, B., Meadows, V., and Leconte, J. (2015a). 3d modeling of gj1214b's atmosphere: vertical mixing driven by an anti-hadley circulation. *The Astrophysical Journal*, 813(1):15.

Charnay, B., Meadows, V., Misra, A., Leconte, J., and Arney, G. (2015b). 3d modeling of gj1214b's atmosphere: formation of inhomogeneous high clouds and observational implications. *The Astrophysical Journal Letters*, 813(1):L1.

Christie, D. A., Lee, E. K. H., Innes, H., Noti, P. A., Charnay, B., Fauchez, T. J., Mayne, N. J., Deitrick, R., Ding, F., Greco, J. J., Hammond, M., Malsky, I., Mandell, A., Rauscher, E., Roman, M. T., Sergeev, D. E., Sohl, L., Steinrueck, M. E., Turbet, M., Wolf, E. T., Zamyatina, M., and Carone, L. (2022). Camembert: A mini-neptunes general circulation model intercomparison, protocol version 1.0.a cuisines model intercomparison project. *The Planetary Science Journal*, 3(11):261.

Cloutier, R. and Menou, K. (2020). Evolution of the radius valley around low-mass stars from kepler and k2. *The Astronomical Journal*, 159(5):211.

Cowan, N. B. and Agol, E. (2010). A model for thermal phase variations of circular and eccentric exoplanets. *The Astrophysical Journal*, 726(2):82.

Daley-Yates, S., Padioleau, T., Tremblin, P., Kestener, P., and Mancip, M. (2021). Idealised 3d simulations of diabatically forced ledoux convection-application to the atmosphere of hot rocky exoplanets. *Astronomy & Astrophysics*, 653:A54.

Deardorff, J. W. (1980). Stratocumulus-capped mixed layers derived from a three-dimensional model. *Boundary-layer meteorology*, 18:495–527.

Demory, B.-O., Gillon, M., De Wit, J., Madhusudhan, N., Bolmont, E., Heng, K., Kataria, T., Lewis, N., Hu, R., Krick, J., et al. (2016). A map of the large day–night temperature gradient of a super-earth exoplanet. *Nature*, 532(7598):207–209.

Diamond-Lowe, H., Berta-Thompson, Z., Charbonneau, D., and Kempton, E. M.-R. (2018). Ground-based optical transmission spectroscopy of the small, rocky exoplanet gj 1132b. *The Astronomical Journal*, 156(2):42.

Ding, F. and Pierrehumbert, R. T. (2016). Convection in condensible-rich atmospheres. *The Astrophysical Journal*, 822(1):24.

Drummond, B., Carter, A. L., Hébrard, E., Mayne, N. J., Sing, D. K., Evans, T. M., and Goyal, J. (2019). The carbon-to-oxygen ratio: implications for the spectra of hydrogen-dominated exoplanet atmospheres. *Monthly Notices of the Royal Astronomical Society*, 486(1):1123–1137.

Drummond, B., Mayne, N., Baraffe, I., Tremblin, P., Manners, J., Amundsen, D. S., Goyal, J., and Acreman, D. (2018). The effect of metallicity on the atmospheres of exoplanets with fully coupled 3d hydrodynamics, equilibrium chemistry, and radiative transfer. *Astronomy & Astrophysics*, 612:A105.

Elkins-Tanton, L. T. and Seager, S. (2008). Ranges of atmospheric mass and composition of super-earth exoplanets. *The Astrophysical Journal*, 685(2):1237–1246.

Emanuel, K. A. (1994). *Atmospheric convection*. Oxford University Press, USA.

Fauchez, T. J., Turbet, M., Wolf, E. T., Boutle, I., Way, M. J., Del Genio, A. D., Mayne, N. J., Tsigaridis, K., Kopparapu, R. K., Yang, J., Forget, F., Mandell, A., and Domagal Goldman, S. D. (2020). Trappist-1 habitable atmosphere intercomparison (thai): Motivations and protocol version 1.0. *Geoscientific Model Development*, 13(2):707–716.

Fauchez, T. J., Villanueva, G. L., Sergeev, D. E., Turbet, M., Boutle, I. A., Tsigaridis, K., Way, M. J., Wolf, E. T., Domagal-Goldman, S. D., Forget, F., et al. (2022). The trappist-1 habitable atmosphere intercomparison (thai). iii. simulated observables—the return of the spectrum. *The Planetary Science Journal*, 3(9):213.

Fischer, D. A., Howard, A. W., Laughlin, G. P., Macintosh, B., Mahadevan, S., Sahlmann, J., and Yee, J. C. (2014). Exoplanet detection techniques. In Beuther, H., Klessen, R. S., Dullemond, C. P., and Henning, T. K., editors, *Protostars and Planets VI*, pages 715–738. University of Arizona Press.

Freedman, R. S., Lustig-Yaeger, J., Fortney, J. J., Lupu, R. E., Marley, M. S., and Lodders, K. (2014). Gaseous mean opacities for giant planet and ultracool dwarf atmospheres over a range of metallicities and temperatures. *The Astrophysical Journal Supplement Series*, 214(2):25.

Friedson, A. J. and Gonzales, E. J. (2017). Inhibition of ordinary and diffusive convection in the water condensation zone of the ice giants and implications for their thermal evolution. *Icarus*, 297:160–178.

Fulton, B. J., Petigura, E. A., Howard, A. W., Isaacson, H., Marcy, G. W., Cargile, P. A., Hebb, L., Weiss, L. M., Johnson, J. A., Morton, T. D., et al. (2017). The california-kepler survey. iii. a gap in the radius distribution of small planets. *The Astronomical Journal*, 154(3):109.

Garaud, P. (2018). Double-diffusive convection at low prandtl number. *Annual Review of Fluid Mechanics*, 50:275–298.

Garaud, P., Medrano, M., Brown, J., Mankovich, C., and Moore, K. (2015). Excitation of gravity waves by fingering convection, and the formation of compositional staircases in stellar interiors. *The Astrophysical Journal*, 808(1):89.

Gauthier, S. and Le Creurer, B. (2010). Compressibility effects in rayleigh-taylor instability-induced flows. *Philosophical Transactions of the Royal Society A: Mathematical, Physical and Engineering Sciences*, 368(1916):1681–1704.

Greene, T. P., Bell, T. J., Ducrot, E., Dyrek, A., Lagage, P.-O., and Fortney, J. J. (2023). Thermal emission from the earth-sized exoplanet trappist-1 b using jwst. *Nature*, 618(7963):39–42.

Guillot, T. (1995). Condensation of methane, ammonia, and water and the inhibition of convection in giant planets. *Science*, 269(5231):1697–1699.

Habib, N. and Pierrehumbert, R. T. (2023). Modelling non-condensing compositional convection for applications to super-earth and sub-neptune atmospheres. *arXiv preprint arXiv:2310.08202*.

Haqq-Misra, J., Wolf, E. T., Joshi, M., Zhang, X., and Kopparapu, R. K. (2018). Demarcating circulation regimes of synchronously rotating terrestrial planets within the habitable zone. *The Astrophysical Journal*, 852(2):67.

Innes, H. and Pierrehumbert, R. T. (2022). Atmospheric dynamics of temperate sub-neptunes. i. dry dynamics. *The Astrophysical Journal*, 927(1):38.

Kaspi, Y. and Showman, A. P. (2015). Atmospheric dynamics of terrestrial exoplanets over a wide range of orbital and atmospheric parameters. *The Astrophysical Journal*, 804(1):60.

Kataria, T., Showman, A. P., Fortney, J. J., Marley, M. S., and Freedman, R. S. (2014). The atmospheric circulation of the super earth gj 1214b: dependence on composition and metallicity. *The Astrophysical Journal*, 785(2):92.

Kempton, E. M.-R., Zhang, M., Bean, J. L., Steinrueck, M. E., Piette, A. A. A., Parmentier, V., Malsky, I., Roman, M. T., Rauscher, E., Gao, P., Bell, T. J., Xue, Q., Taylor, J., Savel, A. B., Arnold, K. E., Nixon, M. C., Stevenson, K. B., Mansfield, M., Kendrew, S., Zieba, S., Ducrot, E., Dyrek, A., Lagage, P.-O., Stassun, K. G., Henry, G. W., Barman, T., Lupu, R., Malik, M., Kataria, T., Ih, J., Fu, G., Welbanks, L., and Mcgill, P. (2023). A reflective, metal-rich atmosphere for gj 1214b from its jwst phase curve. *Nature*, 620(7972):67–71.

Knutson, H. A., Charbonneau, D., Allen, L. E., Fortney, J. J., Agol, E., Cowan, N. B., Showman, A. P., Cooper, C. S., and Megeath, S. T. (2007). A map of the day–night contrast of the extrasolar planet hd 189733b. *Nature*, 447(7141):183–186.

Komacek, T. D. and Abbot, D. S. (2019). The atmospheric circulation and climate of terrestrial planets orbiting sun-like and m dwarf stars over a broad range of planetary parameters. *The Astrophysical Journal*, 871(2):245.

Komacek, T. D. and Showman, A. P. (2016). Atmospheric circulation of hot jupiters: dayside nightside temperature differences. *The Astrophysical Journal*, 821(1):16.

Kreidberg, L. (2017). Exoplanet atmosphere measurements from transmission spectroscopy and other planet star light observations. *arXiv preprint arXiv:1709.05941*.

Kreidberg, L., Bean, J. L., Désert, J.-M., Benneke, B., Deming, D., Stevenson, K. B., Seager, S., Berta-Thompson, Z., Seifahrt, A., and Homeier, D. (2014a). Clouds in the atmosphere of the super-earth exoplanet gj 1214b. *Nature*, 505(7481):69–72.

Kreidberg, L., Bean, J. L., Désert, J.-M., Line, M. R., Fortney, J. J., Madhusudhan, N., Stevenson, K. B., Showman, A. P., Charbonneau, D., McCullough, P. R., et al. (2014b). A precise water abundance measurement for the hot jupiter wasp-43b. *The Astrophysical Journal Letters*, 793(2):L27.

Kylling, A., Stamnes, K., and Tsay, S. C. (1995). A reliable and efficient two-stream algorithm for spherical radiative transfer: Documentation of accuracy in realistic layered media. *Journal of Atmospheric Chemistry*, 21(2):115–150.

Leconte, J., Forget, F., Charnay, B., Wordsworth, R., and Pottier, A. (2013). Increased insolation threshold for runaway greenhouse processes on earth-like planets. *Nature*, 504(7479):268–271.

Leconte, J., Selsis, F., Hersant, F., and Guillot, T. (2017). Condensation-inhibited convection in hydrogen-rich atmospheres-stability against double-diffusive processes and thermal profiles for jupiter, saturn, uranus, and neptune. *Astronomy & Astrophysics*, 598:A98.

Ledoux, P. (1947). Stellar models with convection and with discontinuity of the mean molecular weight. *Astrophysical Journal*, 105:305.

Lefèvre, M., Spiga, A., and Lebonnois, S. (2017). Three-dimensional turbulence-resolving modeling of the venusian cloud layer and induced gravity waves. *Journal of Geophysical Research: Planets*, 122(1):134–149.

Lefèvre, M., Tan, X., Lee, E. K. H., and Pierrehumbert, R. T. (2022). Cloud-convection feedback in brown dwarf atmospheres. *The Astrophysical Journal*, 929(2):153.

Li, C. and Chen, X. (2019). Simulating nonhydrostatic atmospheres on planets (snap): Formulation, validation, and application to the jovian atmosphere. *The Astrophysical Journal Supplement Series*, 240(2):37.

Li, C. and Ingersoll, A. P. (2015). Moist convection in hydrogen atmospheres and the frequency of saturn's giant storms. *Nature Geoscience*, 8(5):398–403.

Luque, R. and Pallé, E. (2022). Density, not radius, separates rocky and water-rich small planets orbiting m dwarf stars. *Science*, 377(6611):1211–1214.

Lustig-Yaeger, J., Fu, G., May, E., Ceballos, K. N. O., Moran, S. E., Peacock, S., Stevenson, K. B., Kirk, J., López-Morales, M., MacDonald, R. J., et al. (2023). A jwst transmission spectrum of the nearby earth-sized exoplanet lhs 475 b. *Nature Astronomy*, pages 1–12.

Madhusudhan, N. (2018). Atmospheric retrieval of exoplanets. *Handbook of Exoplanets*, pages 2153–2182.

Madhusudhan, N. (2019). Exoplanetary atmospheres: Key insights, challenges, and prospects. *Annual Review of Astronomy and Astrophysics*, 57(1):617–663.

Madhusudhan, N., Piette, A. A. A., and Constantinou, S. (2021). Habitability and biosignatures of hycean worlds. *The Astrophysical Journal*, 918(1):1.

Madhusudhan, N., Sarkar, S., Constantinou, S., Holmberg, M., Piette, A. A., and Moses, J. I. (2023). Carbon-bearing molecules in a possible hycean atmosphere. *The Astrophysical Journal Letters*, 956(1):L13.

Markham, S., Guillot, T., and Li, C. (2023). Rainy downdrafts in abyssal atmospheres. *Astronomy and Astrophysics*, 674:1–18.

Markham, S., Stevenson, D., and Guillot, T. (2022). Convective inhibition with an atmosphere, i: super-critical cores on sub-neptune/super-earths. *arXiv preprint arXiv:2207.04708*.

Maxence Lefèvre, Martin Turbet, R. P. (2021). 3d convection-resolving model of temperate, tidally-locked exoplanets. *The Astrophysical Journal*.

Mayne, N., Drummond, B., Debras, F., Jaupart, E., Manners, J., Boutle, I., Baraffe, I., and Kohary, K. (2019). The limits of the primitive equations of dynamics for warm, slowly rotating small neptunes and super earths. *The Astrophysical Journal*, 871(1):56.

Mayor, M. and Queloz, D. (1995). A jupiter-mass companion to a solar-type star. *nature*, 378(6555):355–359.

Menou, K. (2011). Atmospheric circulation and composition of gj 1214b. *The Astrophysical Journal Letters*, 744(1):L16.

Misener, W. and Schlichting, H. E. (2022). The importance of silicate vapour in determining the structure, radii, and envelope mass fractions of sub-neptunes. *Monthly Notices of the Royal Astronomical Society*, 514(4):6025–6037.

Misener, W., Schlichting, H. E., and Young, E. D. (2023). Atmospheres as windows into sub-neptune interiors: Coupled chemistry and structure of hydrogen–silane–water envelopes. *Monthly Notices of the Royal Astronomical Society*, 524(1):981–992.

Moran, S. E., Stevenson, K. B., Sing, D. K., MacDonald, R. J., Kirk, J., Lustig-Yaeger, J., Peacock, S., Mayorga, L., Bennett, K. A., López-Morales, M., et al. (2023). High tide or riptide on the cosmic shoreline? a water-rich atmosphere or stellar contamination for the warm super-earth gj 486b from jwst observations. *The Astrophysical Journal Letters*, 948(1):L11.

Owen, J., Shaikhislamov, I., Lammer, H., Fossati, L., and Khodachenko, M. (2020). Hydrogen dominated atmospheres on terrestrial mass planets: evidence, origin and evolution. *Space Science Reviews*, 216:1–24.

Parmentier, V. and Crossfield, I. (2017). Exoplanet phase curves: Observations and theory. *arXiv preprint arXiv:1711.07696*.

Parmentier, V., Fortney, J. J., Showman, A. P., Morley, C., and Marley, M. S. (2016). Transitions in the cloud composition of hot jupiters. *The Astrophysical Journal*, 828(1):22.

Perez-Becker, D. and Showman, A. P. (2013). Atmospheric heat redistribution on hot jupiters. *The Astrophysical Journal*, 776(2):134.

Pierrehumbert, R. and Gaidos, E. (2011). Hydrogen greenhouse planets beyond the habitable zone. *The Astrophysical Journal Letters*, 734(1):L13.

Pierrehumbert, R. T. (2010). *Principles of planetary climate*. Cambridge University Press.

Popp, M., Schmidt, H., and Marotzke, J. (2016). Transition to a moist greenhouse with co2 and solar forcing. *Nature communications*, 7(1):10627.

Radko, T. (2003). A mechanism for layer formation in a double-diffusive fluid. *Journal of Fluid Mechanics*, 497:365–380.

Rafkin, S. C., Lora, J. M., Soto, A., and Battalio, J. M. (2022). The interaction of deep convection with the general circulation in titan's atmosphere. part 1: Cloud resolving simulations. *Icarus*, 373:114755.

Rogers, L. A. and Seager, S. (2010). A framework for quantifying the degeneracies of exoplanet interior compositions. *The Astrophysical Journal*, 712(2):974–991.

Rotunno, R. and Emanuel, K. A. (1987). An air–sea interaction theory for tropical cyclones. part ii: Evolutionary study using a nonhydrostatic axisymmetric numerical model. *Journal of Atmospheric Sciences*, 44(3):542–561.

Schwarzschild, M. and Härm, R. (1958). Evolution of very massive stars. *The Astrophysical Journal*, 128:348.

Seager, S. and Deming, D. (2010). Exoplanet atmospheres. *Annual Review of Astronomy and Astrophysics*, 48(1):631–672.

Seager, S., Kuchner, M., Hier-Majumder, C., and Militzer, B. (2007). Mass-radius relationships for solid exoplanets. *The Astrophysical Journal*, 669(2):1279.

Seeley, J. T. and Wordsworth, R. D. (2021). Episodic deluges in simulated hothouse climates. *Nature*, 599(7883):74–79.

Seidel, S. D. and Yang, D. (2020). The lightness of water vapor helps to stabilize tropical climate. *Science advances*, 6(19):eaba1951.

Sergeev, D. E., Fauchez, T. J., Turbet, M., Boutle, I. A., Tsigaridis, K., Way, M. J., Wolf, E. T., Domagal-Goldman, S. D., Forget, F., Haqq-Misra, J., Kopparapu, R. K., Lambert, F. H., Manners, J., and Mayne, N. J. (2022). The trappist-1 habitable atmosphere intercomparison (thai). ii. moist cases—the two waterworlds. *The Planetary Science Journal*, 3(9):212.

Sergeev, D. E., Lambert, F. H., Mayne, N. J., Boutle, I. A., Manners, J., and Kohary, K. (2020). Atmospheric convection plays a key role in the climate of tidally locked terrestrial exoplanets: Insights from high-resolution simulations. *The Astrophysical Journal*, 894(2):84.

Shields, A. L. (2019). The climates of other worlds: A review of the emerging field of exoplanet climatology. *The Astrophysical Journal Supplement Series*, 243(2):30.

Showman, A. P. and Guillot, T. (2002). Atmospheric circulation and tides of "51 pegasus b-like" planets. *Astronomy & Astrophysics*, 385(1):166–180.

Southworth, J., Mancini, L., Madhusudhan, N., Mollière, P., Ciceri, S., and Henning, T. (2017). Detection of the atmosphere of the 1.6 m earth exoplanet gj 1132 b. *The Astronomical Journal*, 153(4):191.

Spiga, A., Hinson, D. P., Madeleine, J. B., Navarro, T., Millour, E., Forget, F., and Montmessin, F. (2017). Snow precipitation on mars driven by cloud-induced night-time convection. *Nature Geoscience*, 10(9):652–657.

Stern, M. E. (1960). The "salt-fountain" and thermohaline convection. *Tellus*, 12(2):172–175.

Swain, M. R., Estrela, R., Roudier, G. M., Sotin, C., Rimmer, P. B., Valio, A., West, R., Pearson, K., Huber-Feely, N., and Zellem, R. T. (2021). Detection of an atmosphere on a rocky exoplanet. *The Astronomical Journal*, 161(5):213.

Tan, X., Lefèvre, M., and Pierrehumbert, R. T. (2021). Convection modeling of pure-steam atmospheres. *The Astrophysical Journal Letters*, 923(1):L15.

Tsai, S.-M., Innes, H., Lichtenberg, T., Taylor, J., Malik, M., Chubb, K., and Pierrehumbert, R. (2021). Inferring shallow surfaces on sub-neptune exoplanets with jwst. *The Astrophysical Journal Letters*, 922(2):L27.

Tsiaras, A., Rocchetto, M., Waldmann, I., Venot, O., Varley, R., Morello, G., Damiano, M., Tinetti, G., Barton, E., Yurchenko, S., et al. (2016). Detection of an atmosphere around the super-earth 55 cancri e. *The Astrophysical Journal*, 820(2):99.

Tsiaras, A., Waldmann, I. P., Tinetti, G., Tennyson, J., and Yurchenko, S. N. (2019). Water vapour in the atmosphere of the habitable-zone eight-earth-mass planet k2-18 b. *Nature Astronomy*, 3(12):1086–1091.

Turbet, M., Fauchez, T. J., Sergeev, D. E., Boutle, I. A., Tsigaridis, K., Way, M. J., Wolf, E. T., Domagal-Goldman, S. D., Forget, F., Haqq-Misra, J., Kopparapu, R. K., Lambert, F. H., Manners, J., Mayne, N. J., and Sohl, L. (2022). The trappist-1 habitable atmosphere intercomparison (thai). i. dry cases—the fellowship of the gcms. *The Planetary Science Journal*, 3(9):211.

Van Eylen, V., Agentoft, C., Lundkvist, M. S., Kjeldsen, H., Owen, J. E., Fulton, B. J., Petigura, E., and Snellen, I. (2018). An asteroseismic view of the radius valley: Stripped cores, not born rocky. *Monthly Notices of the Royal Astronomical Society*, 479(4):4786–4795.

Winn, J. N. (2010). Transits and occultations. *arXiv preprint arXiv:1001.2010*.

Wolf, E. T. (2017). Assessing the habitability of the trappist-1 system using a 3d climate model. *The Astrophysical Journal Letters*, 839(1):L1.

Wolf, E. T., Shields, A. L., Kopparapu, R. K., Haqq-Misra, J., and Toon, O. B. (2017). Constraints on climate and habitability for earth-like exoplanets determined from a general circulation model. *The Astrophysical Journal*, 837(2):107.

Wright, J. T. (2017). Radial velocities as an exoplanet discovery method. *arXiv preprint arXiv:1707.07983*.

Wright, J. T. and Gaudi, B. S. (2013). Exoplanet detection methods. *Planets, Stars and Stellar Systems: Volume 3: Solar and Stellar Planetary Systems*, pages 489–540.

Yang, D. and Seidel, S. D. (2020). The incredible lightness of water vapor. *Journal of Climate*, 33(7):2841–2851.

Young, E. D., Shahar, A., and Schlichting, H. E. (2023). Earth shaped by primordial h2 atmospheres. *Nature*, 616(7956):306–311.

Zhang, X. and Showman, A. P. (2017). Effects of bulk composition on the atmospheric dynamics on close-in exoplanets. *The Astrophysical Journal*, 836(1):73.

Zhou, Y. (2017). Rayleigh–taylor and richtmyer–meshkov instability induced flow, turbulence, and mixing. i. *Physics Reports*, 720-722:1–136.

Zieba, S., Kreidberg, L., Ducrot, E., Gillon, M., Morley, C., Schaefer, L., Tamburo, P., Koll, D. D., Lyu, X., Acuña, L., et al. (2023). No thick carbon dioxide atmosphere on the rocky exoplanet trappist-1 c. *Nature*, pages 1–4.